Technische Universität München
TUM School of Medicine and Health

A multi-omic screening approach identifies the ubiquitin ligase DCAF13 as a vulnerability in lung adenocarcinoma

Vinona Tara Wagner (M.Sc.)

Vollständiger Abdruck der von der TUM School of Medicine and Health der Technischen Universität München zur Erlangung eines

Doctor of Philosophy (Ph.D.)

genehmigten Dissertation.

Vorsitz: Prof. Dr. Ruben Portugues

Betreuer*in: Prof. Dr. Florian Bassermann

Prüfer*innen der Dissertation:

1. Prof. Dr. Hana Algül
2. Prof. Dr. Johannes Buchner

Die Dissertation wurde am 25.09.2023 bei der Fakultät für Medizin der Technischen Universität München eingereicht und durch die TUM School of Medicine and Health am 04.12.2023 angenommen.

Content

Abbreviations

°C	Degree celsius
ACN	Acetonitrile
AF	Alexa Fluor
AF	Alexa Fluor
AGC	Automatic gain control
AJCC	American Joint Committee on Cancer
ALK	Anaplastic lymphoma kinase
APS	Ammonium persulfate
ARP2/3	Actin related protein 2/3
ATCC	American Type Culture Collection
BioID	Biotin identification
Blast	Blasticidin
bp	Base pair
BRAF	B-Raf proto-oncogene
BSA	Albumin Fraction V
C-terminal	Carboxy terminal
CAA	2-Chloracetamide
CDC42	Cell division control protein 42 homolog
cDNA	Complementary DNA
CETN3	Centrin-3
COPD	Chronic pulmonary disease
Co-IP	Co-immunoprecipitation
CPM	Counts per million reads
CRISPR	Clustered regularly interspaced short palindromic repeats
CRL	Cullin-RING-ligase
CTNND1	Catenin delta-1
DAMP	Damage-associated molecular pattern
DCAF	DDB1 and CUL4-associated factor
DCAF13	DDB1- and CUL4-associated factor 13
DDB1	Damage Specific DNA Binding Protein 1
DepMap	Dependency Map
diGLY	Lysine-ϵ-Glycine-Glycine ubiquitin remnant motif
DISC	Death-inducing signal complex
DMEM	Dulbecco’s Modified Eagle’s Medium
DMP	Dimethyl pimelimidate
DMSO	Dimethylsulfoxid
DNA	Deoxyribonulceic acid
dNTP	2'-deoxynucleoside-5'-triphosphate
DSMZ	Deutsche Sammlung von Mikroorganismen und Zellkulturen
DTX3	Probable E3 ubiquitin-protein ligase DTX3
DUB	Deubiquitinase
ECL	Enhanced chemiluminescene
EDTA	Ethylenediaminetetraacetic acid
EGFR	Epidermal growth factor receptor

EGTA	Ethylene-bis(oxyethylenenitrilo)tetraacetic acid
EMA	European Medicines Agency
EMEM	Eagle's Minimum Essential Medium
EMT	Epithelial-to-mesenchymal transition
ERBB2	Erb-B2 receptor tyrosine kinase
EV	Empty vector
F-Actin	Filamentous actin
FA	Formic acid
FACS	Fluorescence-activated cell sorting
FBS	Fetal Bovine Serum
FC	Fold change
FDA	Food and Drug Administration
FDR	False discovery rate
FLAG-IP	FLAG-Immunoprecipitation
fw	Forward
G-2-P	ß-Glycerolphosphate disodium salt hydrate
G-Actin	Globular actin
GAPDH	Glyceraldehyde 3-phosphate dehydrogenase
gDNA	Genomic DNA
GFP	Green fluorescent protein
GO	Gene ontology
GSDMD	Gasdermin D
GSDME	Gasdermin E
GSEA	Gene set enrichment analysis
HA	Hemagglutinin
HECT	Homologous to E6AP C terminus
HEPES	N-(2-Hydroxyethyl)piperazine-N-2-ethane sulfonic acid
HR	Hazard Ratio
HRAS	HRAS proto-oncogene
HRP	Horse radish peroxidase
IAP	Immuno-affinity purification
IB	Immunoblotting
IF	Immunofluorescence
IL	Interleukin
IP	Immunoprecipitation
K	Lysine
kb	Kilobase
kDa	Kilo Dalton
KGG	Lysine-glycine-glycine
KRAS	KRAS proto-oncogene
LB	Luria-Bertani
LC	Lung cancer
LCLC	Large cell lung cancer
LC-MS	Liquid chromatography mass spectrometry
Lip-1	Liproxstatin-1
LPS	Lipopolysaccharides

LuAD	Lung adenocarcinoma
LuSC	Lung squamous cell carcinoma
Lys	Lysine
MAP2K1	Mitogen-activated protein kinase kinase 1
MAPK	Mitogen-activated protein kinase
maxIT	Maximum injection time
min	Minute
MOI	Multiplicity of infection
MOMP	Mitochondrial outer membrane permeabilization
MOPS	3-(N-morpholino)propanesulfonic acid
mRNA	Messenger RNA
MS	Mass spectrometry
MS/MS	Tandem Mass spectrometry
MSigDB	Molecular Signatures Database
mTOC	Microtubule organizing center
N-terminal	Amino terminal
NaF	Fluoride ion solution
Nava	Sodium orthovanadate
NCBI	National Center for Biotechnology Information
NCS	Newborn Calf Serum
Nec-1	Necrostatin-1
ng	Nanogram
NGS	Next generation sequencing
NLS	Nuclear localization signal
nM	Nanomolar
NRAS	NRAS proto-oncogene
ns	Not significant
NSCLC	Non-small-cell lung cancer
NT	Non-targeting
PAMP	Pathogen-associated molecular pattern
PBS	Phosphate buffered saline
PCR	Polymerase chain reaction
PD-1	Programmed cell death protein 1
PD-L1	Programmed death-ligand 1
Pen/Strep	Penicillin-streptomycin
PERP	p53 apoptosis effector related to PMP-22
PFA	Paraformaldehyde
PI	Propidium Iodide
PIK3CA	Phosphatidylinositol-4,5-bisphosphate 3-kinase catalytic subunit alpha
PIN	Aprotinin + Soybean trypsin inhibitor + Leupeptin
PMSF	Phenylmethanesulfonylfluoride solution
POLR2	RNA polymerase II
Polybrene	Hexadimethrine bromide
PS	Phosphatidylserine
PTEN	Phosphatase and tensin homolog deleted on chromosome 10
PVDF	Polyvinylidene difluoride

qPCR	Quantitative PCR
RBR	RING-in-between-RING
RBX1	Ring-Box1
rcf	Relative centrifugal force
RING	Really interesting new gene
RNA	Ribonucleic acid
RNA-Seq	RNA sequencing
RNAi	RNA interference
ROCK1	Rho-associated protein kinase 1
ROS1	c-ros oncogene 1
ROS	Reactive oxygen species
RPKM	Reads per kilobase of transcript per million reads mapped
RPLP0	Ribosomal protein large subunit P0
RPMI	Roswell Park Memorial Institute
RT	Room temperature
rv	Reverse
S.D.	Standard deviation
SCLC	Small-cell lung cancer
SDS	Dodecylsulfate-Na-salt
SDS-PAGE	SDS polyacrylamide gel electrophoresis
sec	Second
SF	Double-strep-single-FLAG
sgRNA	Single guide RNA
shRNA	Short-hairpin RNA
siRNA	Small interfering RNA
SUV39H1	Histone-lysine N-methyltransferase SUV39H1
TCA	Trichloroacetic acid solution
TCEP	Tris(2-carboxyethyl)phosphin-hydroshlorid
TCGA	The Cancer Genome Atlas
TEMED	N,N,N`,N``-tetramethyl-ethylenediamine
TFA	Trifluoroacetic acid
TLCK	Nα-Tosyl-L-lysine chloromethyl ketone hydrochloride
TLR	Toll-like receptor
TMT	Tandem mass tags
TOP1	Topoisomerase I
TP53	Tumor protein p53
TPCK	N-p-Tosyl-L-phenylalanine chloromethyl ketone
TSO	Template switch oligo
TUBE	Tandem ubiquitin binding entity
TUM	Technical University Munich
Ub	Ubiquitin
UHRF1	E3 ubiquitin-protein ligase UHRF1
UMI	Unique molecular identifier
UPS	Ubiquitin-proteasome system
UV	Ultraviolet
V	Volt

VASP	Vasodilator-stimulated phosphoprotein
v/v	Volume per volume
vs.	Versus
w/v	Weight per volume
WASP	Wiskott-Aldrich syndrome protein
WB	Washing buffer
WHO	World Health Organization
WT	Wildtype
µg	Microgram
µm	Micrometer
µM	Micromolar

1 Summary

Lung adenocarcinoma (LuAD) constitutes the most prevalent histological subtype within the spectrum of lung cancer. Despite considerable advances in targeted therapy approaches, the prognosis for patients with LuAD remains discouraging and mortality is expected to increase drastically in the coming years (Wéber et al., 2023). This is largely owed to the high heterogeneity in cancer driver mutations, which renders only a subset of patients eligible for targeted therapy, highlighting the need for therapy approaches beyond the level of genetic alterations. Investigating the role of post-translational modifications, such as ubiquitination, in the maintenance of LuAD holds great promise, as the ubiquitin-proteasome system (UPS) is frequently deregulated in cancer (D. Shi & Grossman, 2010).

To identify novel vulnerabilities within the UPS in LuAD, we performed a CRISPR/Cas9-based dropout screen with a pooled sgRNA library targeting 771 genes within the ubiquitin system. The screen identified the poorly characterized E3 ubiquitin ligase DDB1- and CUL4-associated factor 13 (*DCAF13*) as an essential gene for LuAD cell survival. Analysis of the TCGA PanCancer Atlas dataset on LuAD (Ding et al., 2018) revealed *DCAF13* to be significantly overexpressed in tumor tissue compared to normal tissue and high *DCAF13* expression to correlate with adverse overall survival and increased tumor aggressiveness.

Mechanistically, it could be shown that DCAF13 depletion induces cell death, which was found to be dependent on caspase activation. Subsequent investigations established apoptosis as the primary cell death mechanism, which was caused by mitochondrial membrane destabilization and was found to be independent of caspase 8. Immunofluorescence (IF) imaging revealed that DCAF13 localizes primarily to the nucleus, with additional localization to the centrosome and cell-cell contacts, suggesting a potential role in transcription control. Analysis of the transcriptome of DCAF13-depleted cells through gene set enrichment analysis (GSEA) highlighted a significant downregulation of genes involved in ARP2/3-mediated actin nucleation, an essential pathway of actin fiber formation and actin cytoskeleton remodeling (Nolen & Pollard, 2008). IF imaging demonstrated loss of actin stress fibers upon DCAF13 depletion, which occurred independently of caspase activation during apoptosis.

Functionally, DCAF13 is a predicted substrate recruiting unit of a CUL4-family ubiquitin ligase. It could be shown that DCAF13 binds to CUL4A/B and DDB1 to form a ubiquitin ligase complex. In an effort to identify LuAD-specific relevant ubiquitination substrates of DCAF13, we performed affinity-based interactome screening and analyzed the ubiquitome upon DCAF13 depletion by diGLY proteomics. Cross-validation of these approaches revealed the two potential substrate candidates cell division control protein 42 homolog (CDC42) and catenin delta-1 (CTNND1), which are involved in actin cytoskeleton remodeling: (W. W. Liu et al., 2021). The interaction of these proteins with DCAF13 could be shown in LuAD cells but not in HEK293T cells. *In-vivo*-ubiquitination assays in HEK293T revealed no changes in either protein's ubiquitination status upon DCAF13 depletion, indicating that these could be LuAD-specific substrates.

Taken together, the data presented in this thesis depict DCAF13 as a novel vulnerability in LuAD with potential implications in future targeted therapy strategies.

2 Introduction

2.1 Lung cancer

2.1.1 Lung cancer epidemiology and classification

Lung cancer is defined as a malignant transformation of cells residing in the tissue of the lung. It has one of the highest global incidences, with 2.2 million new cases in 2020, and is the leading cause of cancer-related deaths. With around 1.8 million deaths, almost a fifth of worldwide cancer mortality was attributed to lung cancer (18%) in 2020 (Ferlay et al., 2021). Further, current projections estimate mortality to increase up to 2.9 million by 2040 (Wéber et al., 2023).

The predominant risk factor linked to disease development and mortality is tobacco smoke, contributing to 9 out of 10 lung cancer cases (Wéber et al., 2023). Thus, lung cancer prevention efforts have mainly focused on smoking cessation or avoidance. Other risk factors include occupational and environmental exposure to toxins, such as asbestos or air pollutants, and chronic lung diseases like chronic obstructive pulmonary disease (COPD) (Bade & Dela Cruz, 2020).

Lung cancer can be divided into two distinct morphological subtypes: small-cell lung cancer (SCLC) and non-small-cell lung cancer (NSCLC). NSCLC constitutes the majority of lung cancer cases at 85% and is further subdivided into three major histological subtypes: Large-cell carcinoma, squamous cell carcinoma (LuSC), and lung adenocarcinoma (LuAD). Here, LuAD is the most prevalent subtype, with more than 75% of NSCLC cases (Thai et al., 2021). While the classification of lung cancer subtypes is still primarily based on morphology and histology, it is greatly supported by immunohistochemical methods and increasingly by molecular pathology, such as oncogenic mutation detection (A. G. Nicholson et al., 2022).

2.1.2 Lung adenocarcinoma

Lung adenocarcinoma is the most common histological subtype of lung cancer. It arises from glandular epithelial cells and is typically located in the distal regions of the bronchiolar epithelium and the alveolar space (Sainz De Aja et al., 2021).

Molecular profiling of lung adenocarcinoma tumors has revealed a vastly heterogeneous genetic landscape with a plethora of somatic mutations, as depicted in figure 1 for patients with early-stage (Stage I-III) or metastatic (Stage IV) LuAD. Most patients carry activating mutations in genes belonging to the mitogen-activated protein kinase (MAPK) pathway. The most frequently mutated genes are the KRAS proto-oncogene (*KRAS*) (29.1% early-stage, 29.9% metastatic), the B-Raf proto-oncogene (*BRAF*) (7.2% early-stage, 5.5% metastatic), the mitogen-activated protein kinase kinase 1 (*MAP2K1*) (2.1% early-stage and metastatic), and the NRAS proto-oncogene (*NRAS*), and HRAS proto-oncogene (*HRAS*) (1% early-stage and metastatic). Around 14% of early-stage and 30.3% of metastatic-stage tumors harbor an activating mutations in the epidermal growth factor receptor (*EGFR*), and several patients have a mutation (1.8% early-stage, 3.8% metastatic) or amplification (1.6% early-stage and metastatic) of the closely related Erb-B2 receptor tyrosine kinase (*ERBB2*) gene. This highlights the relevance of deregulation in growth-promoting signaling, which is a hallmark of LuAD tumors (Imielinski et al., 2012). Gene fusions in LuAD mainly affect the anaplastic

lymphoma kinase (*ALK*) or c-ros oncogene 1 (*ROS1*). However, these fusion events occur comparatively seldom (Skoulidis & Heymach, 2019). The presence of mutations in major oncogenic drivers, as listed above, are mostly mutually exclusive. However, LuAD patients often carry additional co-mutations in genes, such as the tumor-suppressor tumor protein p53 (*TP53*), promoting genomic instability (Eischen, 2016; Skoulidis & Heymach, 2019). As toxin exposure contributes heavily to LuAD development, these tumors are overall characterized by a large mutational burden (Imielinski et al., 2012; Skoulidis & Heymach, 2019). These aspects contribute to the genetic heterogeneity of patients with LuAD (Collisson et al., 2014; Ding et al., 2008; Imielinski et al., 2012). Notably, a large proportion of tumors cannot be defined by a mutation in a distinct oncogenic driver (27.6% early-stage, 7.8% metastatic), highlighting the need to further characterize these tumors through methods other than genomic sequencing to identify drivers of tumorigenesis in patients with LuAD.

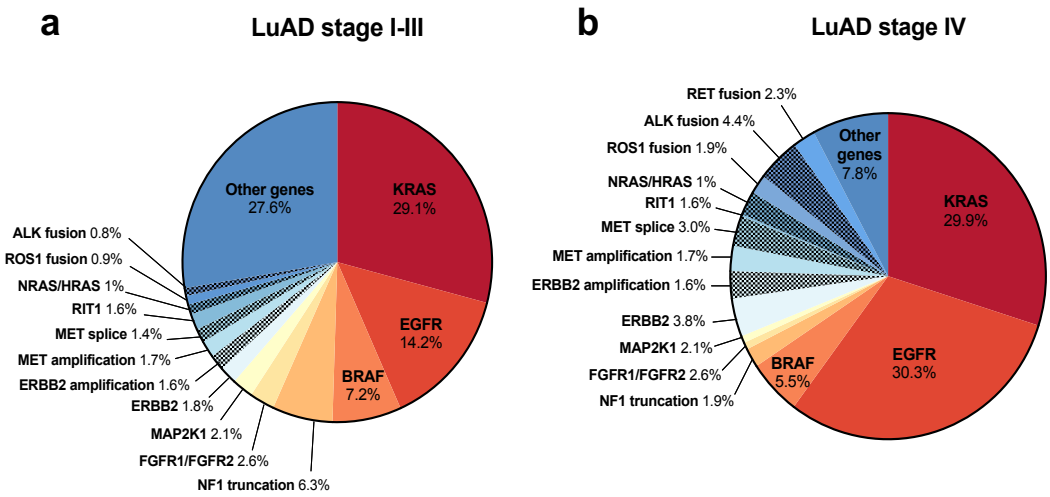

Figure 1: Oncogenic driver heterogeneity in patients with lung adenocarcinoma
Alterations in oncogenic drivers are indicated for patients with early-stage and locally advanced disease (**a**) and metastatic disease (**b**). The analysis was performed by Skoulidis & Heymach, and the figure is adapted from their publication (Skoulidis & Heymach, 2019). The prevalence of oncogenic driver mutations is based on the PanCancer Atlas cohort of The Cancer Genome Atlas (TCGA; n=566) as well as two other cohorts from Imielinski et al. (n=183) and Kadara et al. (n=108) (Imielinski et al., 2012; Kadara et al., 2017).

2.1.3 Overview of the current treatment of LuAD

2.1.3.1 Treatment of early-stage and locally advanced LuAD

Surgical resection is still considered the standard of care for patients with stage I-II NSCLC. In most patients, lobectomy of the afflicted lung lobe is performed (Postmus et al., 2017). However, in patients with a small, non-invasive lesion, sub-lobar resection may be considered and has been shown to provide similar survival and recurrence outcomes as lobectomy (Vansteenkiste et al., 2014).

Adjuvant chemotherapy is generally recommended for stage II and III tumors and should be based on cisplatin in combination with vinorelbine, gemcitabine, docetaxel, or pemetrexed (Postmus et al., 2017). Adjuvant targeted therapy is indicated in patients with *EGFR* exon 10 deletion or exon 21 L858R substitution mutation in the form of the EGFR inhibitor Osimertinib (Remon et al., 2021).

Radiation therapy can be employed for patients with locally advanced lung cancer or contraindication to surgery. This is typically combined with a concurrent platinum-based chemotherapy regimen. Cisplatin is usually the preferred platinum-based agent in this setting. (Eberhardt et al., 2015; Postmus et al., 2017)

Recently, the relevance of immune checkpoint inhibition has been demonstrated. Accordingly, the immune checkpoint inhibitor durvalumab has been approved by the European Medicines Agency (EMA) for consolidation treatment after chemoradiotherapy in unresectable stage III NSCLC (Remon et al., 2021; Spigel et al., 2022). Moreover, the efficacy of immune checkpoint inhibitors in a (neo)adjuvant setting in combination with standard-of-care chemotherapy is currently being evaluated in these patients (Remon et al., 2021).

2.1.3.2 Treatment of metastatic LuAD

Patients with metastatic LuAD have largely benefited from the discovery of targeted therapy. Currently, four major genetic alterations in LuAD are actionable by targeted therapeutics: *ALK* translocation, *BRAF* V600 mutation, *EGFR* mutation, and *ROS1* translocation. A prerequisite for the treatment with a targeted inhibitor is a positive molecular diagnostic for the respective genetic alteration (Hendriks et al., 2023b). Patients harboring a tumor with *ALK* rearrangements can be treated with ALK tyrosine kinase inhibitors, such as alectinib or crizotinib, which are approved by the Food and Drug Administration (FDA) and EMA for first-line therapy (Hendriks et al., 2023b; Kwak et al., 2010; Peters et al., 2017). Crizotinib is also indicated in patients with *ROS1* translocation, as it was shown to inhibit both ALK and ROS1 (Kwak et al., 2010). BRAF inhibitors, such as dabrafenib, are indicated for patients with a *BRAF* V600E mutation (Hendriks et al., 2023b; Planchard et al., 2016). Patients with mutations in *EGFR* are treated with EGFR tyrosine kinase inhibitors, such as osimertinib and erlotinib, in a first-line treatment (Hendriks et al., 2023b; Rosell et al., 2012; Soria et al., 2018). Even though an initial response to EGFR inhibitors is often achieved, almost all patients will develop clinical resistance towards these inhibitors. Resistance is often mediated by additional mutations in *EGFR* or by amplification or mutation of downstream signaling mediators, such as *KRAS* or phosphatidylinositol-4,5-bisphosphate 3-kinase catalytic subunit alpha (*PIK3CA*) (Passaro et al., 2021).

In patients without these actionable genetic mutations, immune checkpoint inhibition is the treatment of choice. The specific treatment is further chosen through histopathological analysis of the tumor's programmed death-ligand 1 (PD-L1) expression. For patients with high PD-L1 expression on cancer cells (>50%), the PD-L1-targeting antibody atezolizumab or the programmed cell death protein 1 (PD-1)-targeting antibody pembrolizumab are FDA and EMA approved first-line treatments (Hendriks et al., 2023a; Jassem et al., 2021; Reck et al., 2016). Moreover, pembrolizumab in combination with platinum-based chemotherapy can be given as a first-line treatment to patients regardless of their PD-L1 status (Gandhi et al., 2018; Hendriks et al., 2023a).

Systemic chemotherapy can be employed in case of contraindication to immunotherapy, such as organ transplantation or severe autoimmune disease (Planchard et al., 2018). Like early-stage and locally advanced NSCLC, chemotherapy in metastatic LuAD heavily relies on platinum-based agents like cisplatin or carboplatin. The treatment is usually administered in a doublet therapy with other cytostatic agents like gemcitabine or pemetrexed (Hendriks et al., 2023a; Oan et al., 2002).

2.2 The ubiquitin system

2.2.1 The ubiquitin code

Ubiquitination is a post-translational modification process of proteins, which is highly dynamic and can be found in virtually all aspects of cellular homeostasis. It describes the three step enzymatic process of covalently attaching the 8 kDa ubiquitin protein to a target protein (Pickart, 2001), as depicted in figure 2. First, a ubiquitin monomer is attached to the ubiquitin-activating enzyme (E1) in an ATP-dependent manner through a highly reactive thioester bond (Schulman & Wade Harper, 2009). Secondly, the ubiquitin moiety is transferred to the ubiquitin-conjugating enzyme (E2) (Ye & Rape, 2009). Lastly, a variety of so-called ubiquitin ligases (E3) coordinate the conjugation of ubiquitin to the designated ubiquitination substrate (Deshaies & Joazeiro, 2009; Rotin & Kumar, 2009). Furthermore, deubiquitinating enzymes (DUBs) are able to remove ubiquitin from proteins.

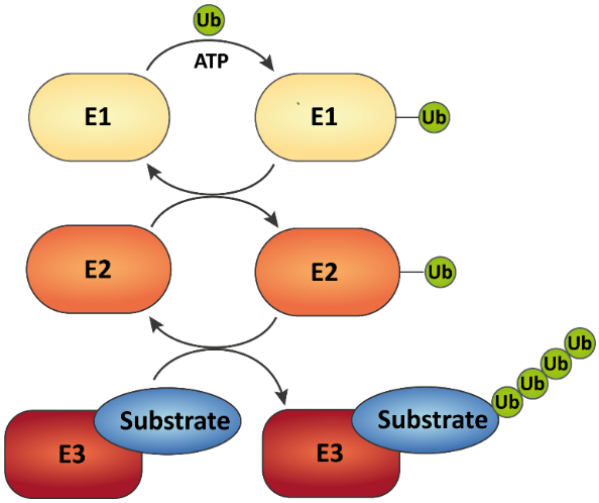

Figure 2: The ubiquitination cascade
Ubiquitination of a substrate requires the consecutive activity of three enzymes. First, ubiquitin is attached to the ubiquitin-activating enzyme (E1) in an ATP-dependent manner. Then, the ubiquitin is transferred to the ubiquitin-conjugating enzyme (E2), and lastly, the ubiquitin-ligase (E3) coordinates the conjugation of ubiquitin to the designated substrate. Ub : Ubiquitin

Ubiquitin is typically attached to lysine (Lys or K) residues of proteins through its C-terminus and forms an isopeptide bond, resulting in monoubiquitination (Ciechanover 2004). Further ubiquitin moieties can then be attached to seven different lysines (K6, K11, K27, K29, K33, K48, K63) within the initial ubiquitin, as well as its N-terminus, to form polyubiquitin chains (Swatek & Komander, 2016). The type of ubiquitin chain determines the fate of the protein, acting as a form of ubiquitin code. Ubiquitin is not only attached in homogenous chains of the same linkage type but can also be modified at several lysine residues, giving rise to branched chains and adding to the vast complexity of the ubiquitin code (Swatek & Komander, 2016).

The most abundant and best characterized form of ubiquitin chain is the linkage on K48. This type of ubiquitin chain typically destines a protein for degradation (Hershko & Ciechanover, 1998; Komander & Rape, 2012; Swatek & Komander, 2016). The degradation is carried out by a large protein complex called the 26S proteasome, which consists of one or two regulatory particles (19S) and a proteolytic 20S core (Bard et al., 2018; Coux et al., 2003). The regulatory particles mediate the recognition of the ubiquitinated proteins, the subsequent removal of the attached ubiquitin, and unfolding of the protein (Tomko & Hochstrasser, 2013). The core particle then executes the cleavage of the unfolded protein via its β-subunits and releases the resulting short peptides of 8-11 amino acids (Coux et al., 2003). Cytoplasmic proteases further process the peptides into amino acids (Coux 1996, Kisselev 1999).

The second most abundant ubiquitin chain is formed by K63 and is associated with many non-degradative functions. For instance, this chain type plays a role in regulating the NF-κB pathway, where it was found to modify protein activity and to function as a signaling scaffold (Z. J. Chen & Sun, 2009; Komander et al., 2009).

The presence of the more unconventional ubiquitin chain types (K6, K11, K27, K29, K33) has been demonstrated *in vivo* (Xu et al., 2009). However, their function is still poorly understood and is thus the subject of current research.

2.2.2 E3 ubiquitin ligases

The human genome encodes for two E1 enzymes, ~40 E2 enzymes, ~600 E3 enzymes, and around 90 DUBs (Z. J. Chen & Sun, 2009). A plethora of cellular processes and proteins can be targeted and modified through a combination of these enzymes (Nandi et al., 2006). It stands to reason that several E3 ligases can target a single protein, and one E3 ligase can target a multitude of proteins, thus alluding to a highly complex network of protein ubiquitination.

E3 ligases can be divided into three major classes by the distinct domains they harbor and the mechanism by which they transfer ubiquitin to the designated substrate (Buetow & Huang, 2016). HECT E3 ligases are defined by their catalytic HECT domain, which first accepts the ubiquitin from the respective E2 enzyme and then transfers it to the ubiquitination substrate (Hershko & Ciechanover, 1998). The second group of E3 enzymes comprises the RING-in-between-RING (RBR) ligases, which contain a RING1-IBR-RING2 catalytic unit. Here, the E2 enzyme transfers the ubiquitin to an active cysteine in the RING2-domain, which is subsequently conjugated to the substrate (Smit & Sixma, 2014). RING E3 ligases form the third class of ubiquitin ligases. Importantly, these ligases do not form an E3 ubiquitin intermediate but rather confer the direct transfer of ubiquitin from the E2 enzyme to the designated substrate (Deshaies & Joazeiro, 2009). Many of these ligases appear in a multimeric complex with the scaffolding protein cullin and are thus called Cullin-RING-ligase (CRL) family (Cardozo & Pagano, 2004; Sarikas et al., 2011).

2.2.3 CUL4 ligases

There are seven different cullin proteins in humans (CUL1, CUL2, CUL3, CUL4A, CUL4B, CUL5, CUL7), which all form different multimeric complexes (Lee & Zhou, 2007). Especially the CUL4 family of CRLs represents an interesting and understudied group of E3 ligases. CUL4A or CUL4B represent the backbone of these ligases, and their C-terminus interacts with

the RING finger protein Ring-Box1 (RBX1), facilitating the recruitment of the E2 enzyme, as depicted in figure 3 (Lee & Zhou, 2007; Petroski & Deshaies, 2005). The N-terminal binding partner of CUL4A/B is Damage Specific DNA Binding Protein 1 (DDB1), which in turn binds to the substrate recruiting unit (Petroski & Deshaies, 2005). The tight conformational packaging of the complex can position the E2 enzyme in close proximity to the substrate, initiating the ubiquitination process.

It has been shown that proteins of the DDB1 and CUL4-associated factor (DCAF) family preferentially function as substrate adapters for CUL4 ligases (Angers et al., 2006; Y. J. He et al., 2006). DCAF proteins contain a WD40 domain consisting of four or more WD repeats that fold into a four-stranded β-sheet and collectively form a propeller-like structure (Lee & Zhou, 2007). Importantly, not all WD40 domain-containing proteins associate with CUL4 and DBB1 and act as substrate adapters. Studies have found that a distinct amino acid sequence, the “WDXR” motif, is essential for the binding of many WD40 proteins to DDB1 (Angers et al., 2006). Additionally, the binding of DCAFs to DDB1-CUL4 might not be sufficient for substrate recruitment and ubiquitination, as posttranslational modification of DCAFs or additional binding factors might be necessary. For instance, the binding of DCAF2 to its substrate CDT1 was found to be dependent on complex formation with PCNA and chromatin (Jin et al., 2006). While many novel DCAFs and WD40 domain-containing proteins have been identified, the molecular function and their candidate substrates remain largely unknown.

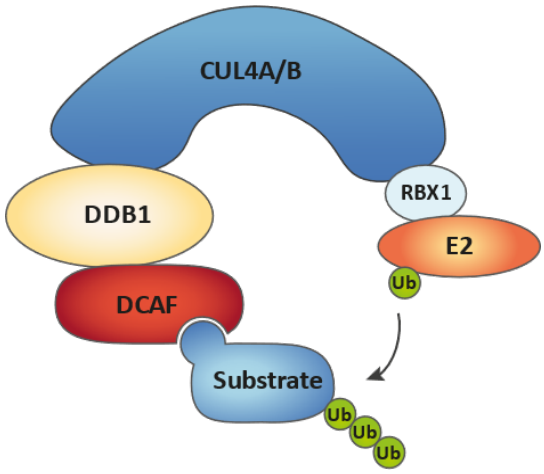

Figure 3: The structure of CUL4 ligases
The CUL4 ligase complex consists of the large scaffolding protein CUL4A or CUL4B. Its C-terminus interacts with the RING finger protein RBX1, which binds to its designated E2 ubiquitin conjugating enzyme. N-terminally, CUL4A/B binds to DDB1, which recruits the substrate specificity receptor. Proteins of the DCAF family preferentially act as substrate adapters for CUL4 ligases. The ubiquitin moiety is ultimately transferred from the RBX1-bound E2 enzyme to the DCAF-bound substrate. Adapted from: (Fouad et al., 2019). Ub : Ubiquitin

2.2.4 DDB1- and CUL4-associated factor 13 (DCAF13)

DDB1- and CUL4-associated factor 13 (DCAF13) is a largely uncharacterized substrate-recognition component of the CUL4 E3 ubiquitin ligase family. The gene is localized on chromosome 8q22.3 and produces two isoforms. The first isoform (Uniprot: Q9NV06-1) has a length of 445 amino acids and a molecular mass of around 51 kDa and represents the canonical form of DCAF13. The second isoform (Uniprot Q9NV06-2) has a length of only 96

amino acids and its function is unknown. The canonical isoform contains seven WD domains (Figure 4a), each forming a four-stranded β-sheet. These seven WD domains collectively form the propeller-like structure as seen in the structural prediction by AlphaFold (Figure 4b). This propeller like structure is characteristic for WD40 domain-containing proteins (Lee & Zhou, 2007), and appears to be essential for the association with DDB1. Several publications have confirmed the binding of DCAF13 to DDB1 (Z. Chen et al., 2018; Y. Zhang et al., 2018). One of these studies has proposed the tumor suppressor phosphatase and tensin homolog deleted on chromosome 10 (PTEN) as a substrate of DCAF13 in osteosarcoma cell lines and therefore implicated DCAF13 as an oncogene in cell survival signaling (Z. Chen et al., 2018).

Recent publications have demonstrated an essential role of Dcaf13 in oocyte maturation and embryonic development in mice (Y. Liu et al., 2019; J. Zhang et al., 2019; Y. Zhang et al., 2018). Moreover, Dcaf13 was shown to influence chromatin tightness (Y. Liu et al., 2019), cellular pluripotency through destabilization of Suv39h1 (Y. Zhang et al., 2018), and rRNA processing (J. Zhang et al., 2019). It is unclear whether these functions of Dcaf13 are only observed in the context of embryonic development in mice or if they are also applicable to humans.

Lastly, an adverse prognostic role of DCAF13 was observed in several cancer entities, such as breast cancer (K. Wang et al., 2019) and hepatocellular carcinoma (Cao et al., 2017; Guojie et al., 2019).

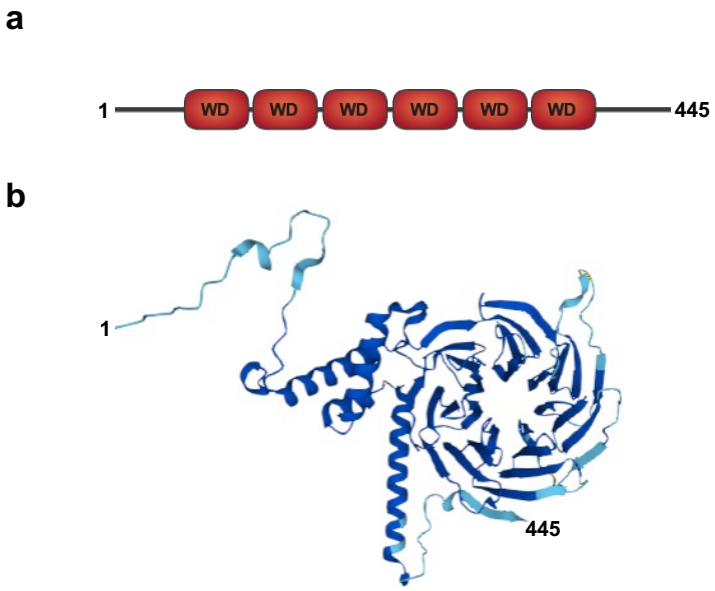

Figure 4: Schematic overview of DCAF13 and its predicted structure
DCAF13 comprises 445 amino acids and contains seven WD domains (**a**). The structural prediction by AlphaFold (Varadi et al., 2022) (**b**) shows that these seven WD domains each form a four-stranded β-sheet, collectively forming a propeller-like structure, the characteristic WD40 domain.

2.3 Cell death

2.3.1 A note about cell death

Scientists initially thought that cells could only die via one of two distinct pathways: programmed apoptotic cell death or uncontrolled necrotic cell death. Decades of research have since discovered numerous other forms of cell death, and many more are still likely to come.

As many of these cell death mechanisms are being described in more complexity, it becomes apparent that there can be an intricate interplay between different cell death pathways. Even though there are additional types of cell death, the following chapters describe the most common and most studied forms of cell death relevant to this study: apoptosis, necroptosis, pyroptosis, and ferroptosis.

2.3.2 Apoptosis

2.3.2.1 Apoptosis in physiology and pathology

Apoptosis is an evolutionarily conserved form of cell death essential for organismal physiology (Singh et al., 2019). It is often referred to as programmed cell death due to its tightly regulated and non-inflammatory nature. Apoptosis is indispensable throughout the life cycle of a multicellular organism, as it is prominent during embryonal development and essential for constant cellular turnover and tissue homeostasis after birth (D'Arcy, 2019; Elmore, 2007).

The dysregulation of such a tightly controlled and crucial process in either direction often culminates in disease. On the one hand, excessive levels of apoptosis are commonly found in neurodegenerative diseases, such as Parkinson's or Alzheimer's disease (D'Arcy, 2019; Dickson, 2004). On the other hand, inhibtion of apoptosis and consequent uncontrolled cellular proliferation is a hallmark of cancer (Hanahan & Weinberg, 2011). Paradoxically, recent reports have also demonstrated a role of apoptosis in promoting cancer (Ichim & Tait, 2016).

2.3.2.2 Characteristics of apoptosis

Apoptosis is morphologically recognizable by cell retraction, rounding, and the distinct process of plasma membrane blebbing (Coleman et al., 2001). This process leads to the formation of the so-called apoptotic bodies, which are taken up by macrophages *in vivo* to recycle the cellular components and to contain tissue damage (Kerr et al., 1972; Savill & Fadok, 2000). An additional characteristic feature is the condensation of the nucleus and its subsequent fragmentation and DNA hydrolysis (Kerr et al., 1972; Taylor et al., 2008; Williams et al., 1974).

Mechanistically, apoptosis is executed through one of two major pathways: the intrinsic or the extrinsic apoptosis pathway. Both pathways strongly depend on cysteine-aspartic proteases known as caspases, which are serially activated and can initiate a plethora of events, thereby rapidly leading to cell death (Creagh et al., 2003; D. W. Nicholson, 1999). Caspases are divided into either initiator or effector caspases, depending on their position and function in the caspase cascade (Cohen, 1997; Elmore, 2007). Despite the differences in the induction of the caspase cascade and the type of initiator caspases between the two pathways, they converge on the same effector caspases, namely caspase-3 and caspase-7 (D'Arcy, 2019).

2.3.2.3 Intrinsic pathway of apoptosis

The intrinsic pathway (Figure 5) is often termed the mitochondrial pathway (Igney & Krammer, 2002) and is mainly triggered by toxic agents, excessive DNA damage, or other cellular stresses (Bertheloot et al., 2021). These stimuli activate members of the BH3-only protein family, which in turn activate the proteins BAX or BAK (D'Arcy, 2019; Ichim & Tait, 2016). The

activation of these proteins induces oligomerization and subsequent pore formation in the mitochondria, causing mitochondrial outer membrane permeabilization (MOMP) (Tait & Green, 2010). This initiates a release of pro-apoptotic proteins, such as cytochrome c or SMAC, into the cytosol. Cytochrome c interacts with APAF1, leading to the assembly of the so-called apoptosome (Cain et al., 2002). The apoptosome recruits and activates the initiator caspase of the intrinsic pathway, caspase-9 (Acehan et al., 2002). Active caspase-9 subsequently cleaves and activates the effector caspase-3, leading to rapid cleavage of caspase substrates and cell death (Cain et al., 2002; Taylor et al., 2008).

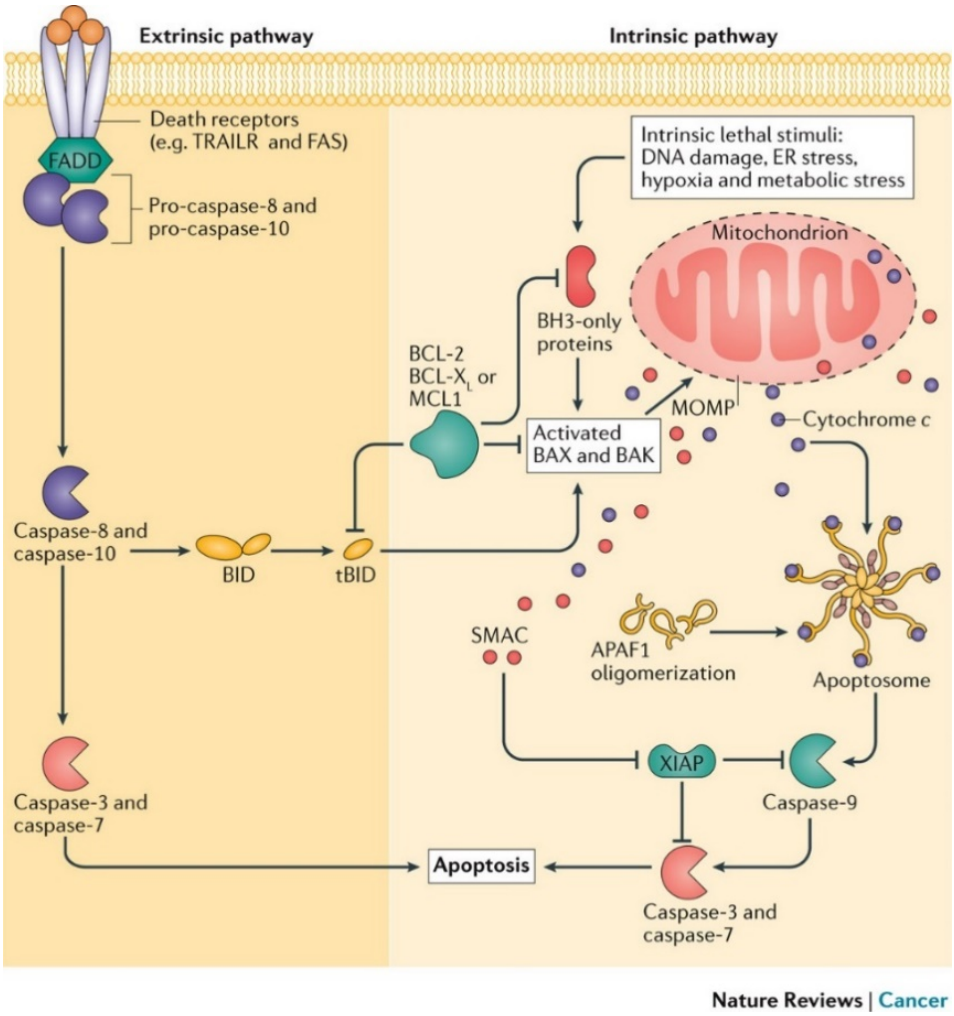

Figure 5 Schematic of the intrinsic and extrinsic apoptosis pathway

The extrinsic apoptosis pathway is activated upon binding of a ligand, such as TRAIL, to its designated receptor, TRAILR. The binding of adapter proteins, such as FADD, then leads to the recruitment and activation of Caspase-8 or caspase-10 and subsequent activation of the effector caspases caspase-3 or caspase-7, leading to apoptosis. The intrinsic apoptosis pathway is activated through intrinsic stimuli, such as DNA damage or ER stress, which engage the BH3-only proteins. These proteins activate BAX and BAK, leading to rapid mitochondrial outer membrane permeabilization (MOMP). Following MOMP, apoptotic proteins like cytochrome c are released into the cytoplasm and can contribute to the recruitment of APAF1 and the subsequent formation of the apoptosome. Apoptosome assembly triggers caspase-9 activation, which in turn activates effector caspases caspase-3/7, leading to rapid apoptosis. A crosstalk between the extrinsic and intrinsic apoptosis pathway exists in caspase-8 mediated cleavage of BH3-only protein BID. Figure taken from (Ichim & Tait, 2016).

2.3.2.4 Extrinsic pathway of apoptosis

The extrinsic pathway (Figure 5), also called death receptor pathway (Igney & Krammer, 2002), is mainly induced by immune cells and is a mechanism by which the immune system eliminates damaged cells. It is initiated by the binding of a ligand to a cell's so-called death receptor (D'Arcy, 2019). Such ligands can be expressed on the cell surface of an immune cell or they can be present as soluble factors. Several pairs of death receptors and death ligands exist, such as TNFR1/2 and TNF (Gon et al., 1996), TRAIL-R1/R2 and TRAIL (Schneider, Thome, et al., 1997), or FAS and FAS-L (Schneider, Bodmer, et al., 1997). Upon ligand binding, the death-inducing signal complex (DISC) is formed, consisting of adapter molecules, such as FADD or TRADD, and pro-caspase-8 or 10 (Micheau & Tschopp, 2003). Dimerization of pro-caspase-8/10 results in their activation through auto-catalytic cleavage (Muzio et al., 1998). Active caspase-8/10 then directly cleaves the effector caspases pro-caspase-3/7, leading to rapid cell death (Seol et al., 2001). In some instances, the extrinsic pathway can converge with the intrinsic pathway through caspase-8-mediated cleavage of the BH3-only protein BID (Li et al., 1998; Luo et al., 1998).

Upon activation of the non-canonical pathway, RIPK1 is recruited to the DISC and induces apoptosis through caspase-8. In the absence of caspase-8, RIPK1 recruitment to the DISC induces necroptosis, representing one of the many ways in which different cell death types can converge and are sometimes difficult to separate (L. Zheng et al., 2006).

2.3.3 Other forms of cell death

2.3.3.1 Necroptosis

Necroptosis (Figure 6a) is a pro-inflammatory form of regulated cell death. It can be induced, similarly to apoptosis, through death-receptor signaling, i.e., Fas/FasL (Holler et al., 2000). Toll-like receptors (TLR) such as TLR3 or TLR4 also induce necroptotic cell death (S. He et al., 2011). Receptor activation leads to the binding of the adapter molecules FADD, TRADD, or TRIF. RIPK1 and caspase-8 are then recruited to the complex (Tenev et al., 2011). While active caspase-8 induces apoptosis, inactive or absent caspase-8 leads to the recruitment and phosphorylation of RIPK3 by RIPK1 (Cho et al., 2009). The newly formed complex recruits and phosphorylates MLKL to form the so-called necrosome (Zhao et al., 2012). MLKL opens calcium or sodium channels and directly forms pores in the plasma membrane, leading to swelling and cell rupture (Cai et al., 2014; Su et al., 2014). The process culminates in the massive release of damage-associated molecular patterns (DAMPs) into the surrounding tissue, resulting in strong immune activation. Cytosolic nucleic acid sensors like STING or RIG-I also induce necroptosis through TNF and type I interferon production and a resultant autocrine feedback loop (Brault et al., 2018).

2.3.3.2 Pyroptosis

Pyroptosis (Figure 6b) is a regulated type of cell death that results in the massive release of pro-inflammatory molecules into the surrounding tissue. It is induced by the activation of so-called inflammasome sensors by DAMPs or pathogen-associated molecular patterns (PAMPs) (X. Liu et al., 2016). The activated sensors oligomerize and activate caspase-1 (Martinon et al., 2002), which cleaves gasdermin D (GSDMD), leading to oligomerization and formation of

pores in the plasma membrane (X. Liu et al., 2016). Water is able to enter the cell through these GSDMD pores, leading to cell swelling. At the same time, caspase-1 cleaves the proforms of interleukin (IL)-1β and IL-18, generating mature inflammatory cytokines, which are then released into the surrounding microenvironment through the GSDMD pores (Bertheloot et al., 2021; Cerretti et al., 1992; Evavold et al., 2018). In the advanced stages of pyroptosis, membrane destabilization through GSDMD pores and cell swelling lead to cell lysis and subsequent massive release of DAMPs into the surrounding tissue.

In the non-canonical pyroptosis pathway, intracellular recognition of lipopolysaccharides (LPS) can activate caspase-4/5, which will then induce a similar cascade as caspase-1 in the canonical pathway (J. Shi et al., 2015).

Interestingly, recent reports have hinted at an interplay between apoptosis and pyroptosis where activated caspase 3 was able to cleave and activate gasdermin E (GSDME), leading to pyroptosis (Y. Wang et al., 2017). However, more research is needed to dissect these mechanisms. Although pyroptosis was first identified and has primarily been observed in the context of immune cells (Bertheloot et al., 2021), several publications have also described this form of cell death in other cell types, such as keratinocytes (Deng et al., 2022) or lung cancer cells (C. Zhang et al., 2019).

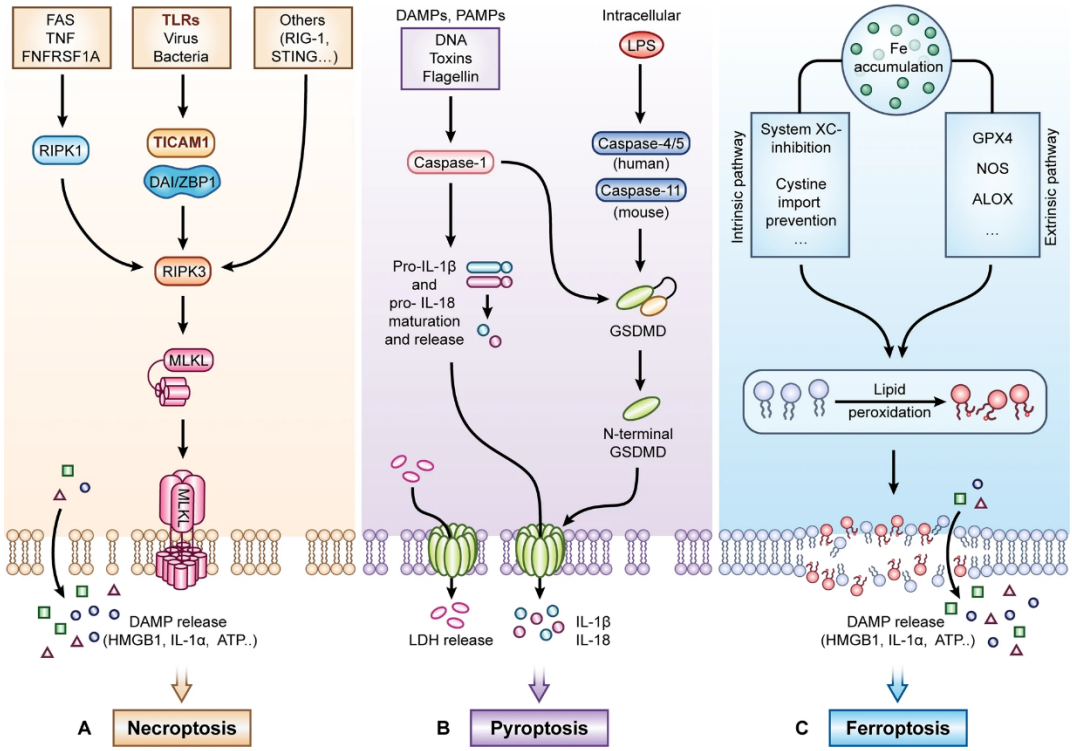

Figure 6: Molecular pathways of necroptosis, pyroptosis, and ferroptosis.
(**a**) Necroptosis is initiated via death receptor signaling (FAS or TNF binding to their designated receptors) or TLR signaling. It is characterized by the activation of RIPK3 and subsequent activation and pore formation of MLKL. Pore formation in the cell membrane leads to the release of DAMP into the surrounding tissue. (**b**) Pyroptosis is initiated by cellular recognition of DAMPs or PAMPs and subsequent activation of caspase-1 and gasdermin D (GSDMD) with GSDMD-mediated pore formation. This cell death culminates in the release of pro-inflammatory cytokines, cell swelling, and cell rupture. (**c**) Ferroptosis is an iron-dependent form of cell death characterized by the peroxidation of lipids in the cell membrane. This leads to damage of the cell membrane and subsequent release of DAMPs into the surrounding tissue. Figure taken from (G. Zhang et al., 2022)

2.3.3.3 Ferroptosis

Ferroptosis (Figure 6c) is characterized by an intracellular accumulation of iron and reactive oxygen species (ROS) (Dixon et al., 2012). Both intracellular iron and ROS are usually tightly controlled, and their accumulation leads to the peroxidation of lipids in the plasma membrane through the so-called Fenton reaction (Conrad & Pratt, 2019). Lipid peroxidation causes destabilization of the cell membrane and subsequent leakage of intracellular components into the surrounding tissue and cell death (X. Jiang et al., 2021). Ferroptosis can be induced by an intracellular and an extracellular pathway.

The intrinsic pathway is initiated by the deregulation of the Xc-system or the transferrin receptor (Gao et al., 2015). The inhibition of the Xc-transporter leads to a reduction in cystine uptake (Sato et al., 1999), an essential building block for the biosynthesis of the antioxidant glutathione (Meister, 1995). Alternatively, activation of the transferrin transporter leads to increased iron import into the cell (Gao et al., 2015).

The extrinsic pathway is induced by inhibition of intracellular antioxidant proteins such as GPX4, which is the primary enzyme that catalyzes the reduction of peroxidized lipids in the cellular membrane (Ursini et al., 1982; Yang et al., 2014).

2.4 Regulation of the actin cytoskeleton

The actin cytoskeleton is essential for every mammalian cell and is involved in a multitude of cellular processes. It not only mediates cell motility, cell shape, and cell division but is also essential in the formation and trafficking of intracellular organelles and vesicles (Rottner et al., 2017). The dynamics of the actin cytoskeleton are tightly regulated. Cellular actin is polymerized from monomeric globular actin (G-Actin) to actin filaments (F-actin) (Fujii et al., 2010) by actin nucleators or nucleation complexes (Pollard & Cooper, 2009). Spontaneous polymerization is prevented by G-actin sequestering proteins (Xue & Robinson, 2013). There are three major actin nucleators: The actin related protein 2/3 (ARP2/3) complex (Machesky & Insall, 1998), the formins (Pruyne et al., 2002), and tandem actin-binding domain nucleators, such as COBL (Ahuja et al., 2007). The involvement of each of these nucleators depends on the localization and particular function of the actin structure. Strikingly, the ARP2/3 complex is involved in almost all areas of actin dynamics. One example is the ARP2/3 complex mediated lamellipodia formation, which are cell protrusions important in cell exploration and migration (Suraneni et al., 2012). Further, the formation of invadosomes, essential for cell adhesion, invasion, and interaction with the extracellular matrix, heavily depends on ARP2/3 activation (Linder et al., 2000). Moreover, stress fibers, which are long fibers that can span the entirety of the cell, are regulated in a ARP2/3 dependent manner (Maekawa et al., 1999; Pellegrin & Mellor, 2007). The ARP2/3 complex is activated by nucleation-promotion factors of the Wiskott-Aldrich syndrome protein (WASP)-family (Linder et al., 2000). Interestingly, actin nucleation is often driven by the activity of Rho family GTPases, such as CDC42, Rho (Otomo et al., 2005; Rohatgi et al., 1999), and the Rho-associated protein kinase 1 (ROCK1) (Maekawa et al., 1999; Pellegrin & Mellor, 2007). The dynamic process of actin remodeling is further completed by actin elongation factors, which include the VASP family of actin filament polymerases (Brühmann et al., 2017), and actin disassembly factors, such as members of the cofilin family (Kanellos & Frame, 2016).

2.5 Aim of the study

Lung cancer accounts for the most cancer-related deaths worldwide, and mortality is expected to increase steeply in the coming years (Wéber et al., 2023). LuAD is the most prevalent subtype, comprising more than 60% of all lung cancer cases. It is characterized by a diverse spectrum of oncogenic driver mutations, of which only a small percentage is actionable by targeted therapeutics (Skoulidis & Heymach, 2019). This highlights the need to identify novel vulnerabilities and therapy approaches beyond the level of genetic modifications.

Investigating the involvement of post-translational modifications, such as ubiquitination, in the maintenance of LuAD holds great promise, as the ubiquitin-proteasome system (UPS) is often deregulated in cancer (D. Shi & Grossman, 2010). Further, targeting or harnessing the UPS, for instance through proteasome inhibitors (W. K. K. Wu et al., 2010) or targeted protein degraders (Békés et al., 2022), respectively, has been a successful strategy in the development of anti-cancer therapeutics.

The aims of this study were, therefore, i) to perform a CRISPR/Cas9-based dropout screen to identify novel vulnerabilities within the ubiquitin system, ii) to characterize the molecular function of the newly identified vulnerability in LuAD, and iii) to identify relevant ubiquitination substrates by cross-validation of mass spectrometry-based interactome screens and functional proteomics.

3 Material

3.1 Devices and instruments

Device	Supplier
Accuri C6 plus	BD Biosciences
Aqualine water bath	Lauda-Brinkmann
Axiovert 40 CFL with HBO50	Carl Zeiss
BioSAFE SC-smart CHRONOS 220	Cryotherm
BransonSonifier 250	Heinemann
Centrifuge 5417R with rotor F453011	Eppendorf
Centrifuge 5424 with rotor FA452411	Eppendorf
ChemiDoc MP Imaging System	Bio-Rad Laboratories
Concentrator plus	Eppendorf
Curix 60	Agfa
ENVAIReco safe Comfort Sterilwerkbänke	ENVAIR
FACS Aria Fusion	BD Biosciences
Fridges and freezers	Liebherr
Gel IX IMAGER 20	INTAS
GloMax Explorer Multimode Microplate Reader	Promega
HERAcell 150i CO2 incubator	ThermoFisher Scientific
HERAfreeze	ThermoFisher Scientific
HERASafe KS safety cabinet	ThermoFisher Scientific
HypercassetteTM	Amersham Biosciences
Innova 40 shaker for bacteria	New Brunswick Scientific
Invitrogen Chamber for Ready Gels	Invitrogen
Magnetic Themo Stirrer RCT Basic	IKA Laboratory Equipment
Mastercycler nexus	Eppendorf
Mini-PROTEAN Tetra Cell SDS Electrophoresis System	Bio-Rad Laboratories
Mini-Sub® Cell GT system for agarose gel electrophoresis	Bio-Rad Laboratories
MiSeq system	Illumina
Multifuge 3SR+	ThermoFisher Scientific
NanoPhotometer	Implen
Neubauer Chamber	Marienfeld
Novex Mini Cell System for precast NuPAGE gels	ThermoFisher Scientific
Orbitrap Eclipse Tribrid Tribrid Mass Spectrometer	ThermoFisher Scientific
Orbitrap Fusion Lumos Tribrid Mass Spectrometer	ThermoFisher Scientific
peqSTAR Thermocycler	Peqlab Biotechnology
Pipetman Neo	Gilson
Polymax 1040 Platform Shaker	Heidolph Instruments
PowerPac Basic Power Supply	Bio-Rad Laboratories
PowerPac HC Power Supply	Bio-Rad Laboratories
Precision balance 572-37	Kern & Son
QuantStudioTM 5 Real-Time-PCR machine	ThermoFisher Scientific

Quintix Analytical Balance	Sartorius
Rotina 380R centrifuge	Hettich
RS-VA 10 Vortexer	Phoenix Instrument
Scanner V850 Pro	Epson
Sep-Pak vacuum extraction manifold	Waters Milipore
SevenCompact pH/Ion pH-meter	Mettler-Toledo
SP8 Confocal Microscope	Leica Microsystems
Thermo block MBT250	Kleinfeld Labortechnik
Thermomixer Compact	Eppendorf
Tube Rotator	Fröbel Labortechnik
Tumbling Roller Mixer RM5	Neolab

3.2 Consumables

Consumable	Supplier
3mm CHR paper (Whatman)	GE Healthcare
Cell culture flasks	Greiner Bio-One
Cell culture plates	Biochrom/Falcon/Techno
Cell scraper	Sarstedt
CL-XPosure Films	ThermoFisher Scientific
Empore Solid Phase Extraction Disks	3M
Glass Cover slips for microscope slides	Sarstedt
Hypodermic needles	Braun
Immobilon-P PVDF transfer membrane	Merck Millipore
Insulin syringes Microfine Plus 29G	BD Biosciences
MicroAmp Fast 96-Well Reaction Plate	Applied Biosystems
MicroAmp Optical Adhesive Film	Applied Biosystems
PCR Tubes	VWR
Pierce Protein Concentrators PES 10K MWCO	ThermoFisher Scientific
Pipette tips	Sarstedt
Reagent reservoirs	VWR
SafeSeal tubes	Sarstedt
Serological pipettes	Greiner Bio-One
Syringe filters	TPP/Biochrom
Syringes	Braun
UVette routine pack	Eppendorf
x-well chamber slides on PCA detachable	Sarstedt

3.3 Chemicals and reagents

Reagent	Supplier
ß-Glycerolphosphate disodium salt hydrate (G-2-P)	Sigma-Aldrich
ß-Mercaptoethanol	Sigma-Aldrich

2-Chloracetamide (CAA)	Sigma-Aldrich
2-Propanol	Carl Roth
3-(N-morpholino)propanesulfonic acid (MOPS)	Sigma-Aldrich
3x FLAG Peptide	Sigma-Aldrich
4-Methylmorpholine	Sigma-Aldrich
Acetic acid glacial	Carl Roth
Acetone	Carl Roth
Acetonitrile (ACN)	Sigma-Aldrich
Agarose NEEO	Carl Roth
Albumin Fraction V (BSA)	Carl Roth
Ammonium persulfate (APS)	Sigma-Aldrich
Ampicillin sodium salt	Sigma-Aldrich
Anti-FLAG M2 Affinity Gel	Sigma-Aldrich
Aprotinin from bovine lung	Sigma-Aldrich
Aqua ad injectable, sterile	B. Braun Melsungen
Bacto Agar	BD Diagnostics
Bacto Tryptone	BD Diagnostics
Bacto Yeast Extract	BD Diagnostics
BES buffered saline	Sigma-Aldrich
Blasticidin S HCl	ThermoFisher Scientific
Boric acid	Sigma-Aldrich
Brilliant Blue R-250	Carl Roth
Bromphenol Blue	Sigma-Aldrich
Calcium chloride dihydrate	Sigma-Aldrich.
CS&T Beads	BD Biosciences
Deoxycholic acid sodium salt	Sigma-Aldrich
Di-sodium hydrogene phosphate dihydrate	Merck Milliprore
Dimethyl pimelimidate (DMP)	Sigma-Aldrich
Dimethylsulfoxid (DMSO)	Carl Roth
Disodium Phosphate	Carl-Roth
DL-Dithiothreitol	Sigma-Aldrich
DNA Loading Dye (6x)	ThermoFisher Scientific
DNA Stain Clear G	SERVA Electrophoresis
dNTP Mix, 10 mM each	ThermoFisher Scientific
Dodecylsulfate-Na-salt (in pellets, SDS)	SERVA
Doxycyline Monohydrat	Sigma-Aldrich
Ethanol	Merck
Ethanolamine	Alfa Aesar
Ethylene-bis(oxyethylenenitrilo)tetraacetic acid (EGTA)	Sigma-Aldrich
Ethylenediaminetetraacetic acid (EDTA)	Sigma-Aldrich
FACS Clean	BD Biosciences
FITC Annexin V	BD Biosciences
Fluoride ion solution (NaF)	Sigma-Aldrich
Formaldehyde (16 % w/v) (PFA)	ThermoFisher Scientific

Formic acid (FA)	Merck
Gelatin from cold water fish skin	Sigma-Aldrich
Glucose	Sigma-Aldrich
Glycerol	Sigma-Aldrich
Glycine	Carl Roth
Hexadimethrine bromide (polybrene)	Sigma-Aldrich
Hexanucleotide Mix, 10x conc.	Roche
Hoechst33342	Sigma-Aldrich
Hydrochloric acid 32%	Carl Roth
Hydrochloric acid fuming 37%	Carl Roth
Leupeptin	Sigma-Aldrich
Liproxstatin-1	MedChem Express
Lipofectamine 2000 Reagent	ThermoFisher Scientific
Lipofectamine RNAiMAX	ThermoFisher Scientific
Live/dead Fixable Dead Cell Stain APC-coupled	ThermoFisher Scientific
Magnesium chloride anhydrous	Sigma-Aldrich
Magnesium sulfate anhydrous	Sigma-Aldrich
Methanol	J. T. Baker
MG132	Biotechne/Tocris Bioscience
Necrostatin-1	MedChem Express
N-(2-Hydroxyethyl)piperazine-N-2-ethane sulfonic acid (HEPES)	SERVA
N-p-Tosyl-L-phenylalanine chloromethyl ketone (TPCK)	Sigma-Aldrich
N,N,N`,N``-tetramethyl-ethylenediamine (TEMED)	Sigma-Aldrich
Nonidet P-40 substitute (10%)	Roche
NuPAGE MES SDS Running buffer (20x)	ThermoFisher Scientific
Nα-Tosyl-L-lysine chloromethyl ketone hydrochloride (TLCK)	Sigma-Aldrich
PBS Dulbecco, powder	Merck Millipore/Biochrome
Pepstatin A	Selleckchem
Phalloidin-iFluor 647 Conjugate	AAT Bioquest
Phenylmethanesulfonylfluoride solution (PMSF)	Sigma-Aldrich
PI/RNase staining buffer	BD Pharmingen
Ponceau S solution	Sigma-Aldrich
Potassium chloride	Sigma-Aldrich
PowerUPTM SYBRTM Green Master Mix	ThermoFisher Scientific
ProLong Diamond Antifade Mountant	ThermoFisher Scientific
Protein G Agarose, Fast Flow	Sigma-Aldrich
Puromycin	ThermoFisher Scientific
RNaseOUT Recombinant Ribonuclease Inhibitor	ThermoFisher Scientific
Rotiphorese NF-Acrylamide/Bis-solution 40% (29:1)	Carl Roth
Saponin	Sigma-Aldrich
Sera-Mag SpeedBead Carboxylate-modified Magnetic particles A	Cytiva
Sera-Mag SpeedBead Carboxylate-modified Magnetic particles B	Cytiva
Sheath Additive	BD Biosciences
Skim Milk Power	Sigma-Aldrich

Sodium acetate	Merck
Sodium azide	Merck
Sodium carbonate	Merck
Sodium chloride	Carl Roth
Sodium dihydrogen phosphate monohydrate	Merck
Sodium fluoride	Sigma-Aldrich
Sodium hydroxide solution 45%	Carl Roth
Sodium orthovanadate	Sigma-Aldrich
Sodium phosphate dibasic	Sigma-Aldrich
Sodium tetraborate decahydrate (Borax)	Sigma-Aldrich
Sodium thiosulfate pentahydrate	Sigma-Aldrich
SuperSignal West Femto Max. Sensitivity Substrate	ThermoFisher Scientific
SuperSignal West Pico Chemiluminescent Substrate	ThermoFisher Scientific
TMT10plex	ThermoFisher Scientific
Trichloroacetic acid solution (TCA)	Sigma-Aldrich
Trifluoroacetic acid (TFA)	Sigma-Aldrich
TRIS	Carl Roth
Tris Buffered Saline (10x)	Sigma-Aldrich
TRIS-acetat-EDTA (TAE) buffer (50x)	ThermoFisher Scientific
Tris(2-carboxyethyl)phosphin-hydroshlorid (TCEP)	Merck
Triton X-100	Sigma-Aldrich
Trypsin inhibitor from soybean	Sigma-Aldrich
Tween 20	Sigma-Aldrich
Z-VAD-FMK	MedChemExpress

3.4 Commercial kits

Kit	Supplier
DC Protein Assay	Bio-Rad Laboratories
DNeasy Blood & Tissue Kit	Qiagen
GeneJET Gel Extraction Kit	ThermoFisher Scientific
In-FusionR HD Cloning Kit	Takara Bio USA
JC-1 Mitochondrial Membrane Potential Assay Kit	Cayman Chemicals
NucleoBond Xtra Midi	MACHEREY-NAGEL
peqGOLD Plasmid Miniprep Kit	Peqlab
Pierce BCA Protein Assay	ThermoFisher Scientific
Pierce Silver staining kit	ThermoFisher Scientific
PTMScan Ubiquitin Remnant motif (K-e-GG) Kit	Cell Signaling Technology
QIAshredder	Qiagen
QIAquick PCR purification kit	Qiagen
Rapid DNA Dephos & Ligation Kit	Roche
RNase-Free DNase Set	Qiagen
RNeasy Mini Kit	Qiagen

3.5 Enzymes

Enzyme	Supplier
AgeI (BshTI)	ThermoFisher Scientific
BamHI	ThermoFisher Scientific
EcoRI	ThermoFisher Scientific
KspAI (HpaI)	ThermoFisher Scientific
XbaI	ThermoFisher Scientific
NheI	ThermoFisher Scientific
Q5 DNA-polymerase	New England Biolabs
SuperScript III Reverse Transcriptase	Invitrogen

3.6 Oligonucleotides

All oligonucleotides were purchased from Eurofins Genomics, Ebersberg, Germany. Nucleotide sequences are written in 5' to 3' direction.

3.6.1 Cloning oligonucleotides

InFusion_DCAF13_SF_fw	TTCGAGAAAGGAGCTATGAAGGTGAAGATGCTGAG
InFusion_DCAF13_SF_fw	AATAGGGCCCTCTAGTTATTTTACAACTGCCACTACGTGT
InFusion_DCAF13_pHIV_fw	AGCGGCCGCTGAGTTATGGATTATAAAGATGATGATGATA AAGG
InFusion_DCAF13_pHIV_fw	GGAGAGGGGCGGATCTTATTTTACAACTGCCACTACGTGT TTC

3.6.2 sgRNA sequences

sgNT	ACGGAGGCTAAGCGTCGCAA
sgPOLR2I	GAACCGCATTCTGCTCTACG
sgDCAF13_1	ACCAAGTTGGACTTACAGAG
sgDCAF13_2	ATTACATACAATATTAGGAA

3.6.3 shRNA sequences

shCTRL	CCTAAGGTTAAGTCGCCCTCG
shDCAF13_1	AGAGCCATTACATACAATATT
shDCAF13_2	TCACCGTGATGGAGTCAATTG
shDCAF13_3	GAATCTAACTCAGCGGAATTG

3.6.4 siRNA sequences

siRNA	Sequence	Origin
siDCAF13 pool	CGAUAAAUCUAUUCGAAUC	Dharmacon (J-017898-09)
	GGAAUCUAACUCAGCGGAA	Dharmacon (J-017898-10)
	CGAAAGGAAGUGAAUCGUA	Dharmacon (J-017898-11)
	ACGUAUAGCUCGUCAUCGA	Dharmacon (J-017898-12)
siNT pool	UGGUUUACAUGUCGACUAA	Dharmacon (D-001810-10)
	UGGUUUACAUGUUGUGUGA	Dharmacon (D-001810-10)
	UGGUUUACAUGUUUUCUGA	Dharmacon (D-001810-10)
	UGGUUUACAUGUUUUCCUA	Dharmacon (D-001810-10)

3.6.5 Sequencing primers

pHIV seq_fw	TGGAATTTGCCCTTTTTGAG
pHIV seq_rv	AGGAACTGCTTCCTTCACGA
pTRI2A seq_fw	GTGGGAGGCCTATATAAGCAG
pTRI2A seq_rv	GCGGGCCGCTGTCCTGAG
pcDNA3_for	GGCTAACTAGAGAACCCACTG
pcDNA3_rev	GGCAACTAGAAGGCACAGTC

3.6.6 qPCR primers

RPLP0 qPCR_fw	GCACTGGAAGTCCAACTACTTC
RPLP0 qPCR_rv	TGAGGTCCTCCTTGGTGAACAC
DCAF13 qPCR fw	TTTCCTGTAGACAAAAGTCGAAGCA
DCAF13 qPCR rv	GCATTAGCTTTCCACAGGCG
RP7_fw_qCPR	CAAGCAGAAGACGGCATACGAG
FP5_rv_qPCR	ATGATACGGCGACCACCGAG

3.6.7 Oligos for CRISPR Screen multiplexing

The underscored letters in the primer represent the barcode sequence

sgRNA_NGS-P501	AATGATACGGCGACCACCGAGATCTACACTAGATCCACCGACTCGGTGCCACTTTT
sgRNA_NGS-P502	AATGATACGGCGACCACCGAGATCTACACCTCTCTCACCGACTCGGTGCCACTTTT
sgRNA_NGS-P503	AATGATACGGCGACCACCGAGATCTACACTATCCTCACCGACTCGGTGCCACTTTT
sgRNA_NGS-P504	AATGATACGGCGACCACCGAGATCTACACAGAGTACACCGACTCGGTGCCACTTTT
sgRNA_NGS-P701	CAAGCAGAAGACGGCATACGAGATGCCTTATTTCTTGGGTAGTTTGCAGTTTT
sgRNA_NGS-P702	CAAGCAGAAGACGGCATACGAGATAGTACGTTTCTTGGGTAGTTTGCAGTTTT
sgRNA_NGS-P703	CAAGCAGAAGACGGCATACGAGATCTGCCTTTTCTTGGGTAGTTTGCAGTTTT
sgRNA_NGS-P704	CAAGCAGAAGACGGCATACGAGATTCAGGATTTCTTGGGTAGTTTGCAGTTTT
sgRNA_NGS-P705	CAAGCAGAAGACGGCATACGAGATGAGTCCTTTCTTGGGTAGTTTGCAGTTTT

3.7 Plasmids

Plasmid	Origin
pcDNA 3.1(+) Zeo Empty vector	ThermoFisher Scientific
pcDNA 3.1 (C)-FLAG-CTNND1	Genscript # NM_001085461.1
pcDNA 3.1 (C)-FLAG-CDC42	Genscript # NM_001791.4
pcDNA 3.1 FLAG-EV	F. Bassermann
pcDNA 3.1 HA-Ubiquitin	Addgene (#17608), T. Dawson
pcDNA 3.1 SF-EV	M. Ueffing
pcDNA 3.1 (N)-SF-DCAF13	V. Wagner, this study
pHIV puro SF-EV	C. Dürr, this study
pHIV puro (N)-SF-DCAF13	C. Dürr, this study
pLenti Cas9 Blast	Addgene (#52962), F. Zhang
pLenti CRISPR GFP DCAF13 sgRNA_1	V. Wagner, this study
pLenti CRISPR GFP DCAF13 sgRNA_2	V. Wagner, this study
pLenti CRISPR GFP non-targeting control	O. Karpiuk
pLenti CRISPR GFP POLII sgRNA	O. Karpiuk
pLenti CRISPR mCherry non-targeting control	O. Karpiuk
pLKO.1 DsRed DCAF13 shRNA_1	V. Wagner, this study
pLKO.1 DsRed DCAF13 shRNA_2	V. Wagner, this study
pLKO.1 DsRed DCAF13 shRNA_3	V. Wagner, this study
pLKO.1 DsRed scrambled control	M. Heider
pLKO.1 Tet puro DCAF13 shRNA_1	V. Wagner, this study
pLKO.1 Tet puro DCAF13 shRNA_2	V. Wagner, this study
pLKO.1 Tet puro DCAF13 shRNA_3	V. Wagner, this study
pLKO.1 Tet puro non-targeting control	R. Spallek
pMD2.G	Addgene (#12259), D. Trono
psPAX2	Addgene (#12260), D. Trono
pXPR-003 ubiquitin sgRNA library	M. Weiss

3.8 Bacteria

Product	Supplier
NEB 5-alpha competent *E.coli*	New England Biolabs

3.9 Standards for DNA and protein analysis

Product	Supplier
GeneRuler 1 kb DNA Ladder	ThermoFisher Scientific
PageRuler Plus Prestained Protein Ladder	ThermoFisher Scientific
KAPA Library Quant (Illumina) DNA Standards 1-6	Roche

3.10 Antibodies

Antibody (clone)	Dilution (application)	Supplier
Caspase-3 (8G10)	1:1000 (IB)	Cell Signaling (9665S)
Caspase-8 (1.1.40)	1:200 (IB)	Santa Cruz (sc-81656)
Centrin-3 (SS12)	1:400 (IF)	Santa Cruz (sc-100933)
Cleaved caspase-3 (Asp175)	1:400 (IB)	Cell Signaling (9664S)
CUL1 (2H4C9)	1:1000 (IB)	Invitrogen (32-2400)
CUL4A	1:1000 (IB)	Bethyl Laboratories (A300-739A)
CUL4B	1:1000 (IB)	Proteintech (12916-1-AP)
DCAF13 (EPR18723)	1:1000 (IB)	Abcam (ab195121)
DCAF13	1:50 (IF)	Sigma-Aldrich (HPA044504)
DDB1	1:1000 (IB)	Bethyl Laboratories (A300-462A)
Donkey anti-mouse IgG-AF488	1:1000 (IF)	Invitrogen (A21202)
Donkey anti-rabbit IgG-AF594	1:1000 (IF)	Invitrogen (A21207)
ECL anti-mouse IgG, HRP-linked	1:10,000 (IB)	GE Healthcare (NA931)
ECL anti-rabbit IgG, HRP-linked	1:10,000 (IB)	GE Healthcare (NA934)
FLAG	1:1000 (IB)	Sigma-Aldrich (F7425)
FLAG-M2	1:1000 (IB)	Sigma-Aldrich (F3165-1MG)
GAPDH (0411)	1:1000 (IB)	Santa Cruz (sc-47724)
GSDMDC1 (64-Y)	1:200 (IB)	Santa Cruz (sc-81868)
HA-tag (16B12)	1:1000 (IB)	Biolegend (901501)
PARP1 (F-2)	1:200 (IB)	Santa Cruz (sc-8007)
α/β-Tubulin	1:1000 (IB)	Cell Signaling (2148S)

3.11 Cell line models

Cell line	Type	Distributor	Culture Media
A549	Epithelial like LC	ATCC (CRM-CCL-185)	DMEM + 10% FBS
HCC-44	LuAD	DSMZ (ACC 534)	RPMI1640 + 10% FBS
HCC827	LuAD	ATCC (CRL-2868)	RPMI1640 + 10% FBS
HEK293T	Embryonic kidney	ATCC (CRL-3216)	DMEM + 10% NCS
IMR-90	Lung fibroblast	Kind gift of Dr. F. Bassermann	EMEM + 10% FBS
NCI-H1417	SCLC	ATCC (CRL-5869)	RPMI1640 + 10% FBS
NCI-H1437	LuAD	ATCC (CRL-5872)	RPMI1640 + 10% FBS
NCI-H1650	LuAD	ATCC (CRL-5883)	RPMI1640 + 10% FBS
NCI-H1703	LuSC	ATCC (CRL-5889)	RPMI1640 + 10% FBS
NCI-H1792	LuAD	ATCC (CRL-5895)	RPMI1640 + 10% FBS
NCI-H1975	LuAD	ATCC (CRL-5908)	RPMI1640 + 10% FBS
NCI-H2087	LuAD	ATCC (CRL-5922)	RPMI1640 + 10% FBS
NCI-H2228	LuAD	ATCC (CRL-5935)	RPMI1640 + 10% FBS
NCI-H23	LuAD	ATCC (CRL-5800)	RPMI1640 + 10% FBS
NCI-H460	LCLC	ATCC (HTB-177)	RPMI1640 + 10% FBS

NCI-H520	LuSC	ATCC (HTB-182)	RPMI1640 + 10% FBS
NCI-H661	LCLC	ATCC (HTB-183)	RPMI1640 + 10% FBS
NCI-H748	SCLC	ATCC (CRL-5841)	RPMI1640 + 10% FBS
SCLC-21H	SCLC	DSMZ (ACC 372)	DMEM + 10% FBS
WI-38	Lung fibroblast	ATCC (CCL-75)	EMEM + 10% FBS

3.12 Cell culture media and supplements

Product	Supplier
Dulbecco's Modified Eagle's Medium (DMEM)	ThermoFisher Scientific
Eagle's Minimum Essential Medium (EMEM)	Bio&Sell
Fetal Bovine Serum (FBS) superior	Merck Millipore/Biochrom
Newborn Calf Serum (NCS)	Merck Millipore/Biochrom
Opti-MEM I, reduced serum media	ThermoFisher Scientific
Phosphate buffered saline (PBS), 10X, sterile	ThermoFisher Scientific
Penicillin/ Streptomycin (100X)	ThermoFisher Scientific
RPMI 1640 GlutaMAX medium	ThermoFisher Scientific
Trypan Blue Stain (0,4%)	ThermoFisher Scientific
Trypsin-EDTA (10X) solution	Merck Millipore/Biochrome

3.13 Solutions and buffers

Annexin V binding buffer (10x)	100 mM HEPES 1.4 M NaCl 25 mM $CaCl_2$
Borax buffer	100 mM Borax (pH 8.8)
Coomassie destaining solution	45% methanol (v/v) 10% acetic acid (v/v)
Coomassie staining solution	45% methanol (v/v) 10% acetic acid (v/v) 0.25% Brilliant Blue R-250 (w/v)
DiGLY blocking buffer	200 mM ethanolamine (PH 8.0)
DiGLY elution buffer	0.15% trifluoroacetic acid (v/v)
FACS buffer	PBS (1x) 2% FBS (v/v)

Freezing medium	90% FBS (heat inactivated) 10% DMSO (v/v)
IF blocking buffer	PBS (1x) 0.25% gelatin from cold water fish skin (w/v) 0.01% Saponin (w/v)
IF permeabilization buffer	PBS (1x) 0.1% Triton-X-100 (v/v)
IF staining buffer	PBS (1x) 0.5% BSA (w/v) 0.01% saponin (w/v)
Immuno Affinity Purification (IAP) buffer	50 mM MOPS (pH 7.2) 10 mM Na_2HPO_4 50 mM NaCl
Inhibitors in lysis buffer	1 µg/ml aprotinin 1 mM DTT 10 mM G-2-P 1 µg/ml leupeptin 0.1 mM PMSF 0.1 mM Na3VO4 10 µg/ml soybean trypsin inhibitor 5 µg/ml TLCK 10 µg/ml TPCK
Laemmli buffer (5x)	300 mM TRIS (pH 6.8) 10% SDS (w/v) 5% β-mercaptoethanol (v/v) 0.05% bromphenol blue (w/v) 50% glycerol (v/v)
Luria-Bertani (LB) medium (1x)	1% Bacto Tryptone (w/v) 0.5% Bacto Yeast Extract (w/v) 170 mM NaCl
LB-agar plates	1.5% Bacto Agar (w/v) LB medium

Lysis buffer (150 mM NaCl)	50 mM TRIS (pH 7.5) 150 mM NaCl 0.1% NP40 (v/v) 5 mM EDTA 5 mM $MgCl_2$ 5% Glycerol (v/v)
Lysis buffer (250 mM NaCl)	50 mM TRIS (pH 7.5) 250 mM NaCl 0.1% Triton X-100 (v/v) 1 mM EDTA 50 mM NaF
SDS running buffer (10×)	250 mM TRIS (pH 7.5) 1.92 M glycine 1% SDS (w/v)
Separating gel buffer	1.5 M TRIS (pH 8.8)
Sep-Pak Solvent A	0.1% formic acid (v/v)
Sep-Pal Solvent B	0.1% formic acid (v/v) 50% acetonitrile (v/v)
Stacking gel buffer	0.5 M TRIS (pH 6.8)
StageTip Solvent A	0.1% formic acid (v/v)
StageTip Solvent B	0.1% formic acid (v/v) 60% acetonitrile (v/v)
Stripping buffer	62.5 mM TRIS (pH 6.8) 2% SDS 0.867% β-mercaptoethanol
Transfer buffer (10x)	48 mM TRIS (pH 7.5) 20% methanol 39 mM glycine
Washing buffer	PBS (1x) 0.1% Tween20 (v/v)

3.14 Software and databases

Software/Database	Supplier
Alphafold	DeepMind and EMBL-EBI
Basic local alignment search tool	NCBI
BioVenn	Tim Hulsen
cBioPortal	Memorial Sloan Kettering Cancer Center
CRAPome	University of Michigan and Samuel Lunenfeld Research Institute Toronto
CRISPRAnalyzeR	Jan Winter. (J. Winter et al., 2017)
DAVID	Laboratory of Human Retrovirology and Immunoinformatics
DepMap	Broad Institute
FlowJo (version 10.9.0)	BD Biosciences
GeneCards	Weizmann Institute of Science
GPP Web Portal	Broad Institute
IMARIS Viewer	Oxford Instruments
ImageJ	W.S. Rasband, U.S. National Institute of Health
Molecular Signatures Database	Broad Institute UC San Diego
Prism (version 10.0.2)	Graph Pad Software
RStudio (version 1.2.5033)	Posit
SnapGene	GSL Biotech LLC
The human protein atlas	The human protein atlas Consortium
UniProt	UniProt Consortium

4 Methods

4.1 Molecular biology

4.1.1 Molecular cloning

Molecular cloning describes the production and engineering of expression vectors commonly used in gene perturbation studies. Expression vectors are circular double-stranded DNA constructs, termed plasmids, and contain a so-called insert. The insert can range from short sequences, such as a short-hairpin RNA (shRNA)s or single guide RNA (sgRNA), to cDNA sequences of an entire gene. The insert can be synthesized synthetically by a manufacturer or generated from a template using polymerase chain reaction (PCR). Usually, the insert and plasmid are cut by restriction enzymes and subsequently ligated and amplified in bacteria to obtain the insert-containing plasmid. The following chapters describe the individual processes required for cloning.

4.1.2 Polymerase Chain Reaction (PCR)

PCR is used to amplify a DNA sequence of interest. During this study, it was primarily used to amplify cDNA. To this end, forward and reverse primers were designed that were homologous to the cDNA of the gene of interest and contained a restriction enzyme site. The enzymatic reaction was pipetted according to the manufacturer's recommendations for the Q5 polymerase-based PCR and is shown below.

Reagent	**Amount**
Q5-reaction buffer (5x)	10 µl
Forward primer (10 µM)	2.5 µl
Reverse primer (10 µM)	2.5 µl
dNTPs (10 mM)	1 µl
DNA template	100-200 ng
Q5 High Fidelity Polymerase	0.5 µl
Nuclease-free dH_2O	To 50 µl

The annealing temperature during the PCR cycle was adjusted depending on the requirements of the individual primer pair. The elongation step was adapted to fit the size of the respective target and set to 40 sec per kb of the expected product.

Program step	Temperature	Time
Initial Denaturation	98°C	30 sec
Cycles: 35		
Denaturation	98°C	10 sec
Annealing	X	50 sec
Elongation	72°C	40 sec / 1 kb
Final Elongation	72°C	2 min
Storage	8°C	Forever

4.1.3 Agarose gel electrophoresis and gel purification

Following PCR or restriction enzyme digest, the DNA was subjected to gel electrophoresis. To this end, 1-2% (w/v) agarose was dissolved in TAE buffer by heating. The liquid agarose solution was stained with 3 µl DNA Stain Clear G per 100 µl total volume. The liquid agarose was then poured into a gel chamber containing a comb and left at RT to solidify. The gel was then transferred to a gel cassette, and the chamber was filled with TAE buffer. The PCR or restriction digest reactions were mixed with 6x DNA loading dye and loaded into the gel pockets. A DNA ladder was loaded, as well. The gel was run at 125 V for 25 min. The DNA was visualized using a UV lamp, and the size was estimated by comparing it to the DNA standard. If the desired DNA fragment needed to be processed further, the desired band was excised from the gel using a scalpel and extracted using the GeneJet Gel Extraction Kit (ThermoFisher Scientific) according to the manufacturer's instructions. The purified DNA product was usually eluted in 30 µl H_2O.

4.1.4 DNA restriction digest and ligation

Bacterial restriction enzymes can cut distinct motifs in DNA sequences. This is particularly useful in molecular cloning techniques. Restriction enzymes create so-called sticky ends when there is a 3' or 5' overhang and blunt ends when both DNA strands are cut equally, and these DNA fragments can then be fused through a ligation reaction.

For the restriction digest, 1 µg plasmid or a desired amount of gel-purified PCR product (see chapter 4.1.3) was mixed with 0.5 µl of the selected restriction enzyme, its designated digest buffer, and H_2O to generate a 30 µl reaction volume. The digestion reaction was incubated at 37°C for 1 hour for most restriction enzymes unless indicated otherwise by the manufacturer. After the digest, the DNA was again subjected to agarose gel electrophoresis and subsequent gel extraction (see chapter 4.1.3). The Rapid DNA Dephos & Ligation Kit (Roche) was used to ligate an insert of choice into a plasmid according to the manufacturer's instructions. In general, 40-80 ng of insert and 120-240 ng of plasmid were used for the reaction.

4.1.5 Bacterial transformation

The process of delivering DNA into bacteria is called transformation. This is commonly used to amplify plasmids. To amplify a plasmid after ligation, 15 µl NEB 5-alpha competent *E.coli* (New England Biolabs) were incubated with 2 µl of the ligation reaction for 20 min on ice. Then, a heat shock was performed at 42°C for 45 sec, followed by an additional incubation on ice for 2 min. In the case of plasmids containing a Kanamycin resistance cassette, the bacteria were incubated with 100 µl SOC media at 37°C for 30-60 min. Transformed bacteria were then plated on LB agar plates containing the relevant antibiotics (100 µg/ml Ampicillin or 50 µg/ml Kanamycin) and incubated at 37°C or 30°C (for plasmids containing cDNA of DCAF13 to reduce recombination events) overnight. The next day, LB medium containing the respective antibiotic was inoculated with single colonies that grew on the plate and incubated overnight at 37°C or 30°C (for plasmids containing cDNA of DCAF13).

4.1.6 DNA extraction from bacterial cultures

The Nucleobond Xtra Midi Kit (Macherey-Nagel) or peqGOLD Plasmid Miniprep Kit (Peqlab) were used to extract the amplified plasmids from 200 ml or 5 ml bacterial culture, respectively. The kits were used according to the manufacturer's instructions, and the DNA pellets were solved in an appropriate volume of endotoxin-free water depending on their size (50-200 µl).

For long-time storage of transformed bacteria, 700 µl bacterial cultures were mixed with 300 µl glycerol and stored at -80°C. LB-media was inoculated with a small amount of the mixture to amplify the plasmid again.

To identify positive bacterial clones containing the correct plasmid, a test digest of the purified plasmid DNA was performed (as described in chapter 4.1.4). The plasmid was subsequently sent to Eurofins Genomics (Ebersberg, Germany) to perform sequencing with promoter or gene-specific primers and to verify the correct insertion of the DNA sequence of interest.

4.1.7 Annealing of sgRNA or shRNA oligonucleotides

Oligonucleotides for sgRNA or shRNA cloning were annealed and ligated into the pLenti CRISPR GFP or pLKO.1 DsRed and pLKO.1 Tet puro plasmid, respectively. To this end, 1 µl of forward and reverse oligonucleotide (100 µM) and Buffer G (ThermoFisher Scientific) were diluted with water to a total volume of 50 µl. The mixture was incubated in a beaker containing boiling water, which was then left on the benchtop to gradually and slowly cool down to RT. 2 µl of the annealed oligonucleotides were then ligated with 50 ng of the respective vector, which was previously digested with AgeI (ThermoFisher Scientific) and EcoRI (ThermoFisher Scientific). The ligated plasmid was subsequently transformed into NEB5a bacteria.

4.2 CRISPR/Cas9 screen

4.2.1 Sample generation

The CRISPR/Cas9 screen was performed in three LuAD cell lines that were priorly stably transduced with a Cas9-expression construct. Transduced cells were selected by adding blasticidin (10 µg/ml for HCC-44, 20 µg/ml for NCI-H23 and NCI-H1437) for two weeks and

kept under selection pressure for the experiment. Pooled lentivirus was generated from the pooled sgRNA library as described in chapter 4.4.7, and cells were transduced at a multiplicity of infection (MOI) of 0.15-0.2 to reduce the occurrence of double transduction events. Transduced cells were sorted by mCherry expression on day four post-transduction. $3.2x10^6$ sorted cells, representing coverage of 1000x of the sgRNA library with a size of 3200 sgRNAs, were immediately washed with PBS, pelleted, and frozen at -80°C (day 4 sample). Another $3.2x10^6$ sorted cells were supplemented in fresh growth media and cultured for 14 days. The coverage of 1000x was maintained while splitting the cells. After 14 days, $3.2x10^6$ cells were harvested and frozen at -80°C (day 18 sample).

4.2.2 Sample preparation for Illumina next-generation sequencing

To quantify sgRNA abundance within the acquired samples, genomic DNA was isolated using the DNeasy Blood and Tissue Kit (Qiagen) according to the manufacturer's instructions. Double elution (first 30 µl, second 20 µl) of the spin columns was performed to increase the yield of the DNA isolation. PCR was performed to amplify the sgRNA locus and add adaptors and barcodes, allowing for Illumina-based sequencing and multiplexing of the samples. The PCR reaction was pipetted, as shown in the table below.

Reagent	**Amount**
Q5-reaction buffer (5x)	10 µl
Forward primer (10 µM) P50X	2.5 µl
Reverse primer (10 µM) P70X	2.5 µl
dNTPs (10mM)	1 µl
GC Enhancer	10 µl
Genomic DNA	3.5 µg
Q5 High Fidelity Polymerase	0.5 µl
Nuclease-free dH_2O	To 50 µl

The PCR amplification was performed using a 1000x coverage and the amount of required genomic DNA was calculated using the following formula:

$$required\ gDNA\ = library\ size\ (number\ of\ sgRNAs)\ x\ coverage\ x\ 10\ pg\ (DNA\ per\ cell)$$

For the screen in this study, 35 µg of genomic DNA were utilized, and this amount was split into 10 reactions with each 3.5µg of gDNA to diversify the amount of mutations gained during the amplification process. The PCR protocol is shown below. For multiplexing of the samples, combinations of differently barcoded PCR primers were used and are indicated for the following samples: NCI-H1437 day 4 (sgRNA_NGS-P501, sgRNA_NGS-P701), NCI-H1437 day 18 (sgRNA_NGS-P502, sgRNA_NGS-P702), HCC-44 day 4 (sgRNA_NGS-P502, sgRNA_NGS-P703), HCC-44 day 18 (sgRNA_NGS-P503, sgRNA_NGS-P704), NCI-H23 day 4 (sgRNA_NGS-P504, sgRNA_NGS-P704), NCI-H23 day 18 (sgRNA_NGS-P504,

sgRNA_NGS-P705). PCR products were purified using the QIAquick PCR purification kit (Qiagen) and pooled for each sample, and the success of the PCR was confirmed by the presence of a 281 bp band, corresponding to the barcoded and amplified sgRNA locus, during agarose gel electrophoresis.

Program step	**Temperature**	**Time**
Initial Denaturation	98°C	2 min
Cycles: 30		
Denaturation	98°C	20 sec
Annealing	60°C	45 sec
Elongation	72°C	45 sec
Final Elongation	72°C	5 min

4.2.3 Illumina MiSeq sequencing

The Illumina MiSeq system was used for sequencing of the samples. To prepare a multiplexed sample for the sequencing, the DNA concentration of each barcoded sample needed to be quantified. The samples were compared to Illumina DNA standards from the KAPA library quantification kit (Kapa Biosystems) through qPCR. To this end, an aliquot of each sample was diluted 1:1000, 1:10,000, and 1: 100,000 and measured together with the DNA standard in technical triplicates. The reaction mix was pipetted as follows: 7.5 µl LightCycler 480 SYBR Green I Master mix, 0.9 µl library qPCR primers (RP7_fw and FP5_rv, 10 mM each), 2 µl template, 4.6 µl dH_2O. The qPCR reaction was performed as described in chapter 4.3.3. The DNA concentration was calculated for each sample, and the samples were diluted and pooled to form 50 µl of a 4nM library. The correct concentration of the library was confirmed by repeating the qPCR against the DNA standard, as described above.

Sequencing of the pooled, multiplexed sample was performed on a MiSeq Illumina machine, using the MiSeq Reagent Kit v2, by R. Öllinger (Department for Internal Medicine II, Klinikum rechts der Isar, München). For this, 4 µl of the sequencing library were mixed with 1 µl of Illumina PhiX Control and 6 pmol of the library were used for sequencing. Sequencing reads were mapped to the library reference file using the web tool of the CRISPRAnalyzeR pipeline (J. Winter et al., 2017)

4.3 Gene expression analysis

4.3.1 RNA extraction from cells

RNA was extracted from frozen cell pellets with RNeasy Mini Kit by Qiagen according to the manufacturer's protocol. The optional step of cell homogenization through QIAshredder spin columns (Qiagen) was performed for all samples. A DNA digest was performed to exclude the binding of PCR primers to genomic DNA instead of cDNA. To this end, the isolated RNA was treated with 0.5 µl DNase I (New England Biolabs) in its respective buffer and incubated at 37°C for 30 min. EDTA was then added to a final concentration of 5 mM, and the samples

were heat-inactivated at 75°C for 10 min. The RNA concentration was measured by spectrophotometry and either directly used for reverse transcription or stored at -80°C.

4.3.2 Reverse transcription of RNA

The SuperScript III Reverse Transcriptase kit (ThermoFisher Scientific) was used for the reverse transcription of RNA into cDNA. To this end, 1 µg of RNA was mixed with 1 µl of random hexamer primers (Roche) in a total volume of 17.5 µl dH_2O and incubated at 70°C for 5 min. After 5 min incubation on ice to cool the mixture down, 6 µl reverse transcriptase buffer (5x), 3 µl DTT, 1 µl 100 mM mixed dNTPs, 0.5 µl RNase Out and 1 µl SuperScript III reverse transcriptase (ThermoFisher Scientific) were added and incubated at 42°C for 60 min. The reaction was stopped through heat-inactivation at 95°C for 5 min, and converted cDNA was directly used for quantitative PCR (qPCR) or stored at -20°C.

4.3.3 Quantitative PCR (qPCR)

Quantitative PCR (qPCR) was used to analyze the expression of a gene of interest. To this end, previously generated cDNA samples were diluted to a final concentration of 4ng/ µl by adding 220 µl H_2O to 30 µl cDNA reaction mix (see chapter 4.3.2). 2 µl of diluted cDNA were added per well of a 96-well plate in technical triplicates on ice. 2 µl water were used as a no-template control. For the master mix, 10 µl LightCycler 480 SYBR Green I Master Mix (Applied Biosystems), 6.8 µl water, and 1.2 µl primer mix (forward and reverse, 10mM each) were mixed per well and per primer pair. The master mix was then pipetted to each well containing cDNA or water, and the plate was sealed with a film (Applied Biosystems) and briefly centrifuged. The LightCycler 480 instrument by Applied Biosystems was used for the qPCR reaction according to manufacturer's instructions, running 40 cycles of amplification. All samples were normalized to the expression of the housekeeping gene ribosomal protein large subunit P0 (*RPLP0*) and further normalized to a control sample using the ΔΔCt method (Livak & Schmittgen, 2001). Sequences of primers are listed in table 3.6.6.

4.4 Cell culture and cell-based assays

4.4.1 Culture of eukaryotic cells

Chapter 3.11 shows a detailed list of all cell lines and their respective growth media used in this study. All cells were grown at 37°C in a humidified incubator with %5 CO_2 content. Cells were cultured on cell culture plates and split every 2-3 days to maintain subconfluency and constant growth. For this, the growth media was discarded, and cells were washed once with PBS. Prewarmed Trypsin/EDTA was added to the cell culture dish, and cells were left to detach at 37°C for 5 min. The trypsin digest was stopped by adding growth media containing serum, and cell debris was removed by centrifuging the cells at 300 rcf for 4 min. The cell pellets were resuspended in fresh growth media and reseeded on new cell culture dishes in a ratio of 1:2-1:8, depending on the growth rate of the cell line.

A defined cell number was seeded into a new dish for specific experiments. To this end, cells were counted in a Neubauer counting chamber using Trypan blue as a discriminator of dead cells.

4.4.2 Freezing and thawing of cells

Cells were frozen in freshly prepared FBS with 10% DMSO (freezing media) for long-term storage. To this end, cells were harvested and centrifuged at 300 rcf for 5 min. Roughly 1 x 10^6 cells were resuspended in 1 ml of freezing media and transferred to a labeled cryo tube. The cryo tubes were frozen at -80°C in a designated freezing container containing isopropanol to allow for slow freezing of cells. Frozen cells were transferred to a liquid nitrogen tank for long-term storage after 24 hours.

To thaw the cells, cryo tubes containing cells were briefly warmed in a 37°C water bath, and the content was transferred to a falcon containing 9 ml of pre-warmed culture media. The cells were then centrifuged at 300 rcf for 5 min to remove the DMSO, and cells were seeded into a cell culture dish containing fresh culture media.

4.4.3 Harvesting cells

For certain experiments, cells were harvested and frozen as non-viable cell pellets. To this end, cells were detached as described above and centrifuged at 300 rcf for 5 min. Cell pellets were then washed twice with PBS and transferred to a 1.5 ml tube. The samples were then centrifuged at maximum speed for 30 sec, the PBS was discarded, and the cell pellets were frozen at -80°C.

4.4.4 DNA transfection by calcium phosphate

The calcium phosphate method was used for the transduction of HEK293T cells. To this end, 4 x 10^6 cells were seeded in a 10 cm cell culture dish in 10 ml culture media. 10 µg DNA were diluted in a total volume of 450 µl H_2O and incubated with 50 µl 2.5 M $CaCl_2$ for 5 min. Then, 500 µl BES solution was added to the mixture dropwise while vortexing. After 20 min of incubation, the mix was added to the cells dropwise and the dish was carefully swirled to mix. The media was replaced with fresh media after 3 hours.

4.4.5 DNA transfection by Lipofectamine 2000

Lipofectamine 2000-based transfection was used for adherent lung adenocarcinoma cell lines, according to the manufacturer's instructions. In short, cells were seeded on the day before transfection to achieve an appropriate density (70-80% confluency). Prior to transfection, culture media was changed to media without Penicillin/Streptomycin (Pen/Strep). DNA and Lipofectamine 2000 were mixed separately with serum-free Opti-MEM and incubated for 5 min. The DNA mixture was then added to the Lipofectamine mixture and carefully mixed by pipetting. A ratio of 1:3 DNA to Lipofectamine was chosen for all experiments. After 20 min of incubation, the transfection mix was added to the cells dropwise, and the dish was swirled carefully to ensure the distribution of the transfection mixture. The transfection media was replaced by fresh media containing Pen/Strep after 3 hours.

4.4.6 siRNA transfection

Selected experiments with the knockdown of DCAF13 were performed in the form of siRNA transfection according to the manufacturer's protocol of the Lipofectamine RNAiMAX reagent

(Thermofisher Scientific). To this end, cells were seeded the day before transfection to achieve an appropriate density (70-80% confluency). Prior to transfection, culture media was changed to media without Pen/Strep. SiRNA and Lipofectamine RNAiMAX were mixed separately with serum-free Opti-MEM and incubated for 5 min. The siRNA mixture was then added to the Lipofectamine mixture and carefully mixed by pipetting. After 15 min of incubation, the mix was added to the cells dropwise, and the dish was swirled carefully to ensure the distribution of the transfection mixture. The transfection media was replaced by fresh media containing Pen/Strep after 3 hours.

4.4.7 Production of lentiviral particles and viral transduction

Lentiviral particles were generated for the transduction of cells and subsequent stable transgene expression. To this end, HEK293T cells were transfected using the calcium phosphate transfection method. The day before transfection, roughly 4x 10^6 HEK293T cells were seeded into a 10cm dish. For the transfection mixture, 15 µg of packaging plasmid (psPAX2), 5 µg of envelope plasmid (pMD2.G), and 20 µg of the designated plasmid containing the transgene were transfected as described in chapter 4.4.4. Media was changed to serum-free OptiMEM 24 hours after transfection and the media containing lentiviral particles was harvested 48 hours after transfection, passed through a 0.45 µm filter and either directly used for infection or aliquoted and frozen at -80°C.

For viral transduction, cells were counted and seeded into an appropriate cell culture dish, and viral supernatant was directly added when the cells were still in suspension. The volume of the viral supernatant was adjusted depending on the number of cells and the desired infection rate. For 100% infection of NCI-H1437 and HCC-44 cells, a 1:3 or 1:2 ratio of 1x10^3 cells to µl viral supernatant was used, respectively. Polybrene was added to the cells at a concentration of 8 µg/µl prior to the addition of the viral supernatant to increase transduction efficiency. Cells were transferred to a fresh culture dish with fresh culture media after 24 hours.

Some constructs that were used in this study contained an antibiotic resistance cassette for the selection of transduced cells. Depending on the antibiotic resistance, the transduced cells were treated at least 48 hours post-transduction with blasticidin (10 µg/ml for HCC-44, 20 µg/ml for NCI-H23 and NCI-H1437) or puromycin (final concentration 0.5 µg/ml). Cells were kept under selection pressure for at least one week, and transgene expression was verified by immunoblotting.

4.4.8 Doxycycline treatment for transgene expression

In this study, a doxycycline-inducible system was used for the expression of shRNAs. HCC-44 and NCI-H1437 cells were lentivirally transduced with the constructs expressing a control shRNA (shCTRL) or shRNAs targeting DCAF13 under the control of a doxycycline-inducible promoter. After the selection of the successfully transduced cells by puromycin, transgene expression was induced by the addition of 1 µg/ml doxycycline. Doxycycline was renewed every 48 hours to ensure prolonged transgene expression.

4.4.9 Treatment with cell death inhibitors

This study used inhibitors of specific cell death pathways to investigate which type of cell death is induced upon DCAF13 depletion. The inhibitors were used in combination with the

doxycycline-inducible shRNA expression system. To ensure that the cell death was completely inhibited, the shRNA expression was induced with doxycycline (see chapter 4.4.8) and the cells were treated with the cell death inhibitor at the same time for the entire length of the experiment. The doxycycline and inhibitors were renewed every 48 hours to ensure continued transgene expression and stability of the cell death inhibition. The following concentrations were used: 20 µM Z-VAD-FMK, 10 µM Necrostatin-1, 1µM Liproxstatin-1.

4.4.10 JC-1 mitochondrial membrane potential detection assay

The JC-1 Mitochondrial Membrane Potential Assay Kit (Cayman Chemicals) was used according to the manufacturer's instructions to determine the mitochondrial membrane potential of cells depleted for DCAF13. To this end, 3000 HCC-44 and 7000 NCI-H1437 cells were seeded in a 96-well plate 24 hours before the measurement. Cells were stained with the diluted assay reagent (1:100 in total) for 30 min at 37°C and subsequently washed once with PBS and measured in PBS immediately. 6 wells were measured per condition, and 4 wells for the background of the JC-1 dye. A plate reader was used for the measurement, using 475 nm excitation and 500-550 nm emission for the JC-1 monomers and 520nm excitation and 580-640 nm emission for the JC-1 aggregates. Blank values for the JC-1 dye were subtracted from every value, and the ratio of JC-1 monomers /JC-1 aggregates was calculated. The highest and lowest value per condition was excluded and the mean ratio in comparison to the control shRNA was calculated.

Cells were also imaged using a confocal microscope. To this end, the cells were additionally incubated with PBS containing 1 µg/ml Hoechst33342 and imaged after 15 min of incubation without washing. Filters for Rhodamine (excitation/emission = 540/570 nm) and FITC (excitation/emission = 485/535nm) were used for the visualization of JC-1 aggregates and JC-1 monomers, respectively.

4.5 Protein biochemistry

4.5.1 Cell lysis

The analysis of the protein content of a cell population required the lysis of the cell and subsequent protein isolation. Harvested cell pellets were resuspended in lysis buffer containing protease and phosphatase inhibitors to prevent degradation or changes in post-translational modifications. A lysis buffer with 150mM NaCl concentration was used for all experiments except the *in-vivo*-ubiquitination assay (Chapter 4.5.7), and it was supplemented with protease inhibitors (PIN, PMSF, TLCK, TPCK), phosphatase inhibitors (Nava, G-2-P), and DTT at previously described concentrations (Chapter 3.13). Cell pellets were resuspended in an appropriate amount of buffer and left to incubate for 20 min on ice. Lysates were cleared for debris by centrifugation at 20,000 rcf at 4°C for 20 min. The protein concentration of the cleared lysates was measured by a modified version of the Lowry assay (Lowry et al., 1951) using the Bio-Rad DC protein assay according to the manufacturer's instructions. Protein lysates were either used in subsequent experiments, such as immunoprecipitation or denatured by the addition of Laemmli buffer and incubation at 95°C for 5 min.

4.5.2 SDS polyacrylamide gel electrophoresis

SDS polyacrylamide gel electrophoresis (SDS-PAGE) is commonly used to separate proteins based on their protein mass and to prepare for subsequent analysis, such as immunoblotting. The addition of SDS allows for the coating of proteins with negatively charged detergent molecules, ensuring that they move through the polyacrylamide gel according to their size and not any inherent charge once an electric field is applied. The polyacrylamide gels were cast using the Mini-PROTEAN® Tetra Electrophoresis system. Each gel consisted of a so-called stacking gel with 3.9% acrylamide and a separating gel containing 6 - 14% acrylamide, depending on the size of the protein of interest. The exact composition of the gels is described in the following table.

Reagent per gel	**Separating Gel [ml]**				**Stacking Gel [ml]**
	6%	9%	10%	12%	
Acrylamide 40% (29:1)	1.5	2.25	2.5	3	1.25
H_2O	To 10 ml				To 5 ml
Separating Buffer	2.5				-
Stacking Buffer	-				1.25
SDS (10%)	0.1				0.1
APS (10%)	0.1				0.1
TEMED	0.004				0.004

After polymerization, the gels were assembled in a chamber filled with running buffer, and 15-25 µg of denatured protein sample were loaded into each pocket of the gel. A protein ladder was included as a size reference and the gels were subjected to electrophoresis at 80-120V until the desired resolution of the protein ladder was achieved. After electrophoresis, the proteins were transferred to a membrane for immunoblot analysis (Chapter 4.5.4), or the gels were incubated in Coomassie (Chapter 4.5.3) to visualize proteins.

4.5.3 Coomassie staining.

Proteins can be visualized within an acrylamide gel using Coomassie staining, which visualizes proteins through interaction with amine groups through van der Waals interactions. For the Coomassie stainig, gels were incubated in the Coomassie staining solution for at least one hour while shaking. Excess dye was removed by repeated washes with Coomassie destaining solution.

4.5.4 Immunoblot analysis

Proteins previously separated by SDS-PAGE were transferred to a polyvinylidene difluoride (PVDF) membrane. To this end, PVDF membranes were shortly activated prior to the transfer of proteins by incubation in methanol for 1 min. The wet transfer was performed with a pre-

chilled transfer buffer by electroblotting at 90V for two hours or 30V overnight. To visualize bound proteins, membranes were shortly stained with a ponceau solution and again destained using washing buffer (WB). Membranes were then blocked in 5% milk (w/v) or 5% bovine serum albumin (BSA) (w/v) for 30 min and subsequently incubated with the primary antibody, diluted in the respective blocking reagent, at 4°C overnight. Dilutions and blocking reagents for the utilized antibodies are indicated in chapter 3.10. The membranes were then washed in WB three times (10 min each) and incubated with the respective horse radish peroxidase (HRP)-coupled secondary antibody at a dilution of 1:10,000. After additional three washing steps, the membranes were incubated with enhanced chemiluminescent (ECL) solution (Pierce ECL Western Blotting Substrate, ThermoFisher Scientific) and visualized using the ChemiDoc Imaging systems (Bio-Rad).

4.5.5 Stripping of membranes

To re-probe PVDF membranes for other antibodies, the previously bound primary and secondary antibodies were removed by incubation with a stripping buffer, containing SDS and β-mercaptoethanol in a process called stripping. The membranes were incubated in the stripping buffer for 30 min at RT and subsequently washed with PBS three times. The membranes were then blocked in 5% milk or 5% BSA and incubated with the new primary antibody.

4.5.6 Immunoprecipitation

Immunoprecipitation (IP) is a method used to purify proteins of interest from a cell lysate using antibodies directly against the protein of interest or a protein tag. The antibodies are commonly attached to agarose beads to enable the sedimentation of bound proteins by centrifugation. In this study, IPs were performed for proteins carrying a FLAG-tag.

In short, cell lysates were generated (Chapter X), using an appropriate lysis buffer, and subjected to a pre-clear, where they were incubated with empty agarose beads for 15 min at 4°C on a rolling wheel to decrease binding of unspecific proteins to the FLAG-M2 agarose beads. Subsequently, the mixture was centrifuged at 200 rcf for 3 min and the supernatant was transferred and incubated with FLAG-M2 agarose beads for 1.5 hours at 4°C. The FLAG-M2 beads were blocked with 1% BSA in PBS for 30 min and washed three times with lysis buffer prior to the incubation with the cell lysate to further reduce unspecific binding. After the incubation of cell lysate and FLAG-M2 beads, the samples were centrifuged, and the beads were washed five times with lysis buffer. Bound proteins were eluted from the beads by the addition of 50 µl of 2x Laemmli buffer and cooking at 95°C for 10 min. The eluted proteins were then subjected to SDS-PAGE and immunoblotting, as described in chapter 4.5.2 and 4.5.4 , respectively.

In this study, 30 µl bead slurry (a 1:1 mixture of dry beads and lysis buffer) of empty agarose beads or FLAG-M2 beads was used per $3x10^6$ HCC-44 or $10x10^6$ HEK293T cells.

4.5.7 *In-vivo*-ubiquitination assay

There are several established methods to determine the ubiquitination status of a protein of interest. In this study, the so-called *in-vivo*-ubiquitination assay was performed. To this end, HEK293T cells were transfected with an siRNA pool targeting the E3 ligase DCAF13 or a non-

targeting control, using RNAiMax (Section 4.4.6). Cells were reseeded the next day and transfected with plasmids encoding 0.3 µg HA-tagged ubiquitin and 3 µg FLAG-tagged ubiquitination substrate candidate and respective controls the day after reseeding, using Lipofectamine 2000 (Section 4.4.5). 24 hours after transfection, cells were treated with 10 µM proteasome inhibitor MG132 for 3 hours to allow accumulation of ubiquitinated proteins. The cells were harvested and directly lysed in 100 µl ice-cold lysis buffer containing 250 mM NaCl and protease and phosphatase inhibitors. Lysates were passed through a syringe to allow extraction of nuclear proteins and were incubated on ice for 20 min before sedimentation of cell debris by centrifugation. Equal amounts of protein were denatured for every condition by adding 0.1 % NP-40, 5 mM EDTA, 1% SDS (v/v), and incubating at 95°C for 10 min. Samples were cooled down for two min at RT and the denaturation was quenched through the addition of 790 µl 250mM NaCl lysis buffer supplemented with 1% Triton-X-100. FLAG-IP was performed subsequently, as described in chapter 4.5.6.

4.6 Mass spectrometry

4.6.1 Interactome analysis

In this study, DCAF13-interacting proteins were identified through FLAG-IP and subsequent mass spectrometric analysis of co-purified proteins. To this end, HCC-44 cells stably expressing SF-DCAF13 or SF-EV were expanded, and $50x10^6$ cells were harvested per condition. Additionally, ten 15cm dishes of HEK293T cells were transiently transfected with plasmids encoding SF-DCAF13 or SF-EV, and roughly $200x10^6$ cells were harvested the next day. All samples were generated in triplicates and pellets were frozen at -80°C until the FLAG purification was performed for all technical replicates at the same time. FLAG-IP was performed as described in chapter 4.5.6 with minor adjustments. $50x10^6$ HCC-44 cells were lysed in 10 ml lysis buffer and IP was performed with 100 µl FLAG-M2 bead slurry. $200x10^6$ HEK293T cells were lysed in 10 ml lysis buffer and IP was performed with 200 µl FLAG-M2 bead slurry. Moreover, bound proteins were eluted from the beads by the addition of 3xFLAG peptide instead of denaturation. To this end, the washed beads after FLAG-IP were washed once with TBS. Proteins were eluted by adding 5x dry bead volume of 200 µg/ml 3xFLAG peptide in TBS and incubation for 30 min at 4°C on an overhead rotator. The single elution step was followed by a TBS wash of the beads with the same volume to increase the yield of eluted proteins.

Eluted proteins were precipitated by the addition of 20% (v/v) TCA and incubation at 4°C overnight. Proteins were pelleted by centrifugation at 20,000 rcf and 4°C for 30 min and subsequent washing steps with 100% acetone. Washed protein pellets were dried in a vacuum concentrator. The samples were then reconstituted in LDS buffer (NuPAGE), reduced with DTT, and alkylated with chloroacetamide (CAA). 100% and 50% of the HCC-44 and HEK293T purification, respectively, were loaded onto a 4-12% BIS-TRIS NuPAGE gel and stained with Coomassie (Chapter 4.5.3) before handing over to Dr. P. Giansanti of the BayBioMS@MRI core facility at TUM.

Further processing by the collaboration partner started with in-gel trypsin digestion of the proteins. Digested peptides were extracted and dried. Dried peptides were reconstituted in 0.1% FA and subjected to MS analysis using a Dionex Ultimate 3000 UHPLC+ system coupled to an Orbitrap Eclipse mass spectrometer (ThermoFisher Scientific). Peptides were delivered

to a trap column (75 µm × 2 cm, packed in-house with 5 µm Reprosil C18 resin; Dr. Maisch) and washed using 0.1% FA at a flow rate of 5 µL/min for 10 min. Subsequently, peptides were transferred to an analytical column (75 µm × 45 cm, packed in-house with 3 µm Reprosil C18 resin, Dr. Maisch) applying a flow rate of 500 nL/min. Peptides were chromatographically separated using a 5 min linear gradient from 4% to 24% solvent B (0.1% FA, 5% DMSO in ACN) in solvent A (0.1% FA in 5% DMSO) applying a flow rate gradient from 500 to 300 nL/min. An additional 3 min linear gradient from 24% to 36% of solvent B was applied, before a 2 min wash and 2 min re-equilibration step at 80% and 4% solvent B, respectively. The mass spectrometer was operated in data-dependent mode, automatically switching between MS and MS/MS. Full-scan MS spectra (from m/z 360 to 1300) were acquired in the Orbitrap with a resolution of 60,000 at m/z 200, using a normalized automatic gain control (AGC) target of 100% and maximum injection time (maxIT) of 50 ms. The most intense ions from the survey scan were selected for HCD fragmentation with normalized collision energy set to 30% within a cycle time of 0.9 s. The isolation window was set to 1.3 Th, and MS/MS spectra were acquired in the Orbitrap with a resolution of 30,000 at m/z 200, using an AGC target of 100%. Dynamic exclusion was set to 25 s.

Peptide and protein identification was performed using MaxQuant (version 2.0.3.0) with its built-in search engine Andromeda (Cox and Mann, 2008). Spectra were searched against a human UniProt database, (UP000005640 – 79,759 sequences). Enzyme specificity was set to Trypsin/P and the search included cysteine carbamidomethylation as a fixed modification, protein N-term acetylation, and oxidation of methionine as variable modifications. Up to two missed cleavage sites were allowed. Precursor tolerance was set to 4.5 ppm (after MS1 feature re-calibration), and fragment ion tolerance to 20 ppm. The match-between-runs feature was enabled. Before further data analysis using the Perseus software suite (version 2.0.7.0), hits to the reverse and contaminant databases and proteins with less than two unique peptides were removed.

For data analysis, only proteins with reliable identification were quantified. For statistical analysis (FDR<5%), data were filtered for at least 2 values in at least one of the 2 conditions and missing data were imputed from a random distribution. Significance was calculated by Welsh's t-test.

4.6.2 DiGLY proteomics

DiGLY proteomics was employed to identify proteins less ubiquitinated upon DCAF13 depletion. To this end, HCC-44 and NCI-H1437 cells were lentivirally transduced to express shRNAs targeting DCAF13 or a non-targeting shRNA to reach a 100% transduction rate. The samples were generated in three biological replicates. Cells were harvested after 48 hours, washed twice with PBS, and cell pellets were stored at -80°C. The cell pellets were lysed in SDS lysis buffer and incubated at 95°C for 5 min. The protein concentration was measured using the Pierce BCA Protein Assay Kit (ThermoFisher Scientific) according to the manufacturer’s instructions.

For the protein digestion, 2 µg of protein per sample were mixed with 100 µl SpeedBeads magnetic carboxylate-modified particles (Cytiva) (1:1 mixture of A and B beads), and 100% EtOH was added to a final concentration of 70% to precipitate the proteins on the beads. The beads were then washed extensively with 80% EtOH and once with acetonitrile before reduction with 10mM TCEP and alkylation with 50mM chloracetamide (CAA) for 45 min

at 37°C. 40 µg trypsin was directly added and incubated at 37°C for 16 hours. The digestion was stopped by acidifying the samples with formic acid (FA) to a final concentration of 0.5%.

The peptides were desalted using Sep-Pak tC18 cartridges (Waters Corp). The cartridges were wet with ACN and Solvent B (0.1% FA, 50% ACN in ddH_2O) and equilibrated twice with Solvent A (0.1% FA in ddH_2O) before loading the acidified peptides. The bound peptides were washed twice with Solvent A and eluted twice with Solvent B. The peptide concentration was determined by Nanodrop measurement, and 50 µg peptides per sample were aliquoted for the analysis of the whole proteome. These samples were frozen at -80°C and dried in a speed vac vacuum concentrator for subsequent TMT labeling. 450 µg peptide of each sample was frozen at -80°C and dried in a speed vac vacuum concentrator to continue for the diGLY enrichment.

For the diGLY enrichment, the beads from the PTM Scan Ubiquitin Remnant Motif (K - ε - GG) kit (Cell Signaling Technology) were washed with borax buffer and cross-linked using 20mM dimethyl pimelidimate (DMP) in borax buffer. Beads were always handled on ice, and all centrifugation steps for the beads were carried out at 2000 rcf and 4°C. The beads were then washed with diGLY blocking buffer and incubated in that buffer overnight at 4°C in an overhead rotator. The beads were then resuspended in Immuno-Affinity Purification (IAP) buffer, and one vial of beads was distributed into nine Eppendorf tubes for the diGLY IP. The dried, desalted peptides were resuspended in IAP buffer and transferred to the Eppendorf tubes containing the previously prepared beads. The mixture was incubated for one hour at 4°C in an overhead rotator. The beads were washed three times with ice-cold PBS and then resuspended in 50 µl 100 mM HEPES (pH= 8.5) to prepare for the TMT labeling.

Each sample was labeled with a different TMT channel, and the preparation of the tube containing the TMT reagent and the labeling of the respective sample was performed for one sample at a time to reduce the chance of hydrolyzation of the TMT reagent and therefore decreased labeling efficiency. To this end, 200 µg TMT reagent was resuspended in 5 µl anhydrous ACN, quickly vortexed, and 2.5 µl (100 µg TMT reagent) were added to the resuspended beads and incubated while shaking at 25°C for 10 min. After incubation, the labeling was quenched by adding 2 µl 5% hydroxylamine (v/v) and another incubation of 5 min under the same conditions. The beads were then washed with PBS and resuspended in 120 µl PBS and an aliquot (5 µl) was stored at -20°C to possibly evaluate labeling efficiency. The beads of all samples of one cell line (9 samples per cell line: 3x shCTRL, 3x shDCAF13_2, 3x shDCAF13_3) were then pooled, washed twice with PBS, and peptides were then eluted with the diGLY elution buffer (twice, 100 µl per elution) by incubating while shaking at RT for 5 min.

The eluted peptides were desalted using self-packed StageTips (three disks of Empore C18, ∅ 1.5 mm; 3M). To this end, the peptides were first acidified with FA to 1% (v/v). The StageTips were then wet with ACN and StageTip Solvent B and equilibrated with StageTip Solvent A by centrifugation of the StageTip at 500 rcf. The acidified peptides were then loaded onto the StageTip, and the flow-through was reapplied to the StageTip to increase the yield of the desalting. The peptides were washed with StageTip Solvent A and eluted with 40 µl of StageTip Solvent B. The sample was then frozen at -80°C and dried in a speed vac vacuum concentrator.

The previously dried peptides for the whole proteome measurement were prepared for TMT labeling by reconstitution in 10 µl 100 mM HEPES (pH= 8.5). TMT labeling was performed as described above with minor adjustments: Only 50 µg of TMT reagent was used for these samples, and incubation with the TMT reagent was increased to 1 hour. The labeled peptides

were pooled for each cell line (9 samples per cell line: 3x shCTRL, 3x shDCAF13_2, 3x shDCAF13_3) and desalted using Sep-Pak tC18 cartridges, as described above. An aliquot of these samples was fractionated by the collaboration partner Dr. Y. Chang (Chair of Proteomics and Bioanalytics at TUM) to increase the yield of identified proteins. To this end, 50 µg of labeled, pooled peptides were loaded onto StageTips and eluted with increasing amounts of ACN (5%, 7.5%, 10%, 12.5%. 15%, 17.5%, 50%). The 5% ACN and 50% ACN fractions were pooled, and the 17.5% ACN fraction was pooled with the first flow-through of the sample loading, resulting in a total of 6 fractions. The fractions were frozen at -80°C and dried with a speed vac vacuum concentrator.

The mass spectrometric measurement and analysis of the data were performed by the collaboration partner Dr. Y Chang. The diGLY-enriched, pooled sample for each cell line was reconstituted in 0.1% FA and measured with a 100 min linear gradient MS3 acquisition on a Fusion Lumos Tribrid mass spectrometer (ThermoFisher Scientific). The fractionated whole protein samples were reconstituted in 0.1% FA, and each fraction was measured with a 60 min linear gradient MS3 acquisition on a Fusion Lumos Tribrid mass spectrometer (ThermoFisher Scientific). Peptide and protein identification and quantification were performed using MaxQuant by searching the MS2 spectra against the human reference proteome supplemented with common contaminants. Further analysis was performed with Perseus. For the diGLY-enriched samples and the whole proteome samples, each TMT channel was additionally normalized to the median intensity of that channel to account for differences in sample handling and sample loss.

4.7 Immunofluorescence microscopy

Immunofluorescence (IF) microscopy uses fluorochrome-coupled antibodies to visualize proteins in their subcellular compartments. To this end, cells were seeded in detachable 8-well chamber slides for microscopy (Sarstedt) and left in culture for the desired amount of time but at least 24 hours. The cells were washed once with PBS and fixed with 4% paraformaldehyde (PFA) in PBS for 10 min at RT. Cells were washed once with PBS and then permeabilized with the IF permeabilization buffer for 10 min at RT. After another washing step with PBS, unspecific antibody binding was blocked with the IF-blocking buffer for 30 min at RT. The slides were then incubated with the primary antibody, diluted in IF staining buffer, overnight at 4°C in a wet chamber. The next day, the slides were washed three times with PBS and incubated with the respective fluorochrome-coupled secondary antibody for one hour at RT. The fluorochrome-coupled phalloidin probe was used parallel to the secondary antibody staining to visualize the actin cytoskeleton. After incubation, cells were washed thrice with PBS, and the nuclei were counterstained with 1 µg/ml Hoechst33342. After staining, the chamber was removed, and the slides were washed once with ddH_2O. Mounting medium was added to the slide, covered by a glass coverslip, and left to cure for 24 hours at RT before imaging with a confocal microscope.

4.8 Flow cytometry

4.8.1 Analysis of dsRed and GFP-positive cells

Transduction efficiency for cells expressing the transgenes GFP or dsRed was measured by flow cytometry. To this end, cells were trypsinized, washed twice with PBS, and subsequently analyzed on an Accuri C6 flow cytometer by BD Biosciences. The GFP and dsRed expression were detected in the FL-1 (FITC) and FL-2 (PE) channels, respectively. Data were further analyzed using the FlowJo (version 10.9.0) software (BD Biosciences).

4.8.2 Analysis of cell death via Annexin V and Live/Dead-dye exclusion

To determine the amount of apoptotic or dead cells within a given sample, Annexin V and live/dead was performed. Annexin V specifically binds to phosphatidylserine, which is translocated from the intracellular side of the plasma membrane to the extracellular side during apoptosis. The live/dead stain (ThermoFisher Scientific) binds to amines on the surface of cells. Once the integrity of the cell membrane is lost during cell death, the dye is able to enter the cells and bind to amines intracellularly, thereby increasing the fluorescence intensity compared to cells with an intact plasma membrane. Consequently, cells positive for Annexin V but negative for the Live/Dead staining are undergoing apoptosis, and double-negative cells are alive. Cells stained by the exclusion dye and Annexin V are classified as dead. For multiplexing, the live/dead dye was coupled with the APC fluorophore, and the Annexin V probe was connected to the FITC fluorophore (BD Pharmingen).

For the experiment, cells were trypsinized and counted. The cells were washed three times with PBS and resuspended in the live/dead stain at a dilution of 1:1000 in PBS and stained for 15 min on ice. The samples were then washed twice with PBS and once with Annexin V binding buffer before resuspending in 100 µl Annexin V binding buffer supplemented with 5 µl FITC Annexin V. The cells were stained for 20 min at RT in the dark and subsequently washed once with Annexin V binding buffer. Flow cytometric analysis was performed in the Annexin V binding buffer. Data was analyzed using the FlowJo (version 10.9.0) software (BD Biosciences).

4.8.3 Cell cycle analysis

The cell cycle phase of a given cell can be determined by DNA content analysis. In this study, the fluorescent dye propidium iodide (PI) was used to stain DNA before analysis by flow cytometry. To this end, cells were fixed in 70% ice-cold ethanol and subsequently stained with the PI/RNase staining buffer (BD Pharmingen) according to the manufacturer's instructions. Cells were analyzed on the BD C6 Accuri flow cytometer with the FL-2 channel. Cell cycle gates were annotated manually in relation to each other using the FlowJo (version 10.9.0) software (BD Biosciences): G1-phase $\approx$ 2n, S-phase $\geq$ 2n and $\leq$ 4n, and G2/M-phase $\approx$ 4n

4.8.4 Fluorescence-activated cell sorting

Fluorescence-activated cell sorting (FACS) describes the process of sorting cells according to their flow cytometric properties, such as size or fluorescence. In this study, cells were sorted during the CRISPR/Cas9 screen. To this end, cells were transfected with the mCherry

expressing pooled lentiviral sgRNA library and sorted on day four post-transduction. FACS was performed on a FACS Aria Fusion cell sorter in a Cell Analysis Core Facility (TranslaTUM, Klinkum rechts der Isar, München). Before sorting, cells were trypsinized, washed once with PBS, and resuspended in FACS buffer (PBS with 2% FBS) at a concentration of $5x10^6$ cells/ml. The cell suspension was filtered through a 30 µm cell strainer and stored on ice until sorting. Sorted cells were resuspended in pre-warmed growth medium.

4.9 RNA sequencing

RNA sequencing was employed to identify transcriptomic changes upon DCAF13 depletion. To this end, HCC-44 and NCI-H1437 cells were lentivirally transduced to express shRNAs targeting DCAF13 or a non-targeting shRNA to reach a 100% transduction rate. The samples were generated in three biological replicates. Cells were harvested prior to transduction, 48 hours post-transduction, and 96 hours post-transduction, washed twice with PBS, and cell pellets were stored at -80°C. RNA was isolated from all samples at the same time, using the RNeasy Mini Kit (Qiagen) according to the manufacturer's instructions. DNA digest was performed as described in the manual, using the RNase-Free DNase Set (Qiagen). RNA quality was assessed by loading 1 µg of RNA on an agarose gel and confirming the presence of a clear 750 bp and 1500 bp band corresponding to the 18S RNA and 28S RNA, respectively.

The RNA was handed over to the collaboration partner R. Öllinger (Department of Medicin II, Klinikum rechts der Isar, TUM). Library preparation for bulk-sequencing of poly(A)-RNA was done as described previously (Parekh et al., 2016). Briefly, barcoded cDNA of each sample was generated with a Maxima RT polymerase (ThermoFisher Scientific) using oligo-dT primer containing barcodes, unique molecular identifiers (UMIs), and an adaptor. The 5' ends of the cDNAs were extended by a template switch oligo (TSO), and full-length cDNA was amplified with primers binding to the TSO-site and the adaptor. NEB UltraII FS kit was used to fragment cDNA. After end repair and A-tailing, a TruSeq adapter was ligated, and 3'-end-fragments were finally amplified using primers with Illumina P5 and P7 overhangs. In comparison with Parekh *et al*(Parekh et al., 2016), the P5 and P7 sites were exchanged to allow sequencing of the cDNA in read1 and barcodes and UMIs in read2 to achieve a better cluster recognition. The library was sequenced on a NextSeq 500 (Illumina) with 65 cycles for the cDNA in read1 and 18 cycles for the barcodes and UMIs in read2. Gencode gene annotations M25 and the human reference genome GRCh38 were derived from the Gencode homepage (EMBL-EBI). Drop-Seq tools v1.12 was used for mapping raw sequencing data to the reference genome (Macosko et al., 2015).

The mapped sequencing data was handed over to Dr. P. Auf der Maur for analysis of transcriptomic changes. In short, differential gene expression analysis was achieved using the edgeR framework (Y. Chen et al., 2016). Gene set enrichments were performed using CAMERA (D. Wu & Smyth, 2012). Curated gene sets (Hallmark, C2, C5) from the Molecular Signatures Database (MSigDB) were used. The analysis was performed for each on-target shRNA, each time-point, and each cell line separately.

4.10 Statistical analysis

All quantified experiments were performed in triplicates, meaning three independent biological replicates, except if indicated otherwise in the figure legend. The non-quantified immunoblot data generally shows results representative of at least two independent experiments. Statistical analyses of the results were performed with the GraphPad Prism software. Depending on the type of data, significance was calculated using the Welsh's t-test, unless indicated otherwise. The error bars shown in the figures represent the mean ± standard deviation (S.D.). The p-values are denoted in the figure legends where a statistically significant difference was found: *, $p < 0.05$; **, $p < 0.01$; ***, $p < 0.001$; ****, $p < 0.0001$.

Statistics for the transcriptomic analysis were calculated using the edgeR framework (Y. Chen et al., 2016) and the glmQLFTest function.

5 Results

5.1 A CRISPR/Cas9-screen identifies DCAF13 as a novel dependency in LuAD

5.1.1 Setup and optimization of the CRISPR/Cas9 screen

In an effort to identify novel vulnerabilities in LuAD, we optimized and performed a CRISPR/Cas9-based dropout screen with a targeted library. The library, consisting of roughly 3200 sgRNAs targeting more than 750 genes of the ubiquitin system, was previously published and was a kind gift from Mitch Weiss from the Children's Hospital in Memphis (Xu et al., 2021). The conceptualization of the screen was based on previous work from the Bassermann lab (Paulmann et al., 2022) and is depicted in figure 7.

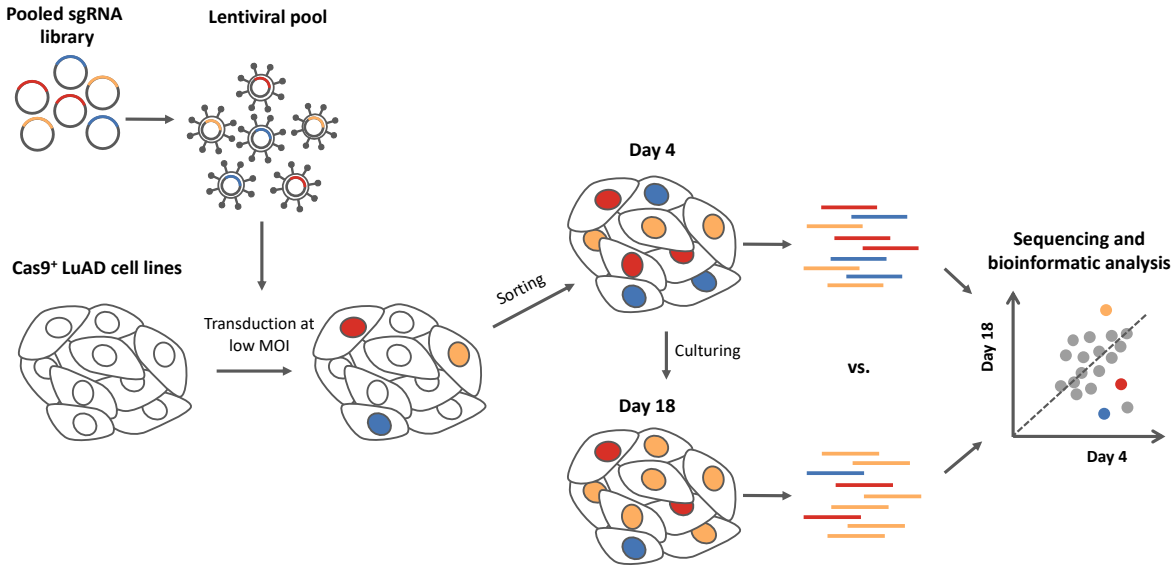

Figure 7: Schematic setup of the CRISPR/Cas9-based dropout screen
A pooled sgRNA library, targeting more than 750 genes of the ubiquitin system, was lentivirally transduced into Cas9-expressing LuAD cells at a low multiplicity of infection (MOI). Transduced cells were sorted, and samples were taken on day four and after 14 days of culturing (day 18). Genomic DNA was isolated, and the sgRNA locus was amplified and sequenced. The composition of the sgRNA pool was compared between day four and day 18 to determine sgRNAs that dropped out of the population and thus targeted genes essential for LuAD cell survival.

In short, the pooled sgRNA library was packaged into lentiviral particles and transduced into Cas9-positive LuAD cell lines at a low multiplicity of infection (MOI) to minimize double-transduction events. Transduced cells, expressing the selection marker mCherry, were sorted on day four post-transduction and maintained in culture for 14 days. Samples of the cell population were taken on day four and day 18, and the sgRNA locus was isolated, amplified from the genomic DNA, and subsequently sequenced. The library composition was compared between the samples to identify sgRNAs that were depleted or enriched over time, hence targeting dependencies or suppressors of LuAD maintenance, respectively.

As described in chapter 2.1.2, LuAD tumors are characterized by significant heterogeneity in cancer driver mutations, of which *EGFR* mutations and *ALK* translocations can be targeted by clinically approved drugs. Hence, four cell lines with an *EGFR* and *ALK* wildtype genotype were chosen for the initial screen optimization, namely NCI-H1437, NCI-H1792, NCI-H23, and HCC-44.

The cell lines were lentivirally transduced with a Cas9-expression construct, and the expression was confirmed by immunoblot analysis (Figure 8a). The growth of the parental and transgenic cell lines was compared to exclude an effect of the Cas9-transgene genomic insertion and expression on cell proliferation. The transgene introduction did not alter the observed cell number in any Cas9-expressing cell line (Figure 8b).

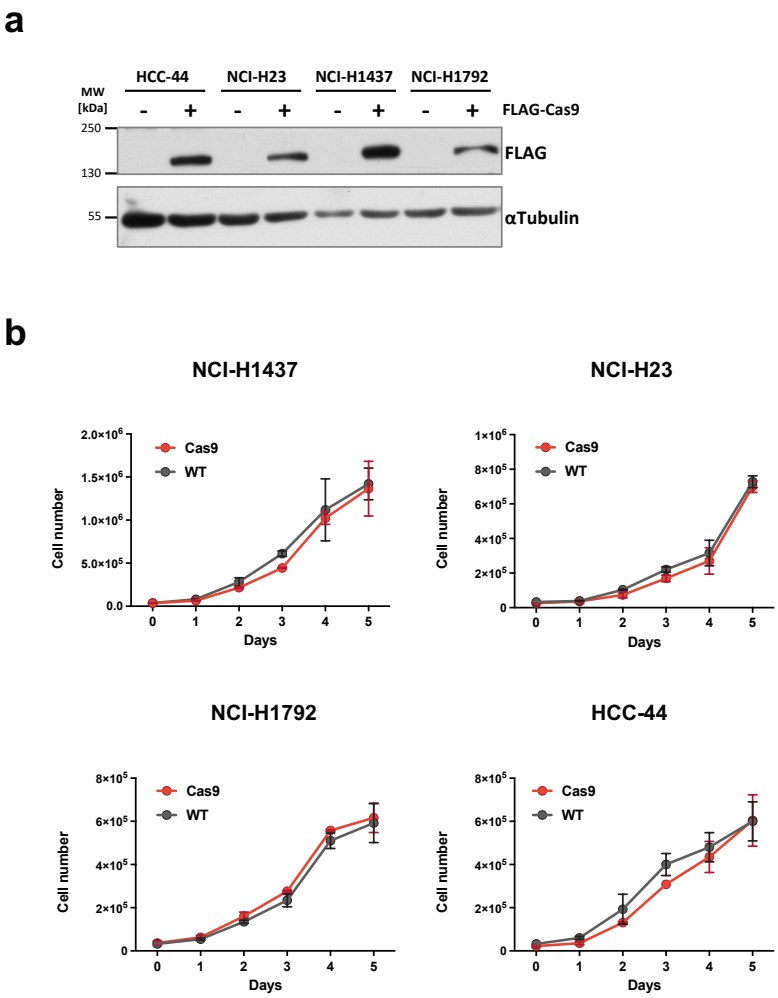

Figure 8: Generation of stable Cas9-expressing cell lines
Indicated LuAD cell lines were lentivirally transduced to express the Cas9 protein. (**a**) Cas9 expression was validated by immunoblot analysis. (**b**) The growth kinetics of the Cas9-expressing cells and their wildtype (WT) parental cell lines were compared by cell counting at indicated time points.

Further, the functionality of the Cas9 protein was evaluated through competition of non-transduced cells and cells transduced with non-targeting sgRNAs (sgNT) or sgRNAs targeting the essential gene RNA polymerase II (*POLR2*). The proportion of transduced cells (GFP positive) to non-transduced control cells was observed over time by flow cytometry. As shown

in figure 9, the relative amount of cells transduced with non-targeting sgRNAs remained roughly the same over 13 days of observation, whereas the cells receiving sgRNAs targeting *POLR2* were outcompeted by the non-transduced cells and dropped out of the mixed population. This indicates that the Cas9 protein is active and can induce a knockout of the *POLR2* gene with the provided sgRNAs, leading to the depletion of these cells from the cell pool.

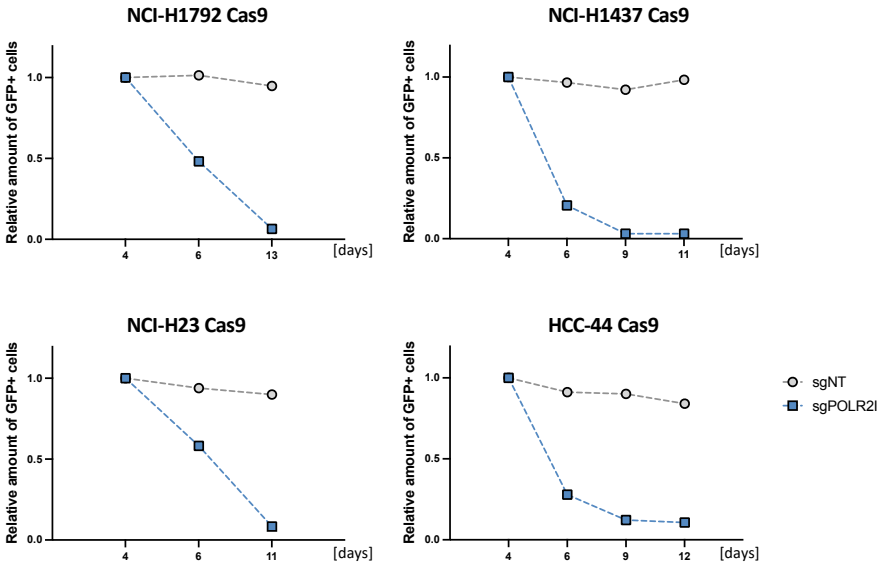

Figure 9: Evaluation of Cas9 activity in Cas9-expressing LuAD cells
Cas9-expressing LuAD cells were lentivirally transduced with either a non-targeting sgRNAs (sgNT) or an sgRNA targeting the essential gene RNA polymerase II (sgPOLR2I) to obtain a transduction rate of roughly 50%. Transduced cells also expressed the transgene GFP. The amount of GFP-positive cells was observed at the indicated time points by flow cytometry. Results are shown for each sgRNA in relation to day four.

As previously mentioned, the Cas9-positive cells were transduced with the lentiviral sgRNA library pool at a low MOI to reduce the occurrence of double transduction events. The MOI for the CRISPR-Screen was optimized by prior investigation of double transduction events. For that purpose, double transduction was evaluated by transduction of a GFP-expressing and an mCherry-expressing lentiviral vector in equal amounts. The single and double positive populations were measured by flow cytometry (Figure 10a), and the double positive population was calculated as a fraction of total transduced cells (Figure 10b). A non-linear increase of double-transduced cells with increasing amounts of lentivirus could be observed for all cell lines. Previous CRISPR-Screens in the Bassermann lab aimed for a double transduction rate of less than 10% of total transduction events. This was achieved in almost all cell lines with a total transduction rate of 15-20%, corresponding to an MOI of 0.15-0.2. While this method underestimates the amount of double infected cells, as it will not measure cells with double mCherry or double GFP expression, it is still a useful approximation. Accordingly, the sgRNA library virus was titrated and scaled up to achieve a transduction rate of 15-20% in the final setup of the screen.

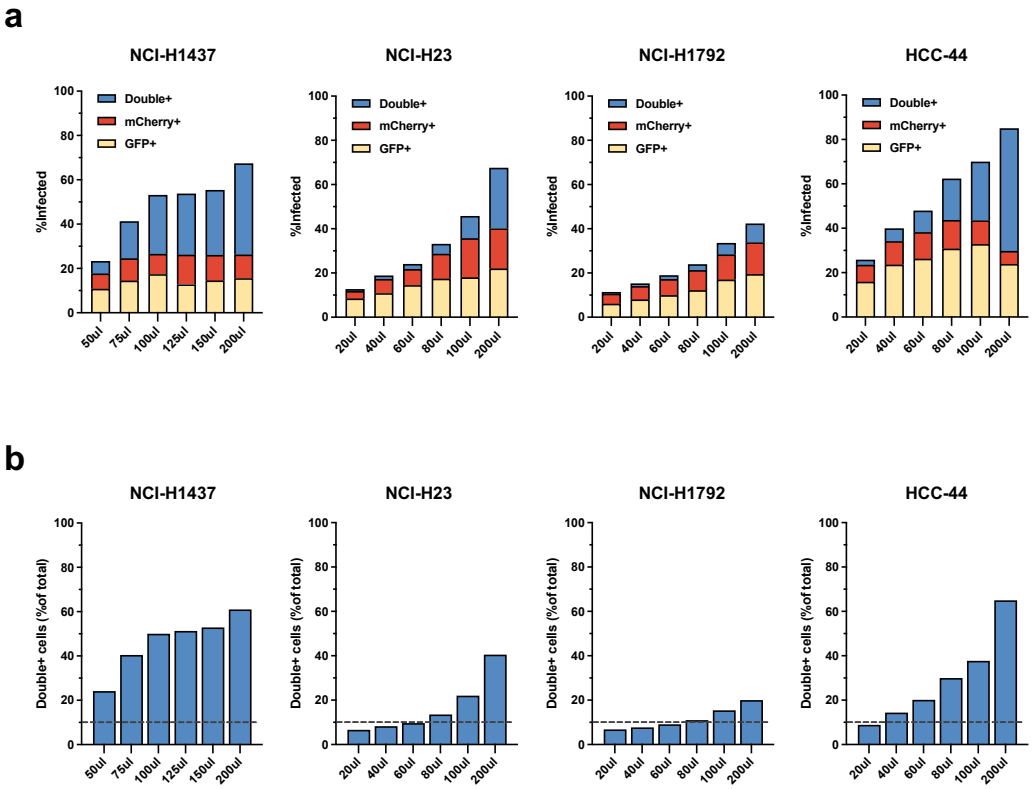

Figure 10: Optimization of transduction rate and analysis of double transduction events
Indicated cell lines were transduced with indicated equal amounts of mCherry or GFP expressing lentivirus and analyzed by flow cytometry. (**a**) The amount of single-positive (mCherry+, GFP+) or double-positive (Double+) cells for each amount of virus and each cell line are indicated. (**b**) Double transduced cells are depicted as a percentage of all transduced cells.

The CRISPR screen was ultimately performed as shown in figure 7. A detailed description of the method can be found in chapter 4.2. Of note, the cell line NCI-H1792 was excluded from the screen, as a trial of the sorting process showed that a single cell suspension of the cell line frequently formed clumps and thus was not suitable for sorting.

5.1.2 Results of the CRISPR/Cas9 screen

5.1.2.1 Scoring and evaluation of the CRISPR/Cas9 screen

After performing the screen in three cell lines (NCI-H1437, NCI-H23, HCC-44), genomic DNA was isolated from all samples, and the sgRNA locus was amplified by PCR and sequenced. The sequencing reads were mapped to the library sequence file, and the counts of each sgRNA were normalized as counts per million reads (CPM). The value of 1 was added as a pseudocount for logarithmic computation (CPM+1). Figure 11 shows the CPM+1 values of each individual sgRNA for day four and day 18. Dots above or below the dashed line indicate an enrichment or depletion of sgRNAs after 14 days, respectively. Similarly, the corresponding graphs in panel b show the log2 transformed fold changes of each individual sgRNA. The changes in sgRNA abundance vary between the cell lines, with cell line NCI-H1437 showing the strongest spreading and HCC-44 showing a more modest spreading of sgRNAs. The positive controls, in form of essential genes, and negative controls, in form of non-targeting

sgRNAs, behave as expected in all cell lines by showing a substantial depletion and not changing abundance, respectively. This indicates a satisfying technical quality of the screen in all cell lines. Moreover, well-described oncogenes and therapeutic targets of LuAD, such as E3 ubiquitin-protein ligase UHRF1 (*UHRF1*) (Sidhu & Capalash, 2017), are classified as vulnerabilities in all cell lines (data not shown) emphasizing the experiment's validity.

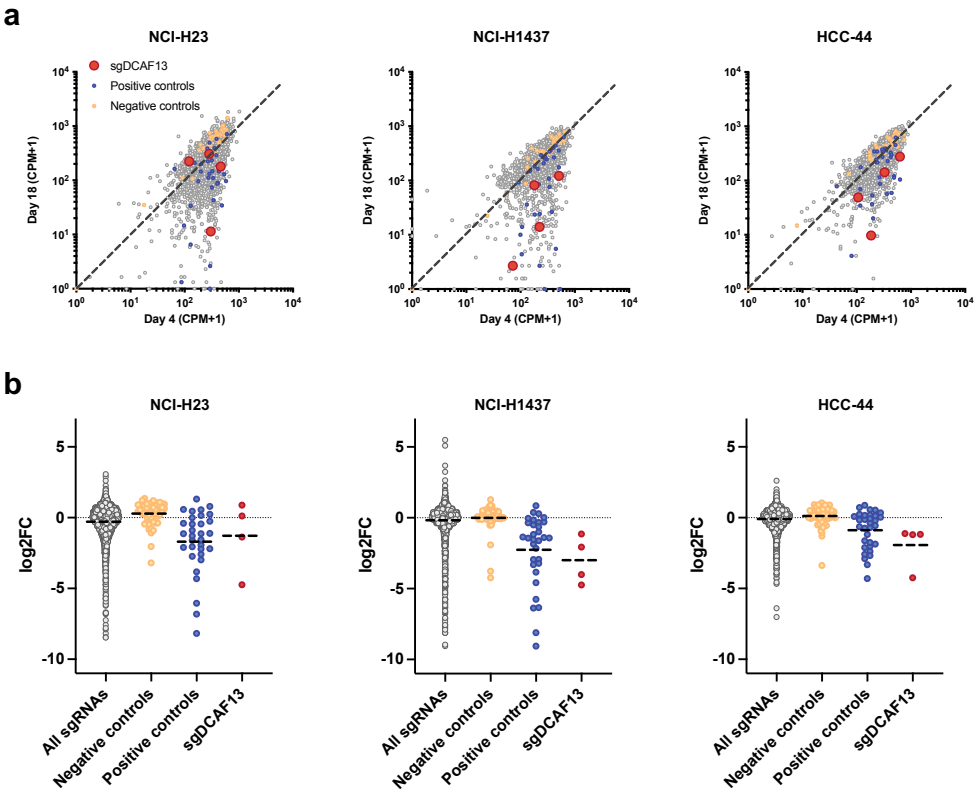

Figure 11: Visualization of the results of the CRISPR/Cas9-dropout screen in LuAD cell lines
Indicated cell lines were transduced with a pooled sgRNA library, as described previously. (**a**) comparison of sgRNA abundance between day four and day 18. (**b**) Fold change of sgRNA abundance was calculated from day four to day 18. Negative controls, in the form of non-targeting sgRNAs, are shown in orange. Positive controls, in the form of the essential genes *COPS5, COPS6, EIF3F, EIF3H, NUP43, TCEB1, TCEB3C, TCEB3*, are indicated in blue. sgRNAs targeting *DCAF13* are indicated in red.

5.1.2.2 Selection of DCAF13 as a candidate

To identify the most promising and clinically relevant novel vulnerability, the screen data was cross-validated with the transcriptome data of the PanCancer Atlas dataset on LuAD from The Cancer Genome Atlas (TCGA) (Ding et al., 2018). For that purpose, we calculated the relative expression, comparing tumor and normal tissue, of all genes present in the ubiquitin-specific CRISPR library (Figure 12a). Interestingly, the poorly described E3 ubiquitin ligase *DCAF13* (highlighted in red) was the most significantly upregulated gene in the TCGA LuAD dataset. This is particularly apparent when comparing patients with matched tumors and normal tissue (Figure 12c). Additionally, *DCAF13* scored highly in all cell lines in the CRISPR screen (Figure 11a and b). Hence, *DCAF13* presented an attractive new target, and we decided to further investigate its involvement in LuAD carcinogenesis.

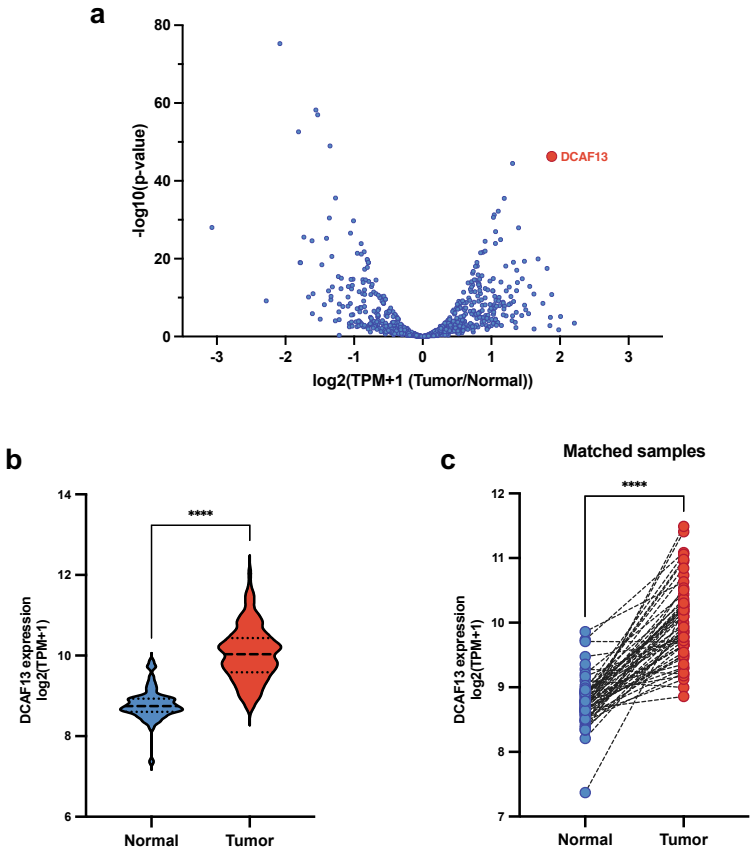

Figure 12: DCAF13 expression in tumor versus normal tissue of LuaD patients

The PanCancer Atlas dataset on LuAD from The Cancer Genome Atlas (TCGA) was analyzed for the expression of ubiquitin-related genes from the CRISPR library in tumor versus normal tissue (**a**). (**b**) Expression of *DCAF13* in normal and tumor tissue of LuAD patients. (**c**) *DCAF13* expression in patients with matched tumor and normal tissue. Matched samples are connected by dashed lines. Statistical significance was calculated by Welsh's t-test. **** : $p < 0.0001$, *** : $p < 0.001$, ** : $p < 0.01$, * : $p < 0.05$

5.1.3 High DCAF13 expression correlates with aggressiveness in patients with LuAD

High *DCAF13* expression correlates with worse overall survival (Figure 13a) and progression-free survival (Figure 13b) in patients with LuAD. Moreover, patients with high *DCAF13* expression exhibit a significantly higher Winter hypoxia score (Figure 13c), a marker for tumor aggressiveness (S. C. Winter et al., 2007). While these patients show a significantly higher mutation count (Figure 13d), a decrease in mutation frequency in the most common oncogenic driver alterations can be observed (Figure 13e). Patients with high *DCAF13* expression show fewer mutations in *EGFR* and *BRAF* and fewer *ROS1* and *ALK* fusion events, making them less eligible for targeted therapy. Lastly, patients with high *DCAF13* expression show a lower frequency of low-grade (Stage I, Stage IA) and a higher frequency of high grade (Stage IIIA, Stage IIIB, Stage IV) tumor stages than those with low *DCAF13* expression (Figure 13f). These results indicate that high *DCAF13* expression correlates with more aggressive LuAD tumors, making *DCAF13* an encouraging candidate for risk prediction or targeted therapy development.

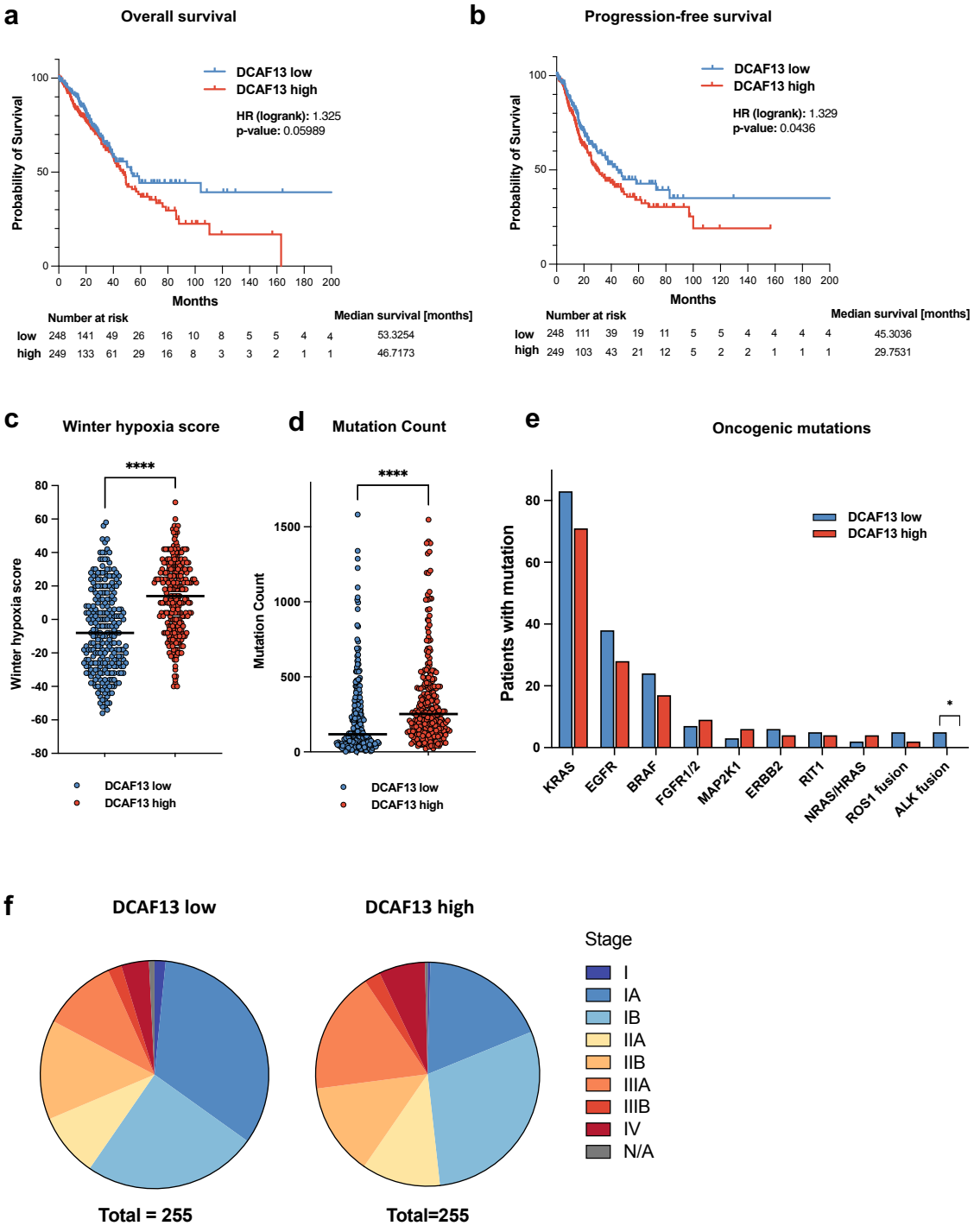

Figure 13: High DCAF13 expression correlates with aggressiveness and worse prognosis in patients with LuAD

Patients of the TCGA PanCancer Atlas LuAD cohort were separated into *DCAF13* low (log2(TPM+1) = 8.61-10.03) and *DCAF13* high (log2(TPM+1) = 10.037 – 12.14) groups. The groups were divided by median *DCAF13* expression. Kaplan-Meier plots for comparison of overall survival (**a**) and progression-free survival (**b**) between indicated groups. (**c**) Winter hypoxia score according to (Winter et al., 2007) for indicated patients. (**d**) total mutation count and (**e**) frequency of oncogenic alterations in indicated patient groups. Statistically significant comparisons are highlighted. (**f**) Relative frequency of indicated tumor stages according to the American Joint Committee on Cancer (AJCC) pathologic staging per patient group. Statistical testing was performed by Welch's t-test. **** : $p < 0.0001$, *** : $p < 0.001$, ** : $p < 0.01$, * : $p < 0.05$

5.1.4 DCAF13 is widely expressed across various cancer entities

To elucidate whether *DCAF13* overexpression is specific for lung cancer cells, the expression levels of a broad panel of cancer cell lines from different entities were investigated (Figure 14x). The publicly available expression data from the Dependency Map (DepMap) project (DepMap Consortium, 2018) was used to determine *DCAF13* expression and cell line clustering. As seen in figure 14X, lung cancer cell lines (marked in red) had the third-highest median *DCAF13* expression of all entities. Notably, most entities showed a higher median expression of *DCAF13* compared to non-cancerous fibroblasts (marked in blue), further hinting at a pro-tumorigenic role of DCAF13. Taken together, *DCAF13* overexpression is not limited to lung cancer and is present in many other entities, hinting at a more general oncogenic role of DCAF13 that is not limited to lung tumorigenesis.

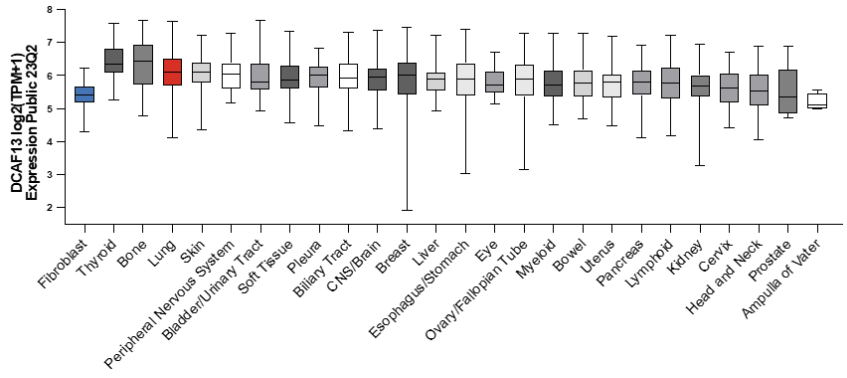

Figure 14: *DCAF13* expression across various cancer entities
Data for *DCAF13* expression levels was downloaded from the Dependency Map (DepMap) portal (DepMap Consortium, 2018). Cancer entities with less than four cell lines were excluded from the panel.

5.1.5 DCAF13 is highly expressed in various LuAD cell lines

To further confirm the observation that *DCAF13* is overexpressed in lung cancer versus non-cancerous fibroblasts, a large cell line panel of LuAD and other lung cancer subtypes was analyzed for *DCAF13* expression (Figure 15X). The lung fibroblast cell line IMR-90 was included as a non-cancerous cell line. *DCAF13* mRNA expression varied across different lung cancer subtypes but was increased in almost all cell lines compared to the non-cancerous IMR-90 cells (Figure 15a). The overexpression seemed even more striking on the protein level (Figure 15b), where IMR-90 cells showed by far the lowest levels of DCAF13. The cell line panel, therefore, confirmed the observation that DCAF13 is overexpressed in cancerous lung cells. Additionally, DCAF13 appeared to be expressed on mRNA and protein level in the embryonic kidney cell line HEK293T.

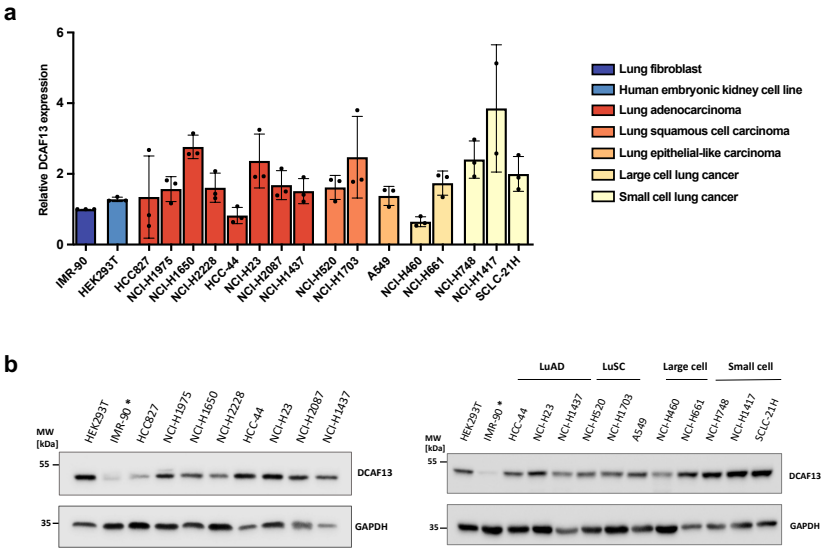

Figure 15: Lung cancer cell lines highly express DCAF13
DCAF13 levels were analyzed in the indicated cell lines. (**a**) Relative *DCAF13* mRNA expression of each cell line normalized to the expression in non-cancerous lung fibroblast cells IMR-90. Every dot indicates a biological replicate. Lung cancer subtypes are indicated by color. (**b**) Immunoblot analysis of DCAF13 protein levels in indicated cell lines. Non-cancerous lung fibroblast cells IMR-90 are marked with a star.

5.1.6 DCAF13 is essential for the proliferation and survival of LuAD cells

The results of the CRISPR screen identified *DCAF13* as a potential dependency of LuAD cell maintenance. To further validate this hypothesis, the apparent growth disadvantage was replicated in a competition assay. To this end, the Cas9-expressing cell lines used in the screen were lentivirally transduced with a construct expressing an sgRNA sequence and a GFP protein as a selection marker. For this experiment, the two sgRNAs that led to the most robust depletion across all cell lines in the screen were chosen to target *DCAF13*. Additionally, a non-targeting control (sgNT), and a positive control targeting an essential gene (sgPOLR2), were utilized. The cells were transduced with an appropriate amount of lentivirus to receive approximately 50% transduced cells, and the transduction efficiency was confirmed by flow cytometry analysis of GFP expression on day four after transduction. The ratio of transduced (GFP-positive) to non-transduced cells was monitored for 14 days by flow cytometry, as depicted in figure 16. The non-targeting controls behaved as expected, as they did not change in abundance over the observed timeframe. Interestingly, the experiment closely replicated the CRISPR screen results, as a dropout of cells transduced with sgRNAs targeting *DCAF13* was shown in all three cell lines, suggesting that *DCAF13* is indeed essential for LuAD cell survival. The strongest and weakest effects were observed in the NCI-H1437 and NCI-H23 cell lines, respectively, consistent with the data obtained from the screen. Hence, *DCAF13* was confirmed as a potential new oncogene and vulnerability in LuAD.

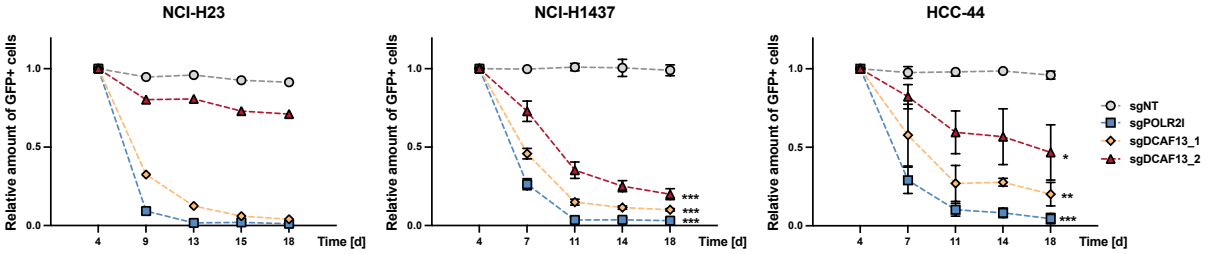

Figure 16: CRISPR-mediated knockout of DCAF13 leads to a growth disadvantage.
Cas9-expressing LuAD cells were lentivirally transduced with either a non-targeting sgRNAs (sgNT), an sgRNA targeting the essential gene RNA polymerase II (sgPOLR2I) as a positive control, or sgRNAs targeting DCAF13 to obtain a transduction rate of roughly 50%. Transduced cells also expressed the transgene GFP. The amount of GFP-positive cells was observed at the indicated time points by flow cytometry. Results are shown for each sgRNA in relation to day 4. The experiment was performed in triplicate for cell lines NCI-H1437 and HCC-44 and once for NCI-H23. Statistical testing was performed by Welsh's t-test. *** : $p < 0.001$, ** : $p < 0.01$, * : $p < 0.05$

5.2 DCAF13 depletion induces apoptotic cell death

5.2.1 DCAF13 depletion leads to a growth disadvantage in various LuAD cell lines

As discussed, *DCAF13* was identified as a novel vulnerability in LuAD cells. However, the molecular mechanisms behind LuAD dependency and the observed dropout phenotype after DCAF13 depletion remained unknown and needed to be explored. While the CRISPR/Cas9-system is a helpful tool for studying gene function, it also possesses disadvantages. Firstly, the knockout process requires some time to be fully implemented and does not occur in every cell simultaneously, thereby complicating precise cell biology studies and potentially weakening the effects of gene perturbation. Secondly, the cell-intrinsic DNA repair machinery will repair Cas9-induced double-strand breaks diversely and unpredictably, leading to highly heterogenous cell populations where some double-strand breaks will even be repaired to form silent mutations and not result in gene knockout. As a consequence, the following gene depletion studies were carried out through short-hairpin RNA (shRNA)-mediated knockdown. Lentiviral transduction of the shRNA-expressing vector was verified by evaluating the knockdown efficiency of the newly designed shRNAs. All three shRNAs targeting DCAF13 showed a distinct and reproducible reduction of DCAF13 protein levels (Figure 17).

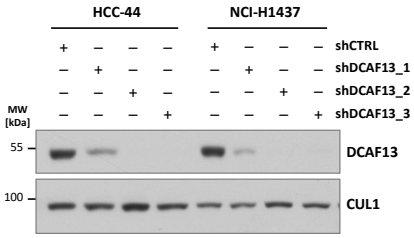

Figure 17: Immunoblot analysis of DCAF13 knockdown efficiency.
Indicated cell lines were lentivirally transduced with shRNAs targeting DCAF13. Cells were harvested four days post-transduction, and the knockdown efficiency was confirmed by immunoblotting with the indicated antibodies.

To further validate the suitability of the shRNA-mediated knockdown of DCAF13 in inducing a dropout phenotype, the previously described competition assay was repeated. For this, a lentiviral vector expressing the shRNA and a dsRed transgene was used, and the ratio of transduced (dsRed-positive) to non-transduced cells was monitored. Consistent with the knockout-based competition assay data, DCAF13 depletion led to a significant dropout of cells over time in the three cell lines used in the initial CRISPR screen (Figure 18a). Moreover, a stronger dropout phenotype was observed in cell lines NCI-H1437 and HCC-44 than in NCI-H23 cells, closely replicating the results of the sgRNA-based competition assay and the CRISPR screen.

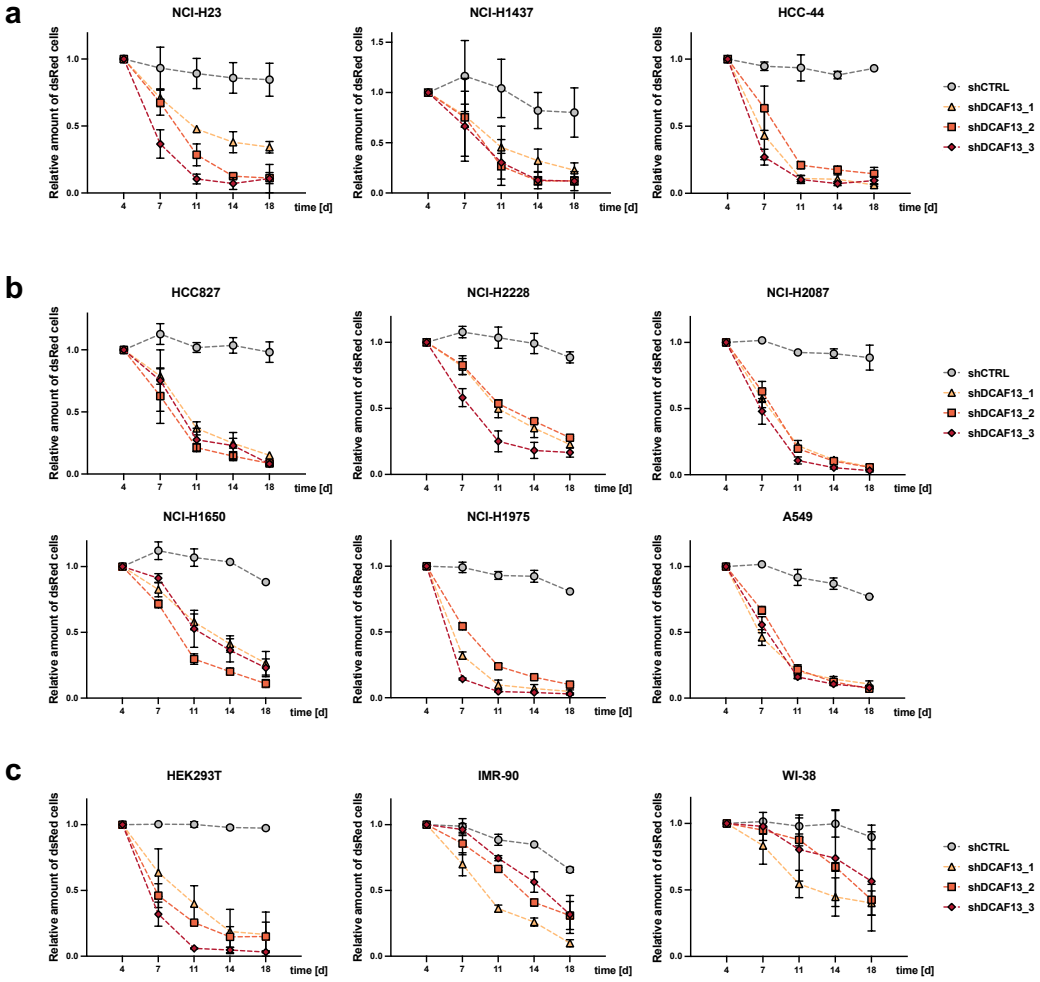

Figure 18: Knockdown of DCAF13 leads to a growth disadvantage in LuAD cell lines
Indicated cell lines were lentivirally transduced with either a non-targeting shRNA (shCTRL) or shRNAs targeting DCAF13 to obtain a transduction rate of roughly 50%. Transduced cells also expressed the transgene dsRed. The amount of dsRed-positive cells was observed at the indicated time points by flow cytometry. Results are shown for each shRNA in relation to day 4. The experiment was performed in triplicate for cell lines except IMR-90 and Wi-38, where the experiment was only performed twice. (**a**) Panel of cell lines used in the CRISPR/Cas9 screen (NCI-H23, NCI-H1437, HCC-44). (**b**) Panel of additional cell lines of the LuAD subtype (HCC827, NCI-H2228, NCI-H2087, NCI-H1650, NCI-H1975) and lung carcinoma epithelial cells (A549). (**c**) Panel of normal-like cell lines, including the embryonic kidney cell line HEK293T and two primary lung fibroblast cell lines (IMR-90, WI-38).

The competition assay was expanded to other LuAD cell line models (Figure 18b). Here, cells with DCAF13 depletion were consistently outcompeted by non-transduced cells, confirming that DCAF13 is essential in LuAD. The same effect was observed in the widely used transformed embryonic kidney cell line HEK293T (Figure 18c, left), indicating that the function of DCAF13 might not be limited to lung cancer cells. Interestingly, DCAF13 depletion exhibited a growth disadvantage in the two primary lung fibroblast cell lines, IMR-90 and WI-38. However, this effect appeared to be delayed compared to the LuAD cell lines. As the lung fibroblast cells also showed a decreased expression of DCAF13 (Figure 15), this could hint at a higher dependency of LuAD cells on DCAF13 levels than normal lung fibroblasts and highlights a potential therapeutic window for DCAF13-targeted therapy.

5.2.2 DCAF13 depletion does not affect the cell cycle

Lentiviral delivery and constitutive expression of the shRNA construct is a valuable tool for mechanistic studies. However, transduction rates are not always consistent and mixed populations of transduced and non-transduced cells can dilute the effects of gene perturbation. Consequently, a doxycycline-inducible shRNA expression vector was utilized to investigate the impact of DCAF13 depletion more consistently and in a more timely manner. Immunoblot analysis showed distinct DCAF13 depletion after induction of on-target shRNA expression by doxycycline but no alterations in cells expressing a non-targeting shRNA or cells treated with the vehicle control DMSO (Figure 19a). To further evaluate this model, the cells were induced with doxycycline or the vehicle control DMSO and counted for seven days. Cell numbers were normalized to the vehicle-treated control for each day. Consistent with the shRNA-based competition assay, DCAF13 depletion significantly reduced cell number in both cell lines, indicating that the doxycycline-inducible knockdown model is suitable to investigate the molecular changes upon DCAF13 depletion (Figure 19b).

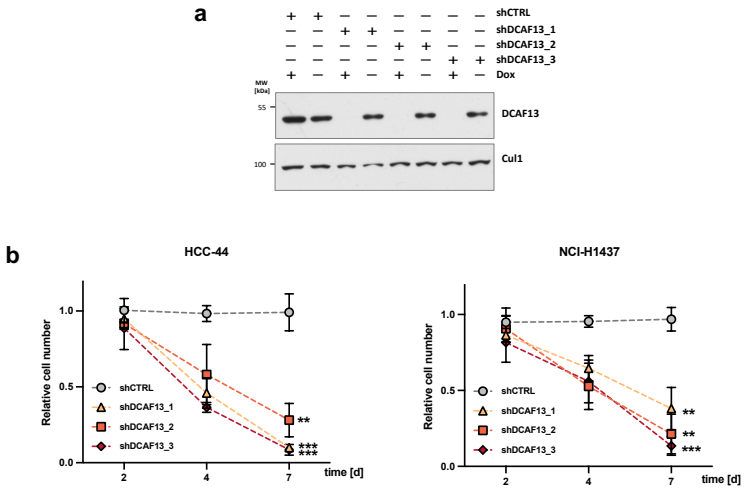

Figure 19: Doxycycline inducible DCAF13 knockdown replicates the observed growth disadvantage.
(**a**) Immunoblot analysis of NCI-H1437 cell lines expressing DCAF13-targeting shRNAs under a doxycycline-inducible promoter. Cells were induced with 1 µg/ml doxycycline or DMSO for 48 hours and immunoblotted for DCAF13 levels. (**b**) The cells with the indicated doxycycline-inducible shRNA expression constructs were induced with doxycycline or DMSO and counted at the indicated time points. Cell numbers are shown in relation to each construct's DMSO control. Statistical testing was performed by Welsh's t-test. *** : $p < 0.001$, ** : $p < 0.01$, * : $p < 0.05$

The evident dropout phenotype after DCAF13 depletion can result from two central cellular mechanisms: cell cycle impairment or cell death. Cell cycle impairment can present as increased cell cycle duration or cell cycle arrest. To investigate this, the cell cycle profile of LuAD cells after DCAF13 depletion was analyzed. To this end, DCAF13 knockdown was induced by doxycycline addition, and cells were analyzed by flow cytometric staining of DNA content through propidium iodide (PI). Cell cycle phases were allocated due to the expected DNA content: G1-phase ≈ 2n, S-phase ≥ 2n and ≤ 4n, and G2/M-phase ≈ 4n. The flow cytometric analysis (Figure 20) showed no apparent cell cycle arrest after four or seven days of DCAF13 depletion. An increase of cells in G2/M-phase was observed in HCC-44 cells treated with shDCAF13_1. However, this effect was not observed in the other cell line and seemed to be reduced in HCC-44 cells treated with the other two shRNAs, implying an off-target effect of shDCAF13_1. The slight increase in the G2/M cell compartment in the other two shRNAs hinted at a possible delay in mitosis. Nevertheless, this effect was insufficient to explain the potent depletion of cells with DCAF13 knockdown or knockout, hinting at cell death as the primary mechanism behind the dropout phenotype.

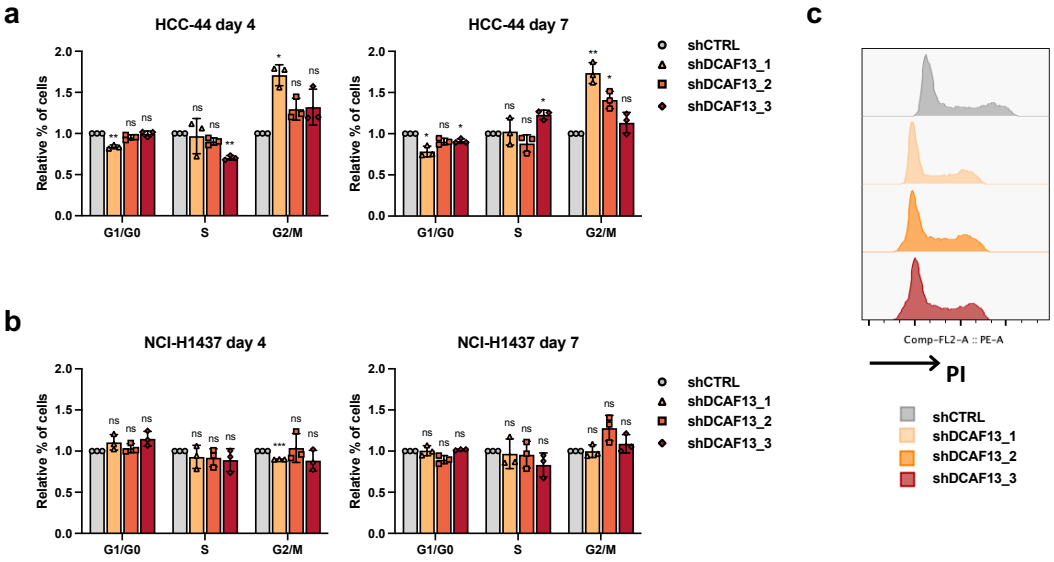

Figure 20: DCAF13 depletion does not significantly influence the cell cycle.
Doxycycline-inducible HCC-44 (**a**) and NCI-H1437 (**b**) cells were induced with 1 µg/ml doxycycline for the indicated time points, and the cell cycle was analyzed by flow cytometry by measuring the DNA content through staining with propidium-iodide. Cell cycle phases were annotated manually by the expected DNA content of G1-phase ≈ 2n, S-phase ≥ 2n and ≤ 4n, and G2/M-phase ≈ 4n. (**c**) Representative cell cycle profile of NCI-H1437 cells on day four after DCAF13 depletion. Statistical testing was performed by Welsh's t-test. *** : $p < 0.001$, ** : $p < 0.01$, * : $p < 0.05$, ns : p-value > 0.05. PI: Propidium iodide

5.2.3 DCAF13 depletion potently induces cell death

To investigate the hypothesis that the dropout phenotype is primarily mediated by cell death, flow cytometry staining for cell death was performed. Here, specific Annexin V staining and dye exclusion (Live/Dead-dye) principles were combined to measure cell death. Annexin V is a protein that specifically binds to phosphatidylserine (PS). PS is localized on the intracellular side of the plasma membrane in healthy cells. When cell death is induced, PS is switched to the extracellular side of the plasma membrane and can be detected by Annexin V (Banfalvi, 2017). The Live/Dead-dye cannot pass the intact cell membrane and is therefore excluded by

healthy cells and cells that are only in the early phases of apoptosis. Once the cell membrane is compromised, the dye can enter the cell and stains proteins, resulting in a potent fluorescent signal. Consequently, cells positive for Annexin V but negative for the Live/Dead staining are undergoing apoptosis, and double-negative cells are alive. Cells stained by the exclusion dye and Annexin V are classified as dead. Importantly, this assay cannot distinguish between apoptosis, necroptosis, and ferroptosis in the double positive population, as all of these types of cell death can be characterized by membrane rupture. While the translocation of PS to the outside of the membrane and subsequent staining by Annexin V is a characteristic trait of apoptosis, membrane rupture can lead to Annexin V binding PS from the inside of the cell and generating a “false positive” signal in necroptotic and ferroptotic cells (Pietkiewicz et al., 2015).

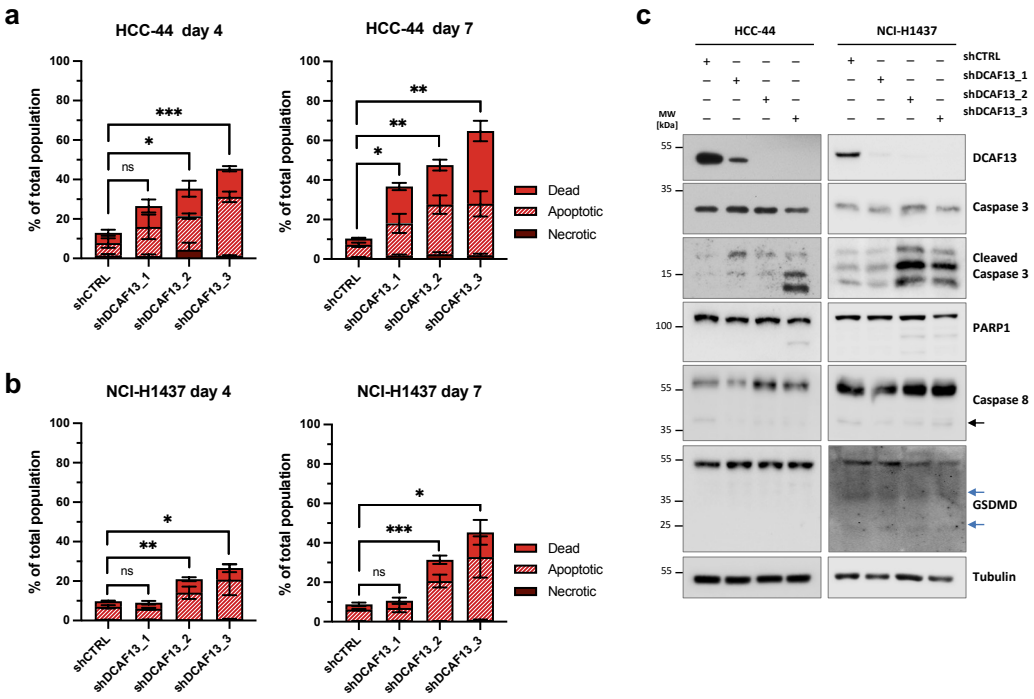

Figure 21: DCAF13 depletion induces cell death with caspase activation

Doxycycline-inducible HCC-44 (**a**) and NCI-H1437 (**b**) cells were induced with 1 µg/ml doxycycline for the indicated time-points, and cell death was analyzed by Annexin V and Live/Dead-dye staining through flow cytometry. Dead cells were defined as Annexin V and Live/Dead-dye-positive, apoptotic cells were defined as Annexin V-positive and Live/Dead-dye-negative, and necrotic cells were defined as Annexin V-negative and Live/Dead-dye-positive. (**c**) Immunoblot analysis of indicated cell death markers after DCAF13 depletion. Black and blue arrows indicate cleaved caspase 8 and cleaved GSDMD, respectively. Statistical testing was performed by Welsh’s t-test. *** : $p < 0.001$, ** : $p < 0.01$, * : $p < 0.05$, ns : p-value > 0.05.

As shown in figure 21, DCAF13 depletion significantly and potently increased the amount of apoptotic and dead cells, confirming the hypothesis that the dropout phenotype mainly results from cell death. Interestingly, the amount of apoptotic or dead cells was higher in HCC-44 cells than in NCI-H1437, replicating the competition and cell counting assay data, where a stronger dropout phenotype was observed in HCC-44 cells. Additionally, immunoblot analysis of caspase-3 cleavage was used to further determine the type of cell death (Figure 21c). Indeed, an increase in caspase-3 cleavage after DCAF13 depletion could be seen, hinting at a mostly apoptotic form of cell death (Banfalvi, 2017). Further, PARP1, a well-known substrate of active caspase-3 during apoptosis, appeared to be cleaved similarly to caspase-

3, supporting apoptosis as the central cell death mechanism (D. W. Nicholson, 1999). Interestingly, cleavage of caspase-8 could not be observed, indicating that DCAF13 depletion primarily induces apoptosis via the intrinsic pathway. An increase in Gasdermin D (GSDMD) cleavage was not observed, excluding pyroptosis as another potential cell death mechanism.

5.2.4 Caspase-inhibition abrogates cell death induced by DCAF13 depletion

Even though the previous observations convincingly showed that DCAF13 induces apoptotic cell death, it cannot be excluded that other cell death mechanisms contribute, as well. Thus, cells were treated with different cell death inhibitors to further characterize the type and mechanism of cell death induced by DCAF13 depletion. To this end, three compounds were used: the pan-caspase inhibitor Z-VAD-FMK, the RIPK1 inhibitor Necrostatin-1 (Nec-1), and the antioxidant Liproxstatin-1 (Lip-1). Z-VAD-FMK is widely used as an inhibitor of apoptosis due to the caspase-dependent nature of apoptotic cell death (Cohen, 1997). However, as it inhibits all major caspases, other caspase-dependent deaths, such as pyroptosis, may also be inhibited to a certain degree (J. Shi et al., 2015). As the name suggests, Nec-1 mainly blocks necroptosis as it is a potent RIPK1 inhibitor (Dong et al., 2022). However, as a specific pathway of TNF-induced apoptosis relies on RIPK1, it can be inhibited by Nec-1 as well (Dong et al., 2022; Wang et al., 2012). Lip-1 is a potent antioxidant that inhibits lipid peroxidation, which is essential for ferroptotic cell death (Fan et al., 2021).

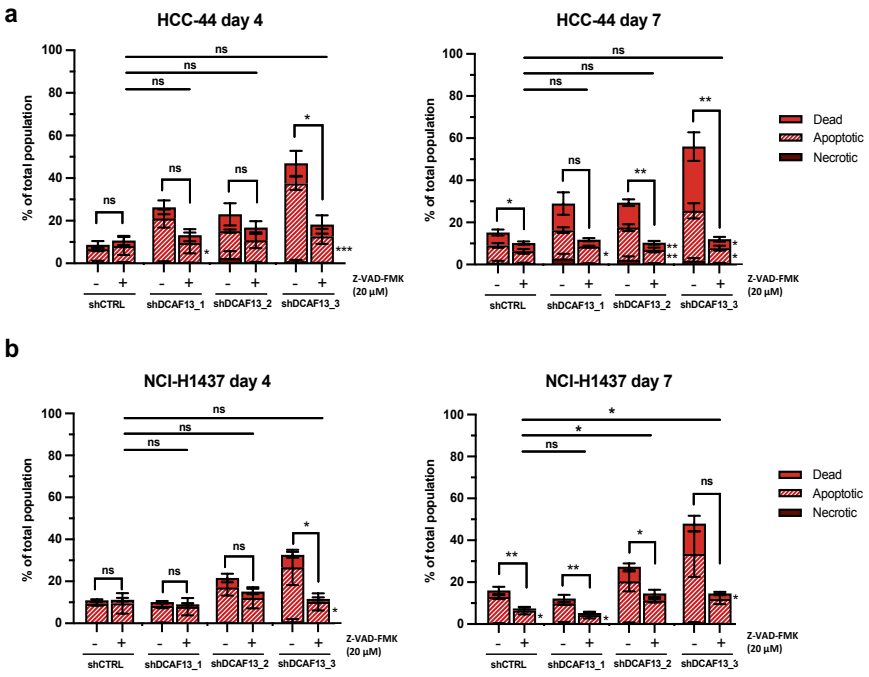

Figure 22: Caspase inhibition abrogates DCAF13 depletion-induced cell death
Doxycycline inducible HCC-44 (**a**) and NCI-H1437 (**b**) cells were induced with 1 µg/ml doxycycline and 20 µM Z-VAD-FMK or vehicle control for the indicated time points, and cell death was analyzed by Annexin V and Live/Dead-dye staining through flow cytometry. Dead cells were defined as Annexin V and Live/Dead-dye-positive, apoptotic cells were defined as Annexin V-positive and Live/Dead-dye-negative, and necrotic cells were defined as Annexin V-negative and Live/Dead-dye-positive. Statistical testing was performed by Welsh's t-test. Comparisons were drawn between the sum of dead, apoptotic, and necrotic cells, as indicated by the brackets. Additionally, the cell death fractions were compared between the cells treated with Z-VAD-FMK and DMSO, and significance is indicated by the stars next to the individual groups. *** : $p < 0.001$, ** : $p < 0.01$, * : $p < 0.05$, ns : p-value > 0.05.

Figure 22 shows the amount of apoptotic and dead cells after treatment with Z-VAD-FMK. Strikingly, the observed cell death after DCAF13 depletion is entirely abolished by the addition of the caspase inhibitor, indicating that the mechanism of cell death is entirely dependent on caspases.

The addition of necroptosis (Nec-1) or ferroptosis (Lip-1) inhibitors did not significantly reduce the number of dead cells (Figure 23). Interestingly, Nec-1 appeared to induce a slight reduction of apoptotic cells, albeit not a complete rescue. As Nec-1 is a RIPK1 inhibitor and a distinct apoptosis pathway can involve RIPK1 signaling, this could further hint at a potential molecular mechanism (Dong et al., 2022). Overall, it can be concluded that the cell death mechanism induced by DCAF13 depletion depends entirely on caspase activation. As mentioned, pyroptotic cell death also heavily relies on caspases. However, considering that no cleavage of GSDMD, a hallmark of pyroptosis, was observed by immunoblotting (Figure 21c), these observations corroborate that DCAF13 depletion induces apoptosis.

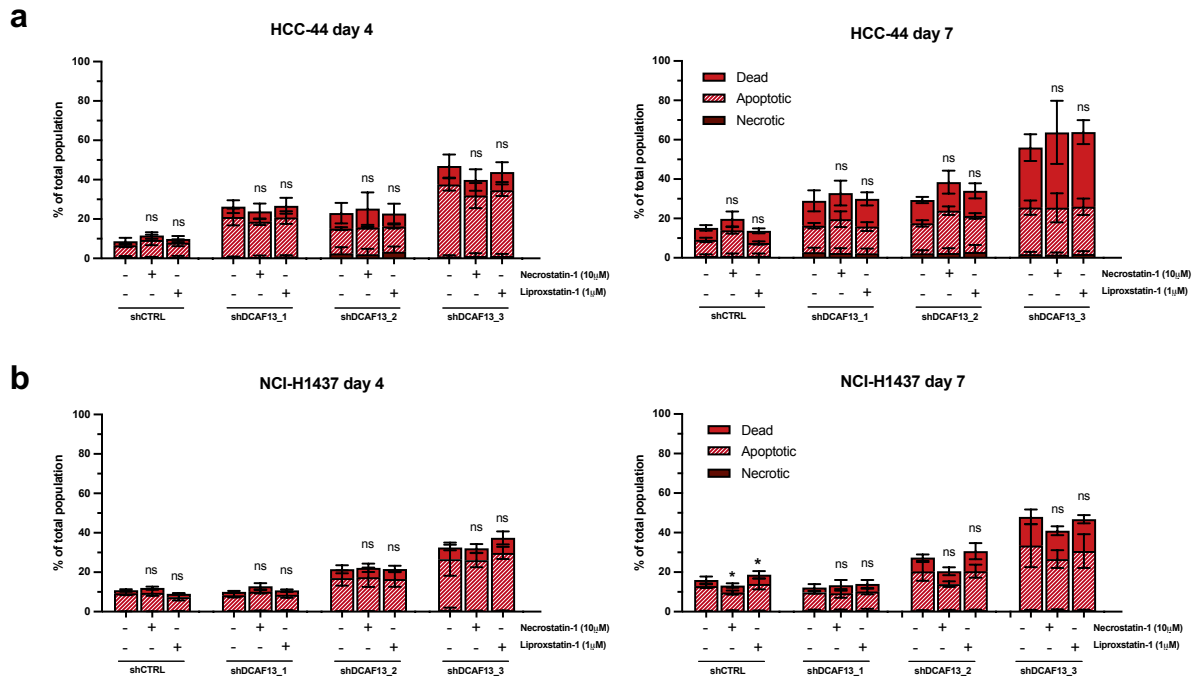

Figure 23: Necroptosis and ferroptosis inhibitors do not prevent cell death upon DCAF13 depletion
Doxycycline-inducible HCC-44 (**a**) and NCI-H1437 (**b**) cells were induced with 1 µg/ml doxycycline and 10 µM Necrostatin-1, 1 µM Liproxstatin-1, or vehicle control for the indicated time-points and cell death was analyzed by Annexin V and Live/Dead-dye staining through flow cytometry. Dead cells were defined as Annexin V and Live/Dead-dye-positive, apoptotic cells were defined as Annexin V-positive and Live/Dead-dye-negative, and necrotic cells were defined as Annexin V-negative and Live/Dead-dye-positive. Statistical testing was performed by Welsh's t-test. Comparisons were drawn between the sum of dead, apoptotic, and necrotic cells, as indicated by the brackets. *** : $p < 0.001$, ** : $p < 0.01$, * : $p < 0.05$.

5.2.5 DCAF13 depletion induces apoptosis via the intrinsic pathway

Figure 21c shows that DCAF13 depletion did not induce cleavage of caspase-8, suggesting that the primary mechanism of apoptosis induction occurs through the intrinsic pathway. To test this hypothesis, mitochondrial membrane destabilization was examined. To this end, the JC-1 dye was employed to indicate mitochondrial membrane potential. As depicted in figure 24a, JC-1 accumulates in intact mitochondria and forms aggregates with red fluorescence,

indicating healthy cells. In case of mitochondrial membrane disruption, such as during apoptosis, JC-1 diffuses into the cytoplasm and is present in a monomeric form with green fluorescence. Therefore, a decrease in the ratio of red/green fluorescence intensity indicates mitochondrial destabilization and intrinsic apoptosis.

As seen in figure 24b, cells depleted for DCAF13 displayed a substantial increase in green fluorescence staining, indicating disrupted mitochondrial potential. This was further confirmed by quantifying the fluorescence intensity (Figure 24c), where DCAF13 depletion significantly reduced the red/green fluorescence ratio. Taken together, this observation, combined with the previously described immunoblotting experiments, confirms that DCAF13 depletion induces apoptosis through the intrinsic pathway.

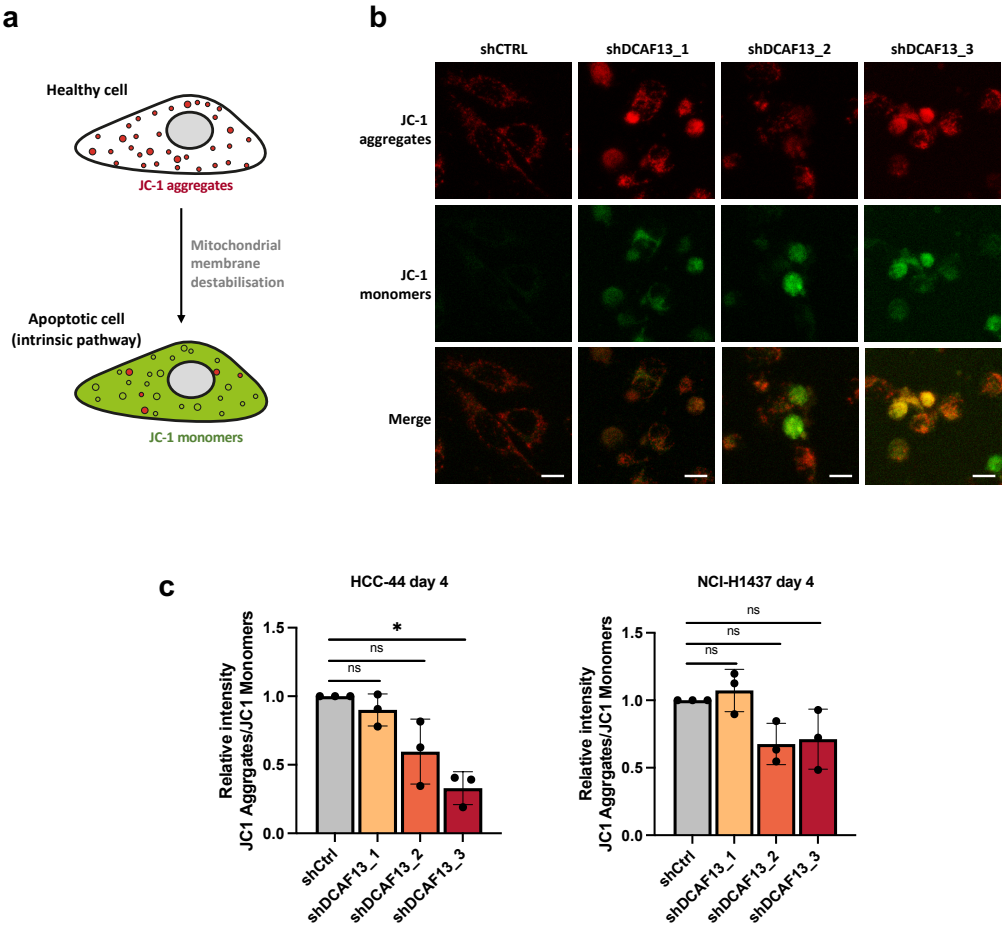

Figure 24: DCAF13 depletion induces mitochondrial membrane destabilization

(**a**) Schematic representation of the JC-1 mitochondrial membrane destabilization assay. JC-1 accumulates in intact mitochondria in healthy cells and forms aggregates of red fluorescence. Upon mitochondrial membrane destabilization during apoptosis, the JC-1 diffuses into the cytoplasm and is present in a monomeric form with green fluorescence. (**b**) Fluorescence microscopy of the JC-1 probe upon DCAF13 depletion. Doxycycline inducible HCC-44 cells were induced with 1 µg/ml doxycycline for four days and stained with the JC-1 probe. Nuclei were counterstained with Hoechst 33342. Images are representative of three biological experiments, and the scale bar indicates 20 µm. (**c**) Quantification of the fluorescence intensity of red (JC-1 aggregates) and green (JC-1 monomers) fluorescence. Doxycycline inducible HCC-44 and NCI-H1437 cells were induced with 1 µg/ml doxycycline for four days and stained with the JC-1 probe. Fluorescence was quantified with a plate reader. Statistical testing was performed by Welsh's t-test. * : $p < 0.05$.

5.3 DCAF13 predominantly localizes to the nucleus in LuAD cells

The function of a protein is often closely linked to its localization in a specific cellular compartment. Hence, to further characterize the role of DCAF13 in LuAD, immunofluorescence staining of its subcellular localization was performed. To this end, an antibody targeting endogenous DCAF13 needed to be validated.

Figure 25a shows a distinct nuclear localization of DCAF13, shown by co-staining with Hoechst 33342, in NCI-H1437 and HCC-44 cells, which was confirmed by loss of staining after DCAF13 depletion. Overexpression of double-strep-single-FLAG(SF)-tagged DCAF13 protein further confirmed dominant nuclear localization, as indicated by white arrows.

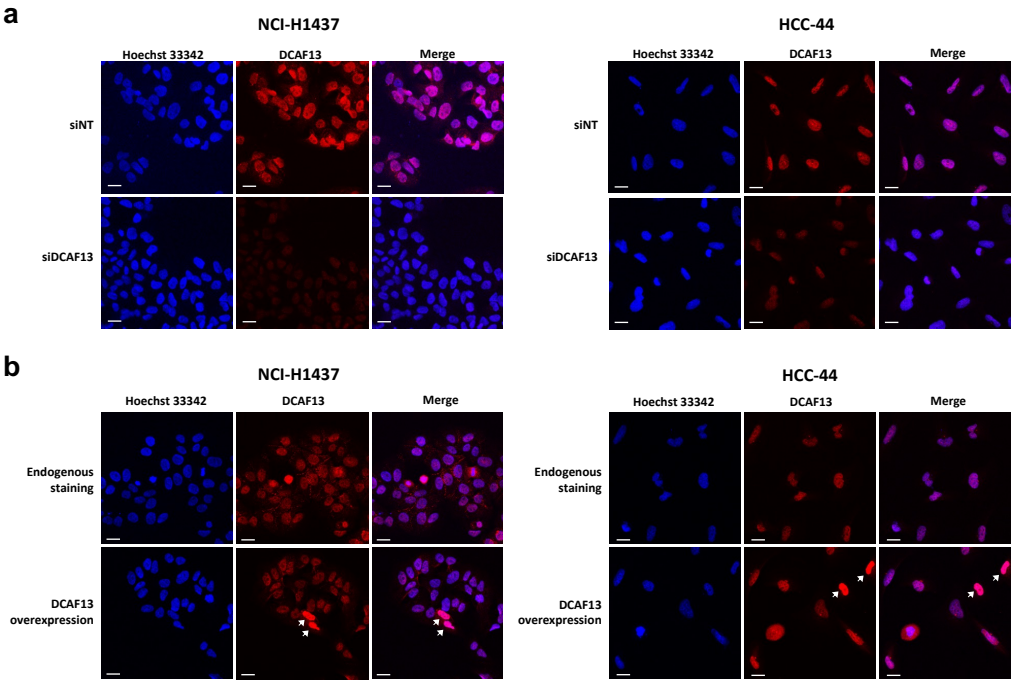

Figure 25: Validation of the antibody for immunofluorescence staining of endogenous DCAF13
Immunofluorescence staining with the antibody targeting DCAF13 in HCC-44 and NCI-H1437 cells with (**a**) siRNA-mediated knockdown of DCAF13 or (**b**) overexpression of SF-tagged DCAF13. Cells with overexpression are indicated by white arrows. The scale bar represents 20 µm

A closer look at the cells revealed an additional singular dot-like structure of DCAF13 staining. In mammalian cells, a distinct dot-like structure next to the nucleus often constitutes the centrosome. The centrosome is a cellular organelle involved in cell cycle progression and functions as the cell's primary microtubule organizing center (mTOC) (J. Wu & Akhmanova, 2017). To investigate if DCAF13 could be localized to the centrosome, a co-staining with the centrosomal marker Centrin-3 (CETN3) was performed. Indeed, as shown in Figure 26, the dot-like structure stained by the anti-DCAF13 antibody fully overlapped with the Centrin-3 staining in both cell lines. In addition, the cells were stained with phalloidin to visualize the actin cytoskeleton. In NCI-H1437 cells, which grow in patches with close contact with other cells, F-actin staining mainly accumulates at the cell membrane between neighboring cells. Here, a closer look revealed another distinct dot-like staining for DCAF13 at the border between neighboring cells. As these dotted structures are not present at the whole cell membrane but

only at the edge of another cell, these structures likely represent a form of cell-to-cell contact. These structures are not visible in HCC-44 cells, as they are somewhat migratory and do not grow in groups, likely limiting the number of cell-to-cell contacts they form. Taken together, it could be shown that DCAF13 predominantly localizes to the nucleus, with additional localization to the centrosome and cell-to-cell contacts in LuAD cells.

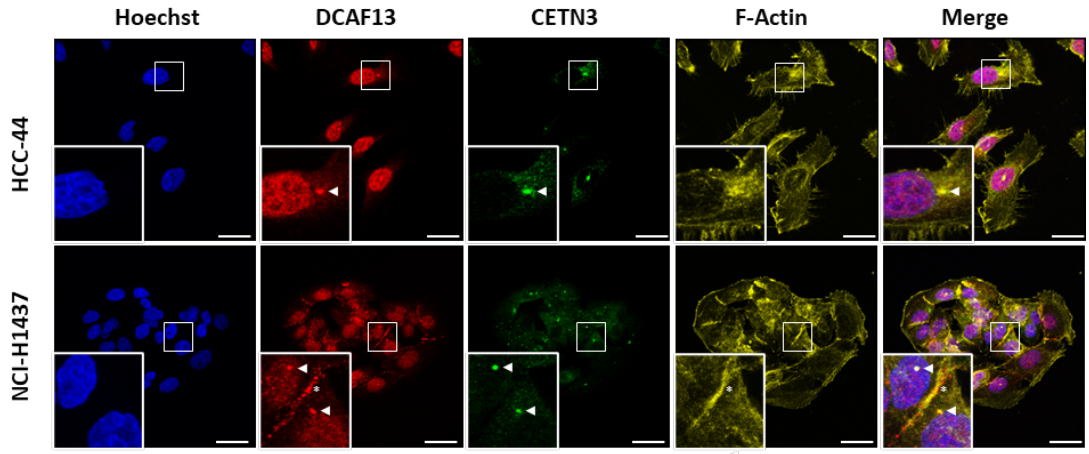

Figure 26: DCAF13 predominantly localizes to the nucleus, the centrosome, and cell contacts in LuAD cells

Co-staining of endogenous DCAF13 with the centrosomal marker centrin-3 (CETN3). Zoomed segments are indicated by white boxes. F-Actin was stained by fluorescently labeled Phalloidin. Nuclei were counterstained with Hoechst 33342. Arrowheads indicate centrosomal localization. Asterisks indicate cell-to-cell contacts. The scale bar represents 30 µm.

5.4 DCAF13 depletion deregulates actin cytoskeleton formation

5.4.1 Transcriptomics implicate a role of DCAF13 in cytoskeleton organization

As shown in the previous chapter, DCAF13 predominantly localizes to the nucleus, implying that it could have a function in transcription control. To test this hypothesis and to further identify the cellular changes that might be responsible for apoptotic cell death after DCAF13 depletion, transcriptomic analysis was performed in the form of RNA sequencing. To this end, cell lines HCC-44 and NCI-H1437 were lentivirally transduced with a non-targeting shRNA (shCTRL) or two different shRNAs targeting DCAF13, as seen in Figure 27a. Samples were harvested prior to transduction and after 48 hours and 96 hours, to investigate early and late changes in gene expression, respectively. Two different shRNAs were chosen to reduce the influence of off-target effects of the individual shRNAs. Immunoblotting of the samples prior to transcriptome analysis showed distinct depletion of DCAF13 in all samples transduced with an shRNA targeting DCAF13 (Figure 27b). The knockdown of DCAF13 was further confirmed by the transcriptome analysis, where *DCAF13* appeared as the most significantly downregulated gene in all conditions (Figure 27c-f).

To achieve a more holistic understanding of the transcriptional changes than identifying singular differentially expressed genes, gene set enrichment analysis (GSEA) was performed by Dr. P. Auf der Maur. To this end, curated gene sets (Hallmark, C2, C5) from the Molecular Signatures Database (MSigDB) were used. The analysis was performed for each on-target

shRNA, each time-point, and each cell line separately. The five most significantly altered gene sets per condition were chosen, and a list of these altered gene sets was used to identify patterns shared between the different shRNAs and time-points (Figure 28).

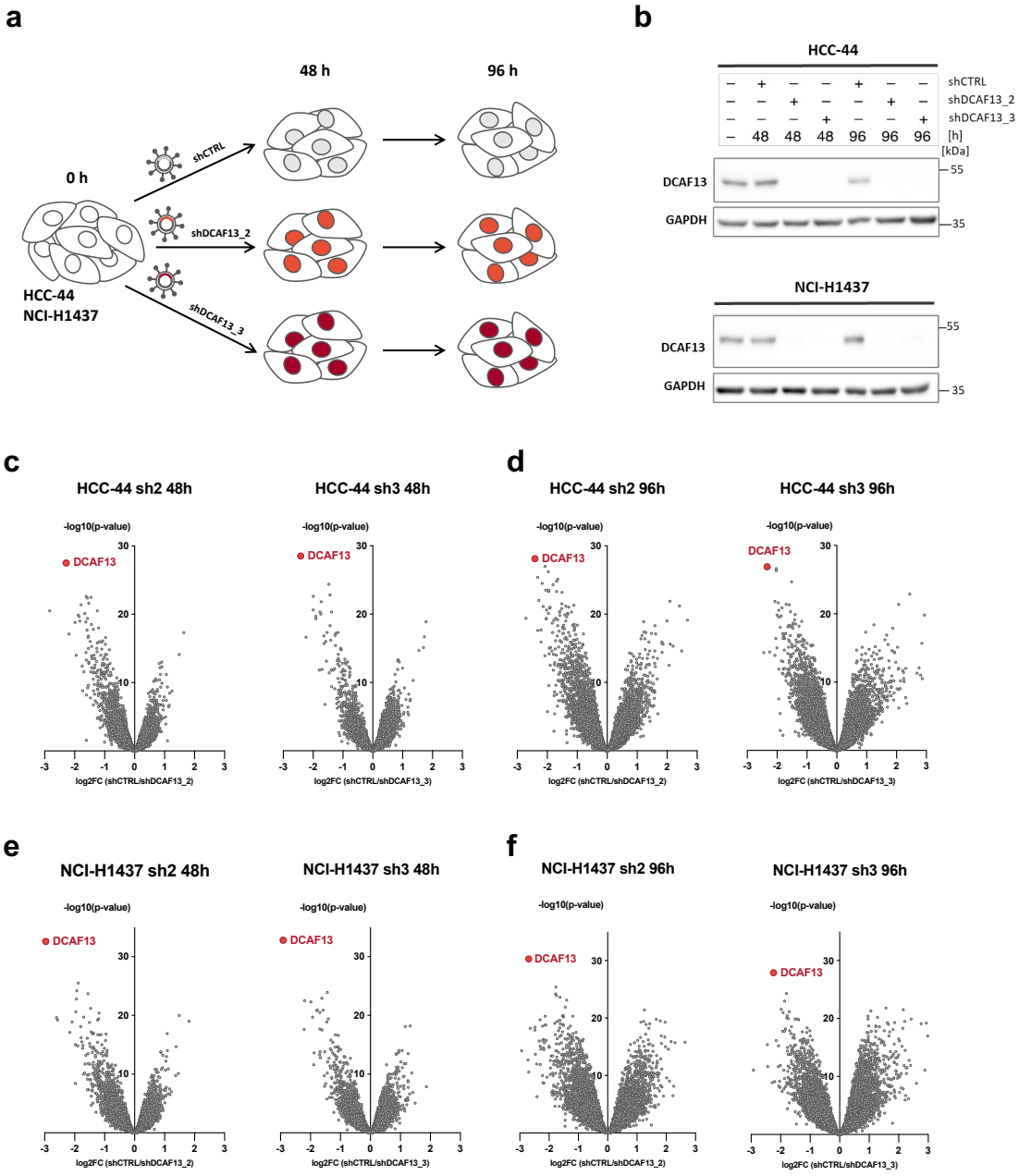

Figure 27: Analysis of the transcriptome upon DCAF13 depletion

Transcriptomic changes upon DCAF13 depletion were investigated by RNA sequencing. (**a**) schematic of the experimental setup. RNA sequencing was performed in the two cell lines HCC-44 and NCI-H1437 with two lentiviral shRNA constructs targeting DCAF13 (shDCAF13_2, shDCAF13_3), as well as a non-targeting shRNA (shCTRL). Samples were collected 48 hours and 96 hours post-transduction. The experiment was performed with three biological replicates. (**b**) Representative immunoblot analysis of DCAF13 depletion in one biological replicate of indicated samples. Volcano plots of transcriptional changes for each DCAF13-targetting shRNA construct in comparison to the non-targeting shRNA (shCTRL) in HCC-44 cells after 48 hours (**c**) and 96 hours (**d**) and in NCI-H1437 cells after 48 hours (**e**) and 96 hours (**f**). Statistics were calculated using the edgeR framework (Y. Chen et al., 2016)and the glmQLFTest function. [Analysis of data for c-f provided by Dr. P. Auf der Maur]

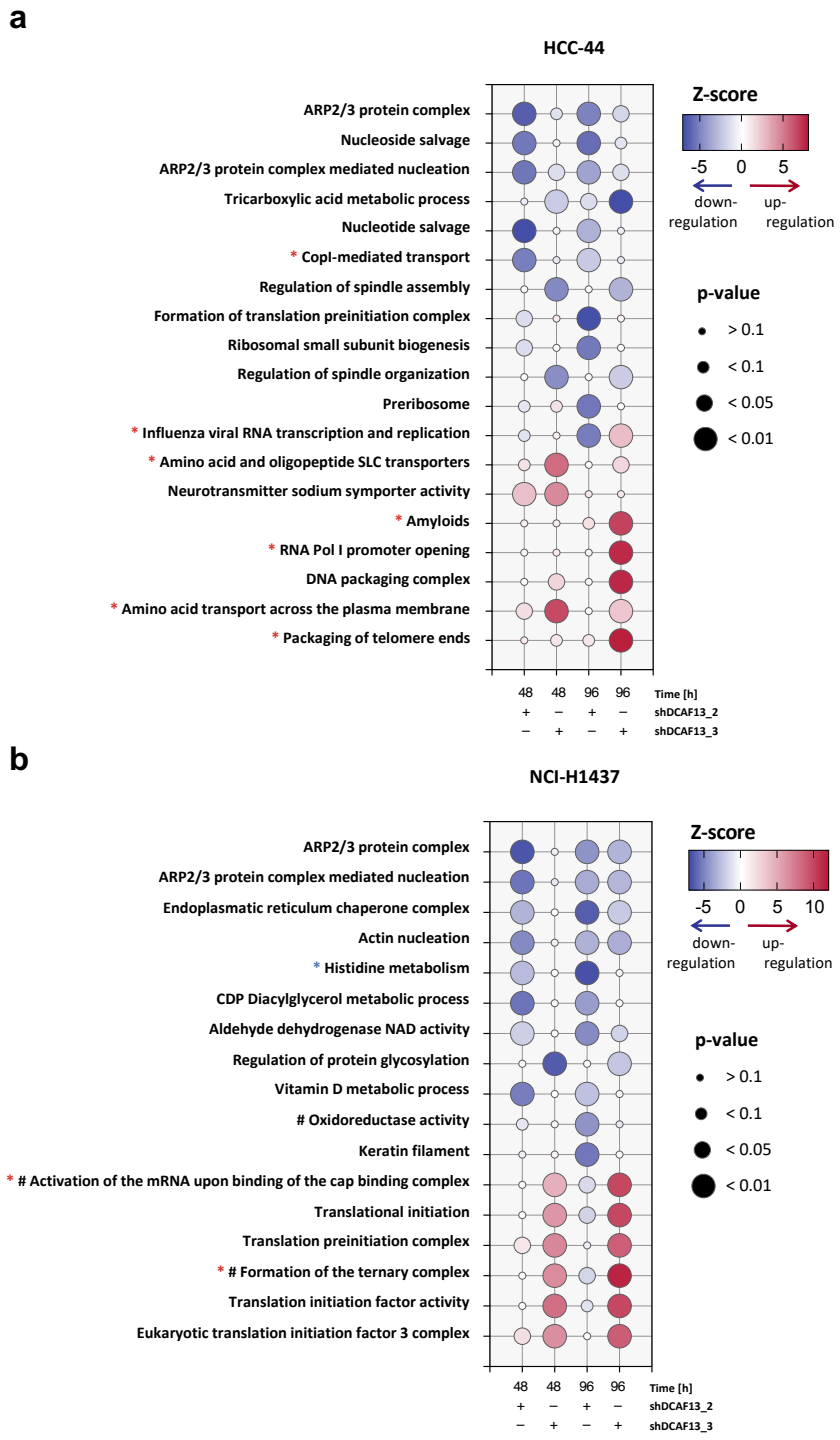

Figure 28: Gene Set Enrichment Analysis indicates actin nucleation defects upon DCAF13 depletion.
Gene Set Enrichment Analysis (GSEA) was performed for the transcriptomic changes upon DCAF13 depletion. Gene sets (Hallmark, C2, C5) were downloaded from the Molecular Signatures Database (MSigDb). The analysis was performed separately for each DCAF13-targeting shRNA, compared to shCTRL, each time point, and each cell line. The five most significantly deregulated gene sets were chosen per condition, and a list of these gene sets was made per cell line. Bubble plots for the most significantly changed gene sets for all conditions in HCC-44 (**a**) and NCI-H1437 (**b**) cells. The bubble size denotes the significance of the gene set alteration, and the bubble color represents a z-score, the -log10(p-value) multiplied by the direction of the alteration (up = 1, down =-1). Statistics were calculated using the edgeR framework (Y. Chen et al., 2016) and the glmQLFTest function. Gene sets with red asterisks are from the REACTOME pathway collection, blue asterisks represent the KEGG pathway collection, and gene sets without asterisks are from the GO-term collection. The hashtag shows a shortening of the name of the gene set for visualization purposes. [GSEA provided by Dr. P. Auf der Maur]

Strikingly, the ARP2/3 protein complex pathway appeared to be one of the most deregulated pathways and was distinctly downregulated upon knockdown of DCAF13 in almost all conditions of both cell lines. Two similar gene sets, “ARP2/3 protein complex-mediated actin nucleation” and “actin nucleation”, were similarly downregulated and shared between both cell lines. Actin nucleation describes the initial step of actin filament formation (Moseley & Goode, 2006). Deregulation of this process could therefore lead to a reduction of several actin structures in the cell, such as actin stress fibers, which are essential for cell

homeostasis. The ARP2/3 protein complex is a highly conserved protein complex responsible for the initial nucleation step in actin filament branching (Nolen & Pollard, 2008). Notably, the actin cytoskeleton is largely involved in cell surface adhesion (Kovacs & Yap, 2002). Accordingly, this could imply that DCAF13 depletion reduces actin structures and possibly reduces cell adhesion. As organization of the cytoskeleton and attachment of cells to the microenvironment are particularly essential in the context of cell culture, these phenotypic changes could potentially account for the observed cell death.

5.4.2 DCAF13 depletion abrogates actin stress fiber formation

To investigate the hypothesis that DCAF13 depletion leads to a defect in actin structure formation, doxycycline-inducible HCC-44 cells were treated with doxycycline to induce non-targeting or DCAF13-targeting shRNA expression. Cells were fixed and stained for F-actin by phalloidin, as seen in figure 29a. In the control condition (shCTRL), every cell showed the formation of so-called actin stress fibers, which are long actin filaments that can span the entire length of a cell. These fibers are essential for cell adhesion and motility (Pellegrin & Mellor, 2007). Additionally, the cells appeared to be spread out and adequately attached to the plastic surface of the cell culture dish. In contrast, cells with DCAF13 depletion did not exhibit long actin stress fibers but rather dotted and disorganized F-actin staining. Strikingly, the quantification of this effect showed a clear enrichment of cells without discernible actin stress fibers in cells depleted for DCAF13 (Figure 29b).

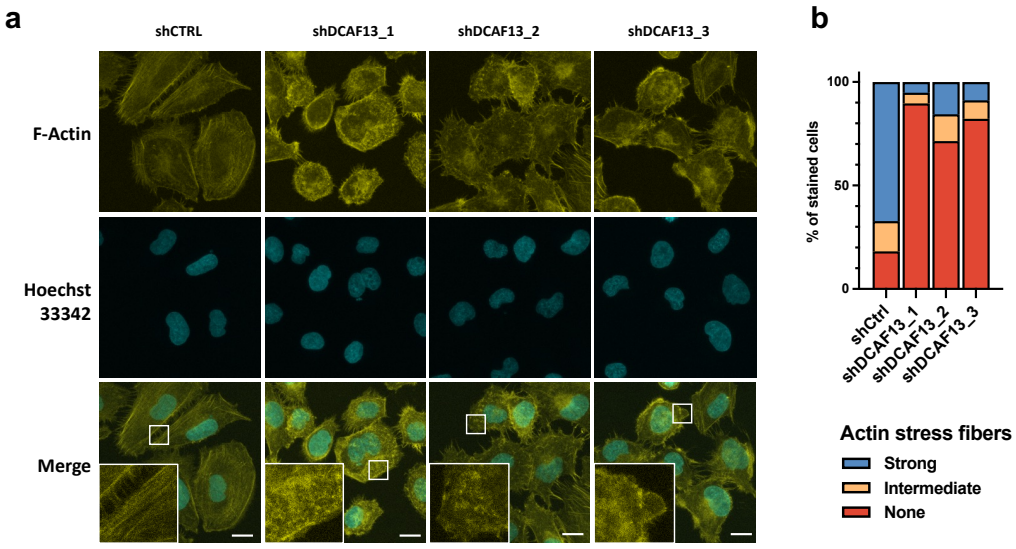

Figure 29: DCAF13 depletion abolishes actin stress fiber formation.
Doxycycline inducible HCC-44 cells were induced with 1 µg/ml doxycycline for 72 hours and fixed with formaldehyde. Immunofluorescent staining for F-actin by fluorescence-coupled phalloidin was performed (**a**). Nuclei were counterstained with Hoechst 33342 (**b**) Qualitative assessment of the presence of actin stress fibers after DCAF13 depletion. Cells were assessed for strong, intermediate, or no actin stress fiber formation. More than 70 cells were counted in five representative images per condition. The scale bar represents 20 µm.

As the gene sets for actin nucleation were significantly downregulated upon DCAF13 depletion in the transcriptomic analysis, a defect in actin nucleation could be the primary mechanism behind the observed loss of actin stress fibers. Further, the cell's morphology

appeared to be less spread and more rounded. This could indicate that the observed defect in actin fiber formation might lead to cell rounding and ultimately to cell detachment after DCAF13 loss.

Actin was shown to be a cleavage substrate of caspases in mammalian cells (Mashima et al., 1997, 1999). As DCAF13-depleted cells undergo apoptosis, it is conceivable that the loss of actin stress fibers is not directly induced by DCAF13 depletion but rather an effect of caspase activation during apoptosis. To test this hypothesis, DCAF13 knockdown was induced in HCC-44 cells, and 20 µM Z-VAD-FMK or vehicle control was added for four days. As previously shown in chapter 5.2.4, adding the caspase inhibitor Z-VAD-FMK completely abrogates apoptosis induced by DCAF13 depletion through caspase inhibition. Strikingly, the addition of the caspase inhibitor did not alter the loss of actin stress fibers in cells depleted for DCAF13 (Figure 30). Thus, it was concluded that the defect in actin stress fiber formation upon DCAF13 depletion is not a secondary effect of caspase activation during apoptosis. Further studies need to be conducted to determine if the opposite could be true and if the deregulation of the actin cytoskeleton upon DCAF13 depletion ultimately induces apoptosis.

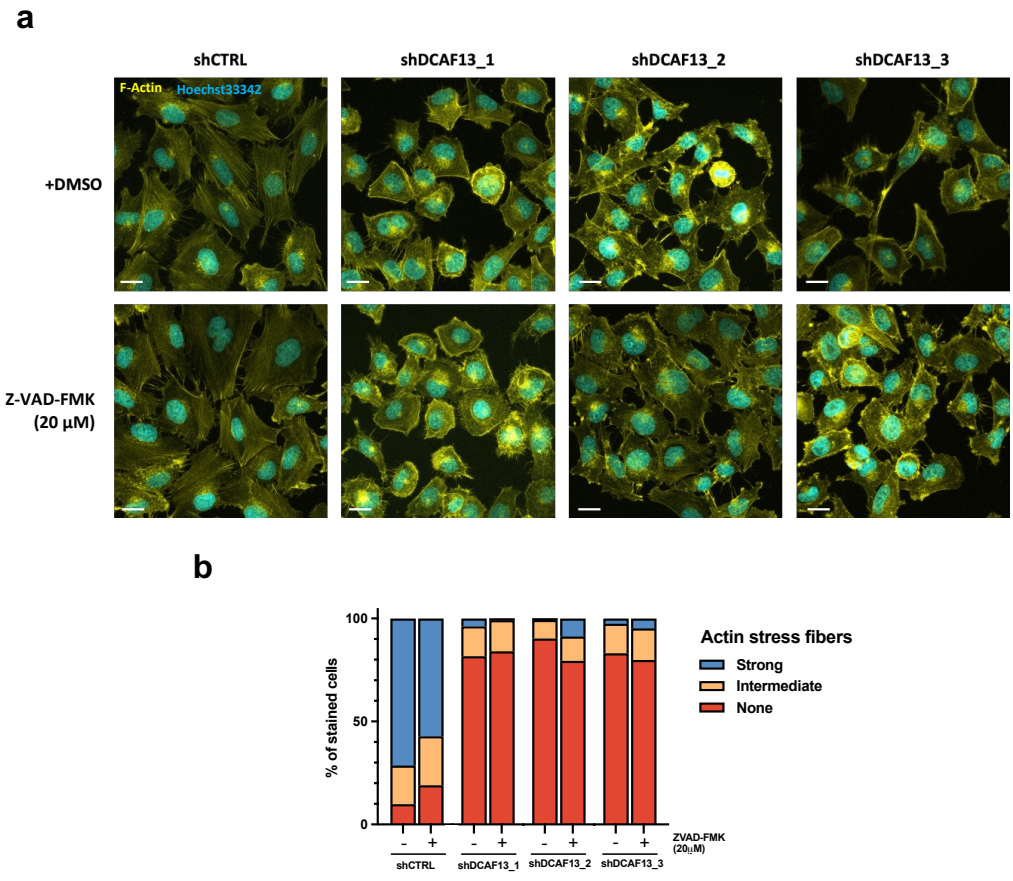

Figure 30: Caspase inhibition does not abrogate actin stress fiber formation defects upon DCAF13 depletion

Doxycycline inducible HCC-44 cells were induced with 1 µg/ml doxycycline and 20 µM Z-VAD-FMK or vehicle control for four days and fixed with formaldehyde. Immunofluorescent staining for F-actin by fluorescence-coupled phalloidin was performed (**a**). (**b**) Qualitative assessment of the presence of actin stress fibers. Cells were assessed for strong, intermediate, or no actin stress fiber formation. More than 100 cells were counted in six representative images per condition. The scale bar represents 20 µm.

5.5 Characterization of DCAF13 ubiquitination substrates

5.5.1 DCAF13 is a component of a CUL4 ubiquitin ligase complex

DCAF13 is predicted to be a substrate-recruiting unit for a ubiquitin ligase complex of the CUL4 family (Figure 31a), and recent reports have supported this prediction (Z. Chen et al., 2018; Y. Zhang et al., 2018). Hence, it is likely that DCAF13 exerts its physiological function via interaction with and ubiquitination of its designated substrates. However, since DCAF13 does not have inherent enzymatic activity, it is imperative that it interacts with the other proteins of the cullin ring ligase (CRL) complex in the cell to induce ubiquitination of its substrates. To investigate if this interaction takes place in LuAD cells, immunoprecipitation (IP) with a tagged DCAF13 protein was performed. As shown in figure 31b, DDB1 and CUL4A co-precipitated with DCAF13, suggesting that DCAF13 can form a functional ubiquitin ligase complex in the cell. Surprisingly, an interaction with CUL4B could not be observed.

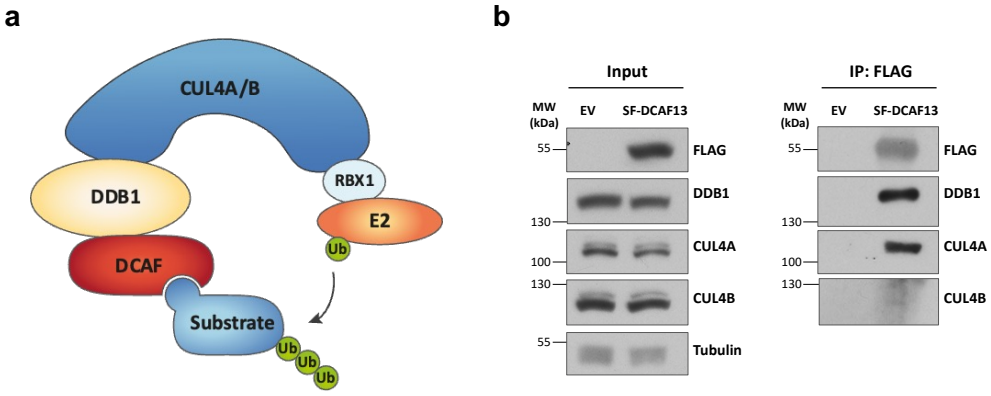

Figure 31: DCAF13 forms a ubiquitin ligase complex with CUL4A and DDB1
(**a**) Schematic representation of the CUL4 ligase complex. (**b**) Immunoprecipitation (IP) of SF-tagged DCAF13 from HEK293T cells. Cells were transiently transfected with an SF-DCAF13 expressing plasmid, and cell lysates were subjected to FLAG-IP and subsequent immunoblotting with the indicated antibodies. EV: Empty vector.

5.5.2 Large-scale screening for DCAF13-interacting proteins

This study combined two screening approaches to identify relevant ubiquitination substrates of DCAF13. Firstly, interactors of DCAF13 were analyzed by performing large-scale immunoprecipitation and subsequent identification of co-purified proteins via mass spectrometry. Secondly, a functional approach was chosen, in which the ubiquitin-modified proteome of the cell was investigated upon DCAF13 depletion. To this end, diGLY proteomics was employed. Proteins co-purified as interactors of DCAF13 and shown to be less ubiquitinated upon DCAF13 depletion were further investigated as potential ubiquitination substrates.

There are several methods to identify interaction partners of a protein of interest. An affinity-based approach, in the form of a large-scale FLAG-immunoprecipitation (FLAG-IP), was chosen for this study. To this end, an overexpression construct of N-terminally tagged DCAF13 was produced. Unfortunately, a FLAG-tagged construct of DCAF13 resisted cloning.

Accordingly, the previously described double-strep-single-FLAG-tagged (SF-DCAF13) expression construct was employed for this experiment.

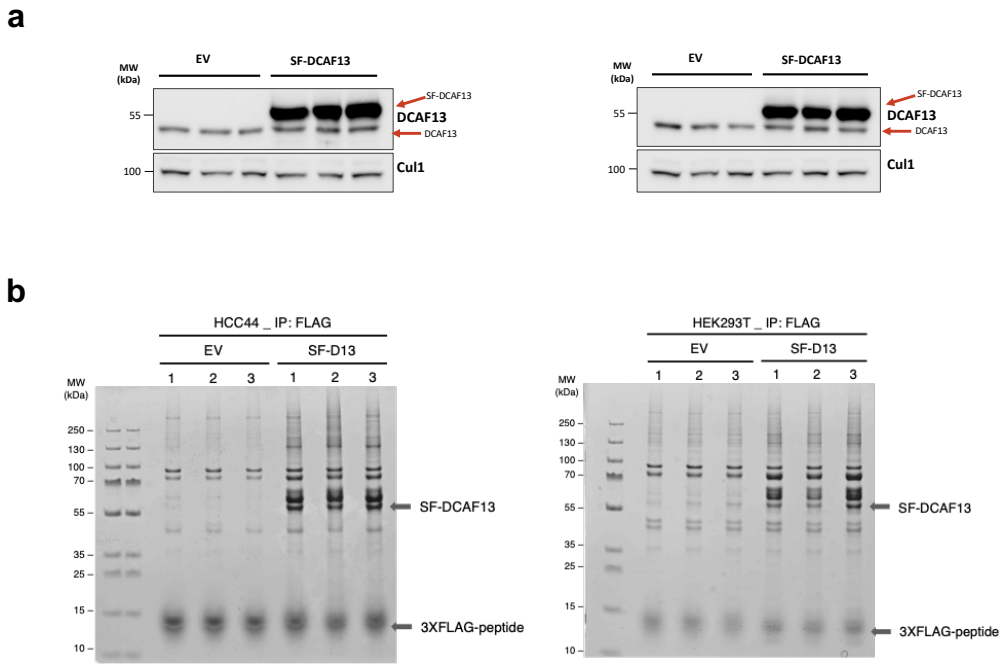

Figure 32: Interactome screening for DCAF13 substrates in HCC-44 and HEK293T cells
(**a**) Immunoblot analysis of cell lysates from HCC-44 (left) and HEK293T (right) cells transduced to express SF-DCAF13 or empty vector controls (EV). (**b**) Coomassie staining of purified proteins after FLAG-immunoprecipitation (FLAG-IP). After immobilization on anti-FLAG-resin and elution with 3x-FLAG peptide, 100% (HCC-44, left) or 50% (HEK293T, right) of the eluate were subjected to SDS-PAGE and coomassie staining to visualize purified proteins. The stained gels were then sent for mass spectrometric analysis.

The interactome analysis was performed in two cell lines, the LuAD cell line HCC-44 and the embryonic kidney cell line HEK293T. HEK293T cells were chosen as they are a standard model system for protein expression and purification studies where large protein amounts are needed (Abaandou et al., 2021). Further, the competition assay, described in chapter 5.2.1, showed that DCAF13 depletion led to a dropout in HEK293T cells, similar to LuAD cells. This indicates that DCAF13 is also a vulnerability in HEK293T cells and is likely interacting with similar substrates, making the cell line an adequate model for this interactome analysis. HCC-44 cells were stably transduced with a lentiviral vector carrying the SF-DCAF13 construct or the SF-tag-expressing empty vector (EV), whereas HEK293T cells were transiently transfected with an SF-DCAF13 expression plasmid or the plasmid expressing the SF-tag alone (EV). The expression of the tagged DCAF13 protein was confirmed by immunoblotting prior to purification (Figure 32a), showing an evident overexpression of SF-DCAF13 compared to the endogenous protein. The purification method is described in detail in chapter 4.6.1. The purified proteins were separated by SDS-PAGE, stained by Coomassie, and sent for mass spectrometry analysis. Figure 32b shows the Coomassie-stained SDS-PAGE gels to visualize the purified proteins. The bait protein (SF-DCAF13) is enriched in all three replicates in both cell lines. Further, many proteins co-purified with the bait protein, evident by the additional bands in the SF-DCAF13 samples. Interestingly, the purification from HCC-44 cells appears cleaner than the purification from HEK293T cells, as there are fewer

bands in the EV samples compared to the SF-DCAF13 samples. This was also apparent from the volcano plots of the identified proteins depicted in figures 33a and b. Distinctly more proteins were enriched in the DCAF13 samples in the HCC-44 cell line than in HEK293T cells. 1169 proteins were identified in the purification from HCC-44 cells, with 776 being identified with high reproducibility (-log10(p-value) ≥ 1.3) and enrichment (log2FC ≥ 2). In contrast, only 964 overall and 282 significant proteins were identified in the HEK293T cells, supporting the impression from the Coomassie-stained gels that the purification from HCC-44 cells appeared cleaner.

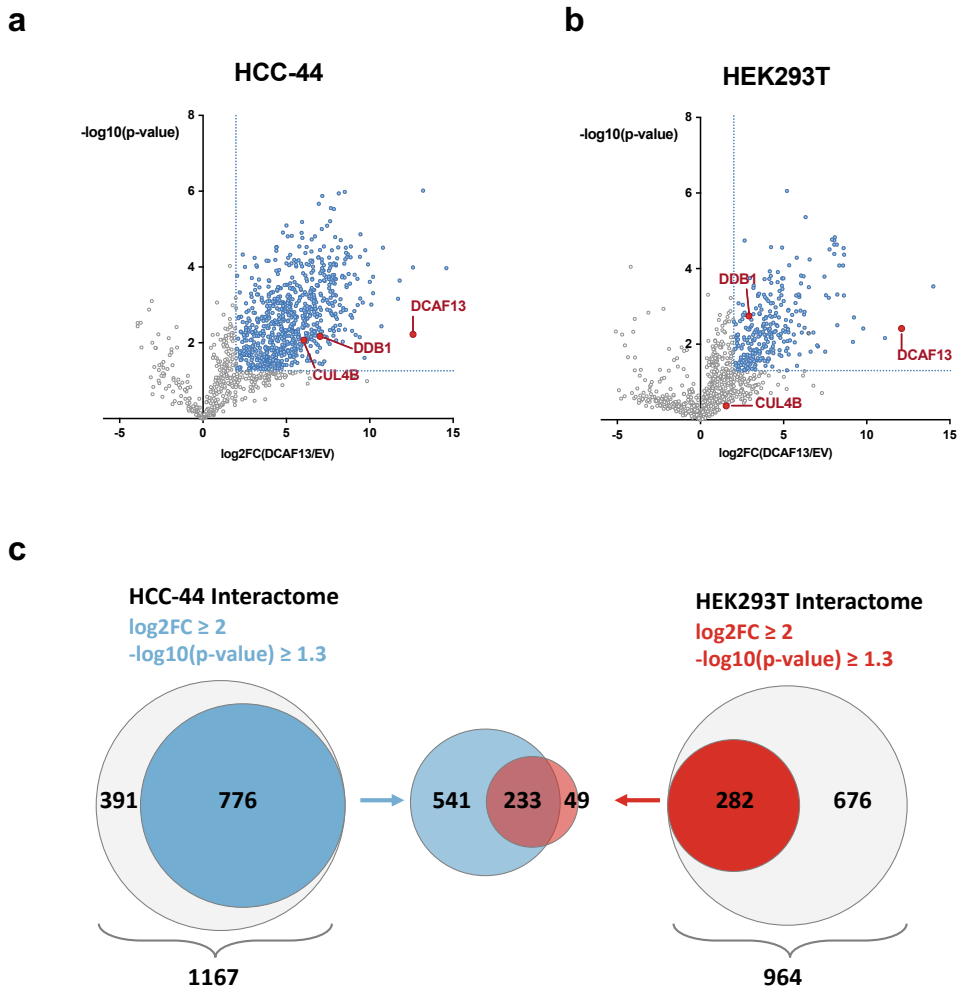

Figure 33: Analysis of interactome screening for DCAF13 substrates
Volcano plot of the mass spectrometric analysis of the DCAF13 interactome screen for HCC-44 (**a**) and HEK293T (**b**) cells. Log2 ratios of averaged DCAF13/EV LFQ (label-free quantification) values were plotted against negative log10 of the calculated p-value by Welsh's t-test. Significantly enriched proteins (log2FC ≥2 and -log10(p-value) ≥ 1.3) are marked in blue. Bait protein (DCAF13) and members of the CUL4 ubiquitin ligase complex (CUL4B, DDB1) are marked in red. (**c**) Visualization of the overlap of significantly enriched proteins from the DCAF13 interactome in HCC-44 and HEK293T cells. FC: Fold change; EV: empty vector. [MS data provided by BayBioMS@MRI core facility, Dr. P Giansanti]

An overlap of the significantly enriched proteins from both purifications (Figure 33c) revealed that almost all significantly enriched proteins from the HEK293T purification were also found in the HCC-44 purification. Moreover, while the expected binding partners of the ubiquitin

ligase complex CUL4B and DDB1 (highlighted in red) were identified in both datasets, CUL4B did not surpass the significance threshold in the purification from HEK293T cells. Consequently, further analyses were performed with the dataset generated from the HCC-44 cells. Focusing on the purification from LuAD cells also added the benefit of including potential lung-specific interactors. Surprisingly, the interactor CUL4A could not be found in the interactome, although its interaction with DCAF13 was previously observed in the FLAG-IP depicted in Figure 31. This might be due to a detection limit of the mass spectrometer, as discussed in chapter 6.4.1.

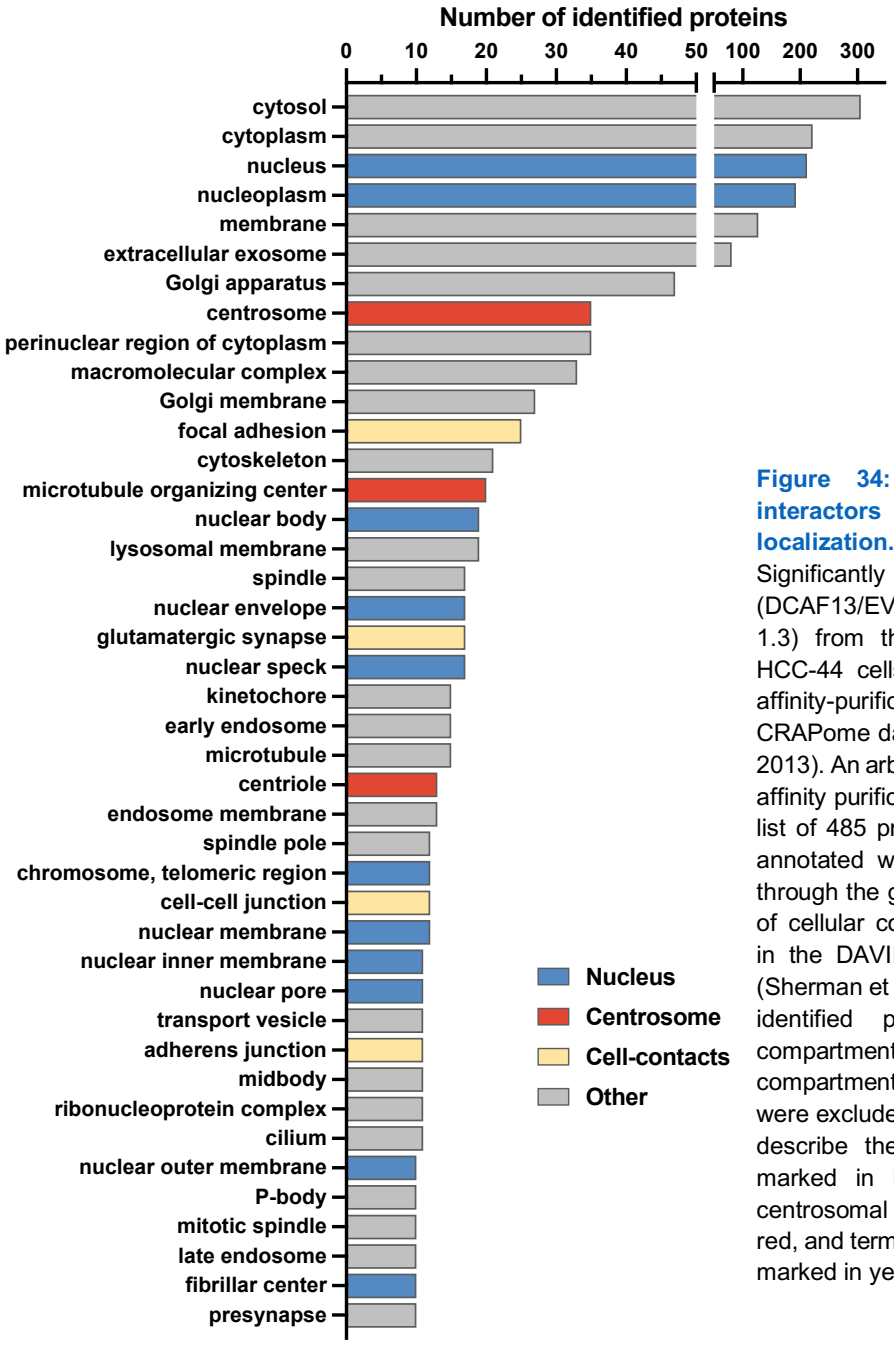

Figure 34: Clustering of DCAF13 interactors according to their cellular localization.
Significantly enriched proteins (log2FC (DCAF13/EV) ≥2 and -log10(p-value) ≥ 1.3) from the DCAF13 interactome in HCC-44 cells were filtered for common affinity-purification contaminants from the CRAPome database (Mellacheruvu et al., 2013). An arbitrary cutoff of 180/716 single affinity purifications was set, resulting in a list of 485 proteins. These proteins were annotated with their cellular localization through the gene ontology term collection of cellular compartments (GOTERM-CC) in the DAVID functional annotation tool (Sherman et al., 2022), and the number of identified proteins in each cellular compartment was counted. Cellular compartments with less than ten proteins were excluded from the graph. Terms that describe the nuclear compartment are marked in blue, terms describing the centrosomal compartment are marked in red, and terms describing cell contacts are marked in yellow.

To further narrow down the list of potential substrate candidates, the dataset was cross-validated with the data of common purification contaminants from the CRAPome database (Mellacheruvu et al., 2013). This approach was chosen to exclude common contaminants of affinity purifications and proteins that predominantly interact during protein biosynthesis of every overexpression construct, i.e., ribosomal proteins and chaperones, and therefore are presumably not relevant substrate candidates. For that purpose, the filter was set to proteins identified in less than 180 of 716 single affinity purifications deposited on the CRAPome database. This resulted in a list of 485 proteins. These proteins were further characterized and grouped by their annotated cellular compartment, using the DAVID functional annotation tool and the gene ontology term collection of cellular compartments (GOTERM-CC) (Sherman et al., 2022), as seen in figure 34. Interestingly, many identified proteins were annotated with localization to the nucleus (highlighted in blue), the centrosome or mTOC (highlighted in red) or cell-contacts (highlighted in yellow). This is in line with the localization of DCAF13 in LuAD cells, as observed in the immunofluorescence staining described in chapter 5.3. Strikingly, almost half of the identified and filtered proteins were annotated with nuclear localization (196 of 485), supporting the finding that DCAF13 predominantly localizes to the nucleus and might exert its most relevant function in that cellular compartment.

5.5.3 DiGLY proteomics identify the altered ubiquitome after DCAF13 depletion

A diGLY proteomics approach was chosen to identify potential ubiquitination substrates of DCAF13. This approach makes use of the fact that ubiquitin is covalently attached to lysine residues of the target protein via its C-terminus. Once the ubiquitinated protein is digested with trypsin, peptides are generated that have a glycine-glycine (diGLY) remnant attached to the priorly ubiquitinated lysine. An antibody that recognizes the diGLY motif is used to enrich previously ubiquitinated peptides by immunoprecipitation, which are then analyzed by mass spectrometry, as depicted in Figure 35a. Depleting the E3 ligase adapter DCAF13 from cells would therefore cause a reduction in the ubiquitination status of its substrates and lead to fewer ubiquitinated peptides being measured.

For this experiment, HCC-44 and NCI-H1437 cells were transduced with a control shRNA or shRNAs targeting DCAF13, as depicted in the schematic in Figure 35b. Samples were harvested 48 hours post-transduction and either subjected to diGLY enrichment or directly measured by mass spectrometry to analyze the reference proteome. An early time-point of 48 hours was chosen to reduce downstream ubiquitination events due to the observed apoptotic phenotype. Figure 35c shows the volcano plots of enriched or depleted peptides after DCAF13 knockdown compared to the control shRNA. For subsequent analyses, a cutoff for significantly less ubiquitinated peptides was employed (log2FC(shCTRL/shDCAF13) ≤ -0.5 and -log10(p-value) > 1.3), and respective peptides are marked in orange (shDCAF13_2 vs. shCTRL) or red (shDCAF13_3 vs. shCTRL). A pathway enrichment analysis on all significantly downregulated peptides per condition revealed an enrichment of proteins associated with programmed cell death and signaling of Rho GTPases, which are GTPases that are highly involved in actin cytoskeleton dynamics (Pellegrin & Mellor, 2007) (Figure 36, blue arrows). This further confirmed the observed phenotypic changes of actin cytoskeleton deregulation and apoptosis upon DCAF13 depletion described in the previous chapters.

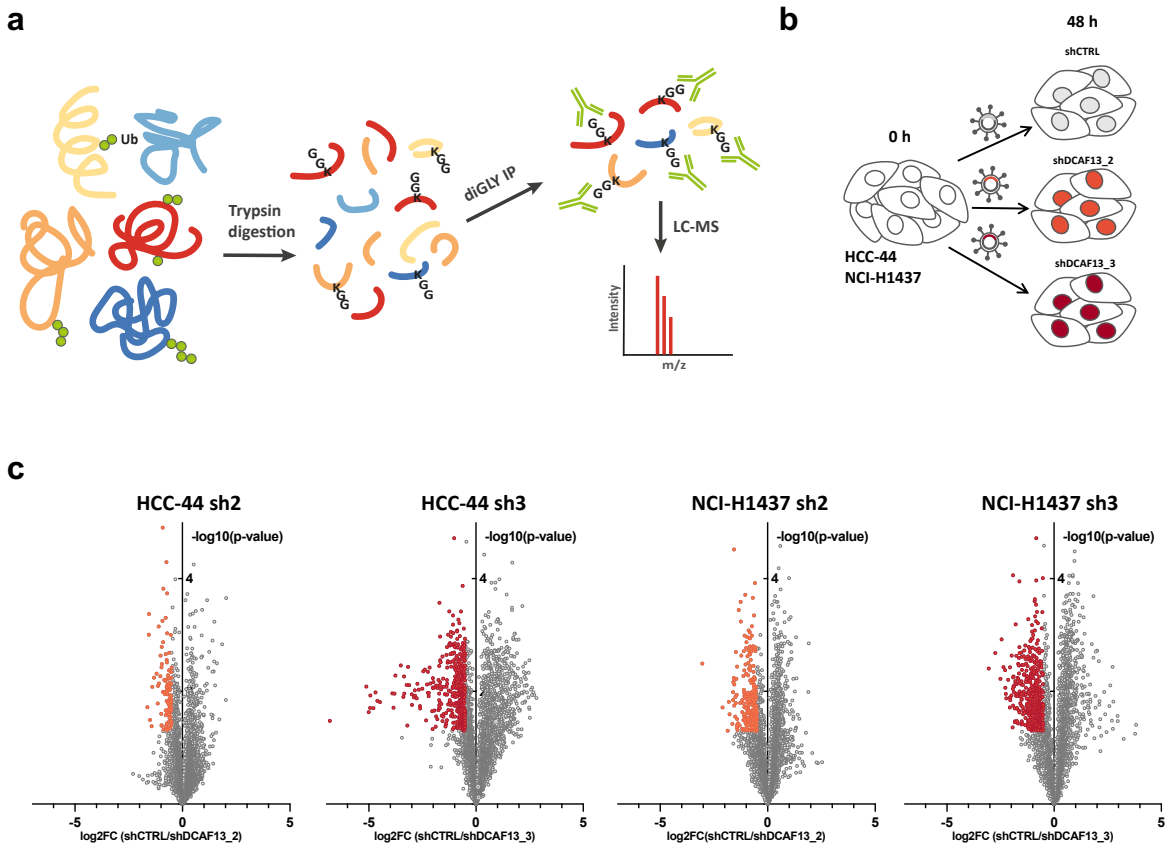

Figure 35: DiGLY proteomic analysis for the identification of DCAF13 ubiquitination substrates.
(**a**) Schematic representation of the diGLY enrichment method. Ub: ubiquitin (**b**) Schematic of the experimental setup for diGLY proteomics upon DCAF13 depletion. HCC-44 or NCI-H1437 were lentivirally transduced with a non-targeting shRNA (shCTRL) or shRNAs targeting DCAF13 (shDCAF13_2, shDCAF13_3) and harvested after 48 hours. Protein lysates were subjected to trypsin digestion and direct TMT labeling and mass spectrometric analysis (see figure 37) or diGLY enrichment and subsequent TMT labeling and mass spectrometric analysis. (**c**) volcano plots for alterations in ubiquitinated peptides in HCC-44 and NCI-H1437 cells upon DCAF13 depletion. Log2 transformed ratios of averaged shCTRL/shDCAF13 reporter intensities are plotted against negative Log10 transformed p-values calculated by Welsh's t-test. Significantly less ubiquitinated peptides (log2FC(shCTRL/shDCAF13) ≤ -0.5 and -log10(p-value) > 1.3) are indicated in orange (shCTRL vs shDCAF13_2) or red (shCTRL vs shDCAF13_3). [Data for (c) by Dr. Chien-Yun Lee] LC-MS : Liquid chromatography mass spectrometry

The diGLY mass spectrometric analysis was combined with the measurement of the reference proteome of the same samples (Figure 37). This was implemented to exclude that fewer ubiquitinated peptides of a protein were measured simply because the protein itself was less abundant and not because it was less ubiquitinated. In fact, if a protein has less degradative ubiquitination, such as the K48 chain type, then stabilization and enrichment of that protein could even be expected. However, since it has yet to be discovered if DCAF13 influences the turnover of its substrates through K48 ubiquitination, stabilization or enrichment of the potential substrate candidate cannot be assumed.

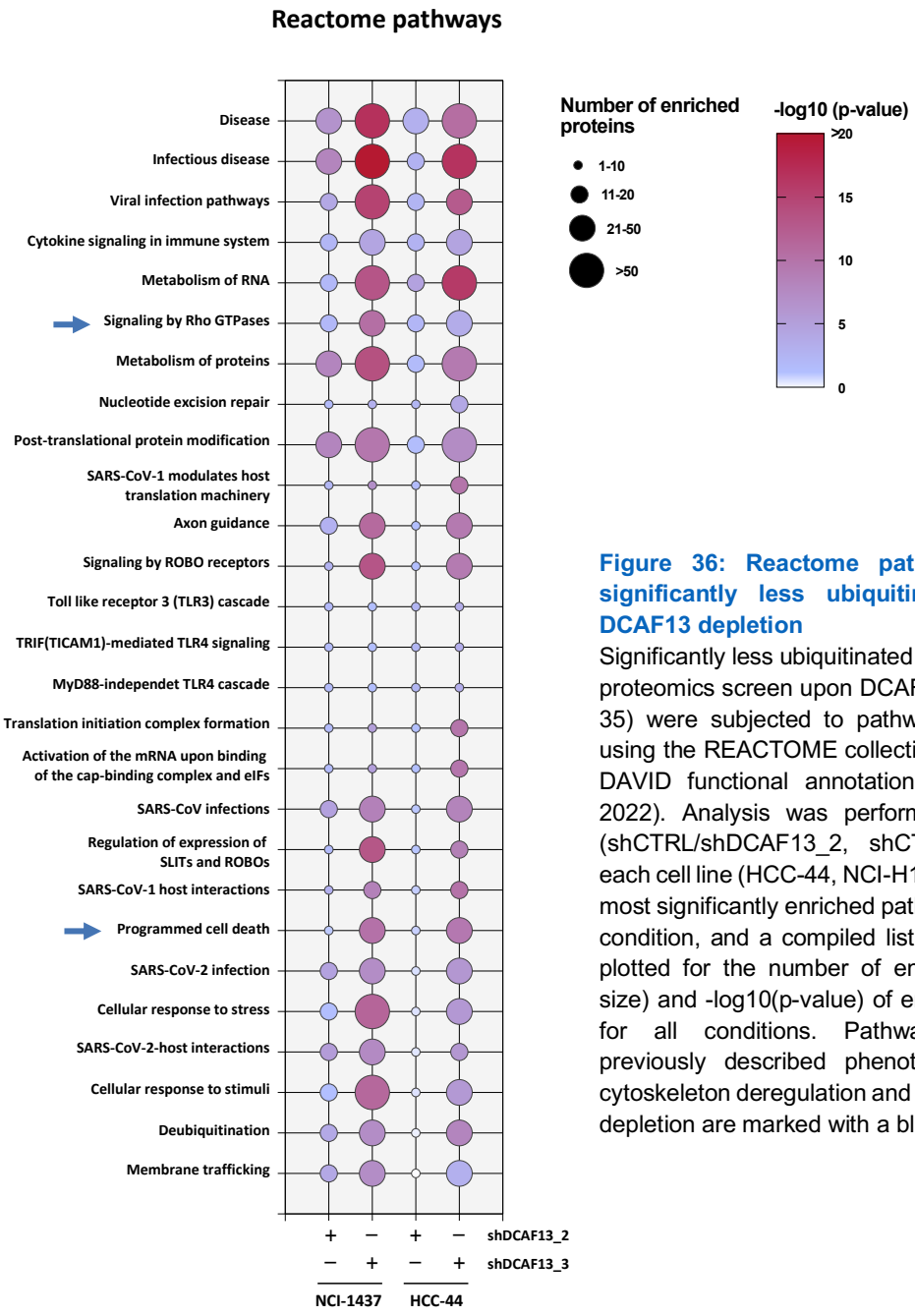

Figure 36: Reactome pathway enrichment for significantly less ubiquitinated peptides upon DCAF13 depletion

Significantly less ubiquitinated peptides from the diGLY proteomics screen upon DCAF13 depletion (see figure 35) were subjected to pathway enrichment analysis using the REACTOME collection of pathways from the DAVID functional annotation tool (Sherman et al., 2022). Analysis was performed for each condition (shCTRL/shDCAF13_2, shCTRL/shDCAF13_3) and each cell line (HCC-44, NCI-H1437) separately. The ten most significantly enriched pathways were selected per condition, and a compiled list of these pathways was plotted for the number of enriched proteins (bubble size) and -log10(p-value) of enrichment (bubble color) for all conditions. Pathways corroborating the previously described phenotypic changes of actin cytoskeleton deregulation and apoptosis upon DCAF13 depletion are marked with a blue arrow.

Figure 37a shows the volcano plots for each condition (shCTLR/shDCAF13_2, shCTRL/shDCAF13_3) and cell line and highlights how DCAF13 is significantly depleted in all samples. Additionally, the proteomic changes were also subjected to gene set enrichment analysis (GSEA), as previously described, and gene sets were filtered for association with the actin cytoskeleton (Figure 37, left) or apoptosis (Figure 37b, right). Consistent with the previously discussed phenotypic observations, the analysis showed a proteomic downregulation of gene sets involved in actin cytoskeleton regulation and upregulation of gene sets involved in apoptosis. This further confirmed that DCAF13 depletion induces actin cytoskeleton deregulation and apoptosis.

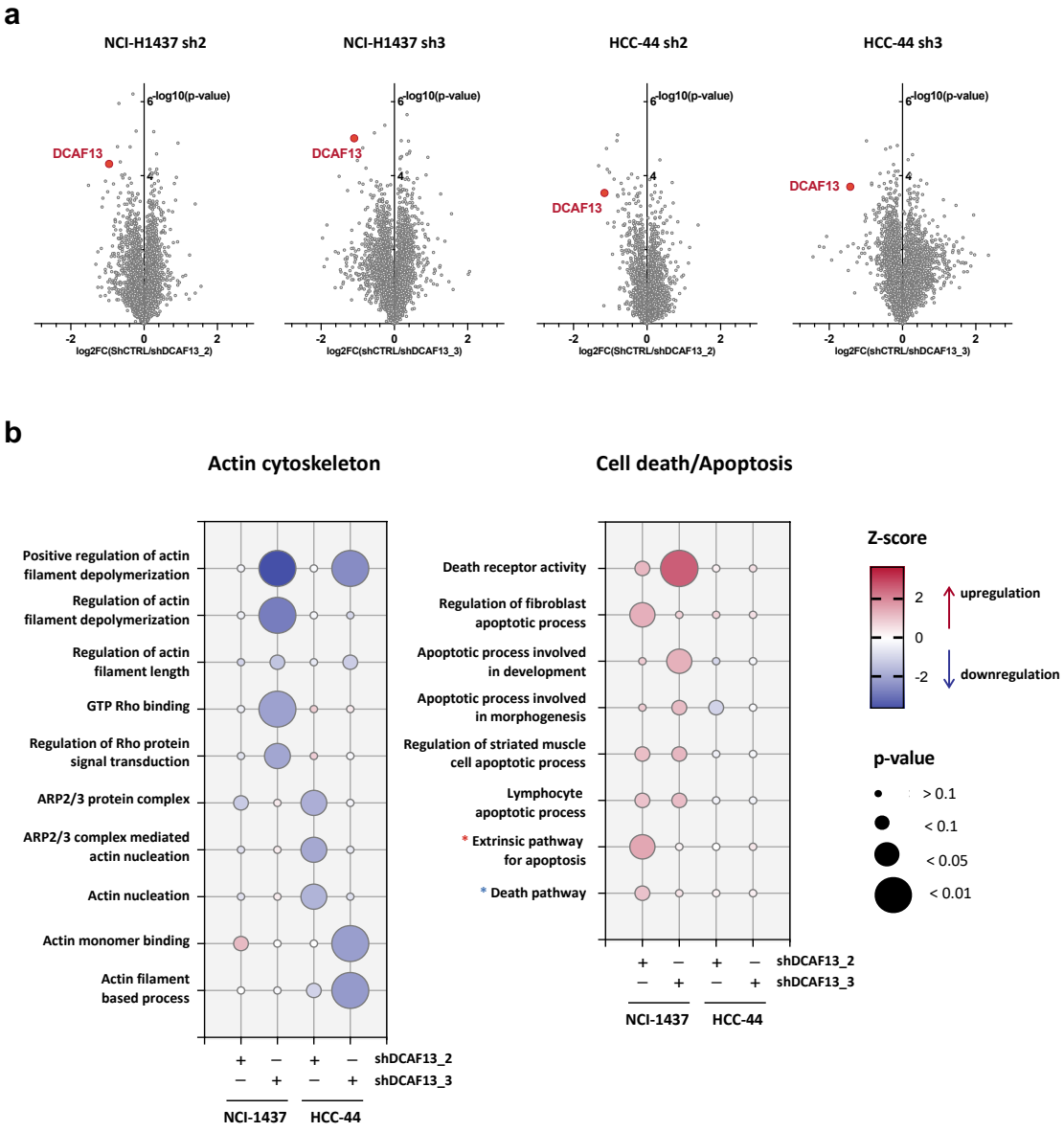

Figure 37: Analysis of proteomic changes upon DCAF13 depletion

HCC-44 or NCI-H1437 were lentivirally transduced with a non-targeting shRNA (shCTRL) or shRNAs targeting DCAF13 (shDCAF13_2, shDCAF13_3) and harvested after 48 hours. Protein lysates were subjected to trypsin digestion and either diGLY enrichment and subsequent TMT labeling and mass spectrometric analysis (see figure 35.) or direct TMT labeling and mass spectrometric analysis (**a**) volcano plots for alterations in protein abundance in HCC-44 and NCI-H1437 cells upon DCAF13 depletion. Log2 transformed ratios of averaged shCTRL/shDCAF13 reporter intensities are plotted against negative Log10 transformed p-values calculated by Welsh's t-test. Depletion of DCAF13 is indicated in red. (b) Gene set enrichment analysis (GSEA) was performed for the proteomic changes upon DCAF13 depletion. Gene sets (Hallmark, C2, C5) were downloaded from the Molecular Signatures Database (MSigDb). The analysis was performed separately for each DCAF13-targeting shRNA, compared to shCTRL, and each cell line. Gene sets associated with actin cytoskeleton regulation (left) and apoptosis or cell death (right) were isolated and plotted for changes in the individual conditions. The bubble size denotes the significance of the gene set alteration, and the bubble color represents a z-score, the -log10(p-value) multiplied by the direction of the alteration (up = 1, down =-1). Statistics were calculated using the edgeR framework (Y. Chen et al., 2016)and the glmQLFTest function. Gene sets with red asterisks are from the REACTOME pathway collection, blue asterisks represent the KEGG pathway collection, and gene sets without asterisks are from the GO-term collection [Data for (a) by Dr. Chien-Yun Lee, R-code for GSEA in (b) by Dr. P. Auf der Maur]

5.5.4 Cross-validation of the DCAF13 interactome and functional proteomics screens

To identify potential DCAF13 ubiquitination substrates, the two screens were intersected to identify proteins that co-purify with DCAF13 and are less ubiquitinated upon DCAF13 depletion. The Venn diagram of the cross-validation is depicted in figure 38a. Overlap of significantly enriched proteins from the interactome in HCC-44 cells (Chapter 5.5.2) and proteins with less ubiquitinated peptides from the diGLY proteomics screening in either HCC-44 or NCI-H1437 cells (Chapter 5.5.3) yielded 117 potential substrate candidates. The dataset obtained from NCI-H1437 cells was included in the cross-validation approach to increase the pool of potential substrates.

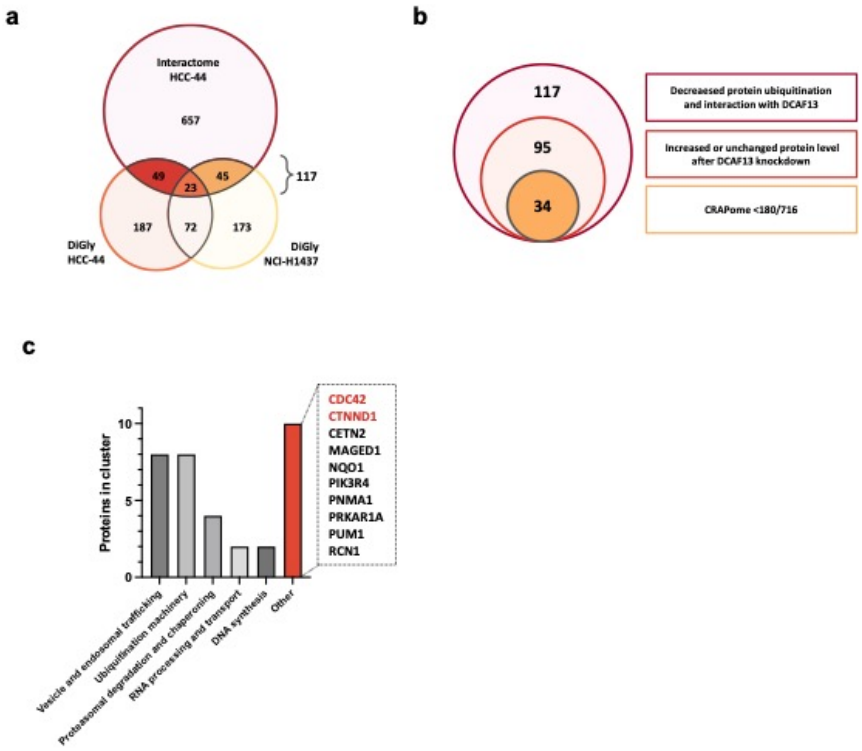

Figure 38: Cross-validation of mass-spectrometry-based screens for DCAF13 substrate candidates
Venn diagram of i) proteins significantly enriched in the DCAF13 interactome in HCC-44 cells (Figure 33), and proteins with at least one peptide significantly less ubiquitinated upon DCAF13 depletion in the diGLY proteomics screen in at least one comparison of shDCAF13 to shCTRL in ii) HCC-44 cells (Figure 35) and iii) NCI-H1437 cells (Figure 35). The overlap of less ubiquitinated proteins from either cell line with the DCAF13-interacting proteins yielded 117 candidates. (b) The 117 candidates were further narrowed down by integrating information on protein levels after DCAF13 depletion from the proteomics screen. A log2(FC) ≥ - 0.1 was set as cutoff for the average of shCTRL/shDCAF13_2 and shCTRL/shDCAF13_3 in the respective cell line with the significantly altered ubiquitinated peptide. Proteins with significantly altered peptides but without information about the protein levels were also included. This list of 95 proteins was further narrowed down by integrating information about common contaminants of affinity purifications from the CRAPome database (Mellacheruvu et al., 2013). An arbitrary cutoff of 180/716 deposited single-affinity screens was used to exclude unspecific binding partners, yielding 34 potential substrate candidates. (c) Functional clustering of the 34 substrate candidates based on the DAVID functional annotation tool (Sherman et al., 2022) or literature research. Proteins involved in actin cytoskeleton regulation are marked in red.

These 117 proteins were further reduced by integrating information on the total protein levels of less ubiquitinated proteins to exclude the occurrence of false positives, as previously described. This yielded 95 proteins, many of which were excluded as potential contaminants due to cross-validation with the affinity purification contaminant repository CRAPome (Mellacheruvu et al., 2013), resulting in 34 potential substrate candidates (Figure 38b). These candidates were subjected to functional annotation clustering through the DAVID functional annotation tool (Sherman et al., 2022) and literature research (Figure 38c).

The candidates primarily clustered into proteins involved in endosomal trafficking or the ubiquitination and proteasome machinery. Ten proteins could not be clustered into common cellular pathways. Interestingly, two out of those proteins, cell division control protein 42 homolog (CDC42) and catenin delta-1 (CTNND1), are involved in the regulation of actin cytoskeleton organization, making them attractive ubiquitination substrate candidates for DCAF13. CDC42 is a small GTPase belonging to the Rho GTPases family that governs the formation of cellular actin structures (Nobes & Hall, 1995; Tapon & Hall, 1997). CDC42 activity has been closely linked to ARP2/3-mediated actin polymerization (Bogucka-Janczi et al., 2023), and elevated CDC42 activity was shown to prevent actin fiber formation (Landspersky et al., 2022). CTNND1, also known as p120, is a regulator of cadherin-mediated cell adhesion (Ishiyama et al., 2010). It was further shown to translocate to the nucleus and associate with transcription factors (Daniel, 2007). Of note, recent studies have shown that CTNND1 can activate CDC42 and thereby regulate actin cytoskeleton dynamics (W. W. Liu et al., 2021). CDC42 and CTNND1, thus, presented promising substrate candidates, as both are involved in actin cytoskeleton organization and could potentially explain the observed phenotype of actin cytoskeleton deregulation upon DCAF13 depletion.

5.5.5 Validation of CDC42 and CTNND1 as potential DCAF13 substrate candidates

To evaluate if CDC42 and CTNND1 could indeed be ubiquitination substrates of DCAF13, we first sought to replicate the interaction with DCAF13. To this end, semi-endogenous IPs with overexpressed SF-tagged DCAF13 were performed in HCC-44 (Figure 39a) and HEK293T (Figure 39b) cells. Immunoblotting of the IP samples revealed a moderate binding of CDC42 and CTNND1 to DCAF13 but not to the EV control in HCC-44 cells. Of note, both proteins presented with multiple bands on immunoblotting. A second band above the expected protein size was detected for CDC42, indicating posttranslational modification, such as phosphorylation. CTNND1 presented with several bands below the predicted protein size of 109 kDa of its largest and canonical isoform, indicating that its more than 30 other isoforms might also be of relevance. Interestingly, the interaction of the two proteins with DCAF13 could not be observed in HEK293T. This closely replicated the data obtained from the DCAF13 interactome in HEK293T cells, where both CDC42 and CTNND1 were identified but did not meet the significance threshold described in chapter 5.5.2, hinting at a potential context-dependent interaction of CDC42 and CTNND1 with DCAF13 in LuAD cells.

To further test whether the ubiquitination of CDC42 and CTNND1 was altered by DCAF13, an *in-vivo*-ubiquitination assay was performed. To this end, HEK293T cells were transfected with a non-targeting siRNA or siRNA targeting DCAF13 (siDCAF13) to deplete DCAF13. Next, the cells were transfected with HA-tagged ubiquitin and either FLAG-tagged CDC42 or CTNND1. After 24 hours, cells were treated with the proteasome inhibitor MG132

to allow for the accumulation of ubiquitinated substrates that would otherwise be degraded by the proteasome. Cell lysates were subjected to FLAG-IP under denaturing conditions to exclude co-purification of interaction partners and subsequently analyzed by immunoblotting. The immunoblotting analysis of the assay for CDC42 is depicted in Figure 39c. The characteristic laddering and high-molecular-weight smear could be observed in the segment blotted for HA-tagged ubiquitin after the FLAG-IP for samples containing FLAG-tagged CDC42. The laddering started above the predicted and observed size of 21 kDa of CDC42, indicating that CDC42 is indeed polyubiquitinated. However, the depletion of DCAF13 did not alter the band pattern or the intensity of the HA-ubiquitin signal, indicating that DCAF13 does not alter CDC42 ubiquitination. The same effect was observed for CTNND1, as depicted in Figure 39d. Of note, the signal for the FLAG-tagged CTNND1 and HA-ubiquitin after FLAG-IP appeared to create a band pattern and smear below the expected size of the overexpression construct of roughly 110 kDa. This could indicate that the plasmid construct or the protein was degraded during the experiment and that it should therefore be repeated. In conclusion, while the interaction of DCAF13 with CDC42 and CTNND1 was demonstrated in LuAD cells, an interaction or altered ubiquitination could not be observed in the context of HEK293T cells. Whether DCAF13 can alter the ubiquitination of CDC42 and CTNND1 in the context of LuAD needs to be investigated further.

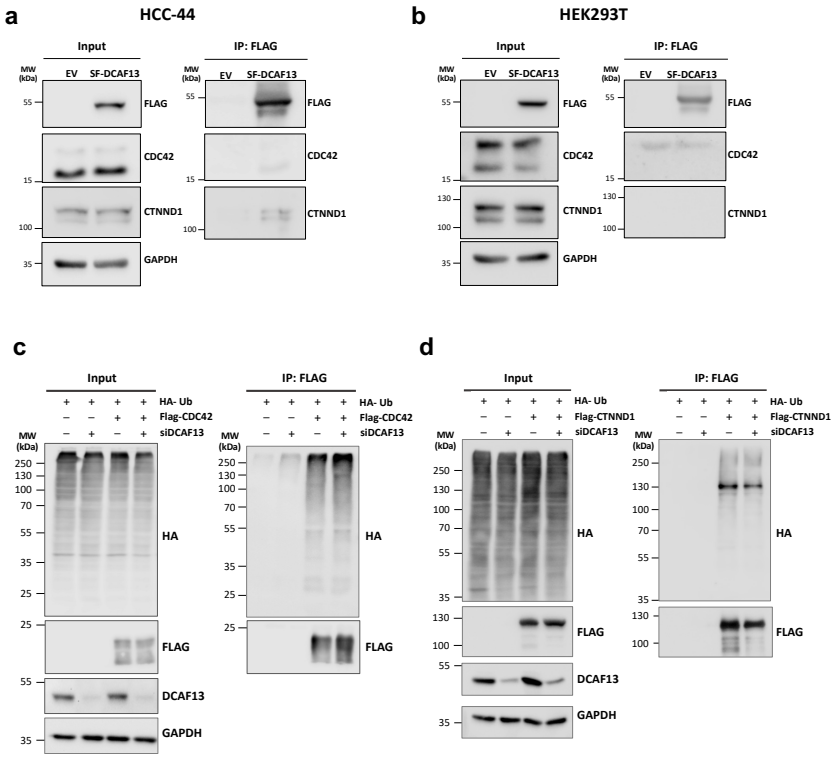

Figure 39: DCAF13 depletion does not alter ubiquitination status of CDC42 and CTNND1
The binding of CDC42 and CTNND1 to DCAF13 was analyzed by semi-endogenous immunoprecipitation (IP) with overexpressed SF-tagged DCAF13 and subsequent FLAG-IP in (**a**) HCC-44 and (**b**) HEK293T cells. Ubiquitination of CDC42 (**c**) and CTNND1 (**d**) upon DCAF13 depletion was assessed using an *in-vivo*-ubiquitination assay. HEK293T cells were transfected with a non-targeting siRNA or siRNAs targeting DCAF13 (siDCAF13) to induce DCAF13 depletion. Cells were additionally transfected with the indicated plasmids encoding Ha-ubiquitin (HA-Ub) or FLAG-tagged CDC42 or CTNND1. 24 hours after transfection, cells were treated with 10 µM MG132 for 3 hours prior to harvest. Cell lysates were subjected to FLAG-IP under denaturing conditions, and immunoblot analysis with the indicated antibodies was performed subsequently.

6 Discussion

6.1 A CRISPR/Cas9-based vulnerability screen identifies DCAF13 as a dependency

CRISPR/Cas9-based genome-wide cancer dependency screening was first established in 2014, and since then, it has been widely used as a tool across the spectrum of cancer entities (Meyers et al., 2017; Shalem et al., 2014). Pooled CRISPR dropout screens are primarily based on the competition principle, and sgRNA libraries targeting the whole genome often only reveal the strongest oncogenes and common cell-essential genes, which are either well-studied or unsuitable therapeutic targets. Due to the pooled approach, the effect of less prominent but interesting dependencies is often masked. Thus, smaller and focused libraries hold the potential to identify dependencies in specific pathways or groups of genes, as for example for kinases and proteins involved in DNA damage repair (Mengwasser et al., 2019; Slivka et al., 2019). For this project, we used a previously published (Xu et al., 2021) targeted sgRNA library to identify LuAD vulnerabilities within the ubiquitin system and identified the E3 ubiquitin ligase adapter *DCAF13* as one of the most potent dependencies (Figure 11). At the same time, the screen recapitulated the essentiality of well-known oncogenes and therapeutic targets of LuAD, such as E3-ubiquitin-protein ligase UHRF1 (*UHRF1*) (Sidhu & Capalash, 2017), emphasizing the experiment's validity.

The knockout of *DCAF13* led to a similarly potent depletion in genome-wide dependency screens performed by Aguirre *et al*. The authors performed CRISPR/Cas9 dropout screens in 33 cancer cell lines representing various cancer entities. *DCAF13* was defined as a dependency in 31 out of 33 cell lines, consistently ranking in the top depleted genes, with the most potent depletion showing in the melanoma cell line A-375 with a rank of 119 out of 17627. Of note, *DCAF13* also ranked in the top 500 out of 17627 genes in all four LuAD cell lines included in the screen. Cell line HCC-44, which was also part of the CRISPR dropout screen with the targeted ubiquitin library, as presented in chapter 5.1, ranked *DCAF13* at position 331 in the study by Aguierre *et al.,* indicating that a dependency observed in a targeted-library approach can also be replicated by whole-genome screening (Aguirre et al., 2016). Furthermore, as the screen performed by Aguirre *et al*. included cell lines from many other entities, such as melanoma, colorectal cancer, pancreatic cancer, and sarcoma, this would imply that the *DCAF13* dependency is not limited to the lung cancer context (Aguirre et al., 2016). Indeed, several publications have described *DCAF13* as an oncogene in breast cancer (J. Liu et al., 2020; Shan et al., 2022; Z. Sun et al., 2022), colorectal cancer (Y. Sun et al., 2023), hepatocellular carcinoma (Cao et al., 2017), or osteosarcoma (B. Chen et al., 2019; Z. Chen et al., 2018) and a very recent publication also confirmed its oncogenic role in LuAD (Wei et al., 2023). Moreover, Wei *et al*. demonstrated that *DCAF13* is overexpressed in tumor tissue compared to normal tissue in a plethora of cancer entities, further emphasizing that *DCAF13* acts as a pan-cancer oncogene (Wei et al., 2023). Notably, these observations are only based on transcriptomic data. As a factor in posttranslational modification, the expression of DCAF13, and other components of the ubiquitin system, would be more informative on the protein level. However, large-scale datasets with protein expression in tumor and normal tissue are still missing. Nevertheless, as presented in the previous chapters, shRNA-mediated

competition assays in lung fibroblast cells (Figure 18) also revealed that DCAF13 depletion led to a delayed growth disadvantage in comparison to LuAD cells, indicating that normal cells might not be as dependent on DCAF13 function as cancerous cells and implying a potential therapeutic window for DCAF13-targeting therapy. However, as described in chapter 2.1.2, LuAD is a tumor that arises from glandular epithelial cells. Thus, to confirm that normal lung tissue is not as dependent on DCAF13 as cancerous tissue, the experiments should be repeated in non-cancerous cells of epithelial origin, such as primary small airway epithelial cells (HSAEC).

An oncogene-dependent genome-wide CRISPR screen performed by Vichas *et al.* with isogenic cell lines, derived from LuAD cell line PC-9, harboring an activating mutation in the *KRAS* or *EGFR* gene classified *DCAF13* as a dependency (Vichas et al., 2021). This further implies that *DCAF13* is a vulnerability in LuAD cells regardless of the activation of common oncogenes. This is further supported by the data generated by the CRISPR screen in this study, where *DCAF13* was identified as a dependency in cell lines with a $KRAS^{WT}$ (NCI-H1437) and $KRAS^{G12C}$ (HCC-44, NCI-H23) genetic background (Figure 11). Furthermore, knockdown-based competition assays in various LuAD cell lines (Figure 18) with *EGFR* mutation (NCI-H1975, NCI-H1650, HCC827), *ALK* translocation (NCI-H2228), *NRAS* and *BRAF* mutation (NCI-H2087), or *KRAS* mutation (NCI-H23, HCC-44, A549) confirmed this observation, as DCAF13 depletion consistently led to a growth disadvantage. Moreover, a genome-wide CRISPR/Cas9 screen performed by Feng *et al*. in isogenic cell lines derived from HEK293A cells, with loss of function of common tumor suppressors, such as *TP53* and *PTEN*, revealed that *DCAF13* still ranked as dependency regardless of tumor-suppressor presence. These findings are particularly fascinating in the context of patients with LuAD, where tumors are defined by significant heterogeneity of oncogenic drivers and additional co-mutations. A dependency such as *DCAF13*, which could be targeted irrespective of the patient's genetic background, would be particularly valuable.

For time reasons, the scope of this study could not include validation of *DCAF13* as a dependency of LuAD in an *in vivo* mouse tumor model. However, it is critical to investigate whether DCAF13 inhibition can decrease or abrogate tumorigenesis in preclinical tumor models before suggesting DCAF13 as a therapeutic target in patients. A recent study of DCAF13 in LuAD showed that DCAF13 depletion decreased tumor growth in an *in vivo* xenograft model (Wei et al., 2023), and the same effect was also observed in the context of breast cancer (Shan et al., 2022), indicating that DCAF13 is also a valid target *in vivo* and in different cancer entities. Collectively, the results presented in this study and recent publications nominate *DCAF13* as an oncogene in LuAD and as pan-cancer vulnerability, irrespective of the genetic background, with the potential for the development of targeted therapy.

6.2 DCAF13 depletion leads to loss of actin stress fibers and induction of apoptosis

In this study, *DCAF13* was identified as a dependency in a pooled CRISPR/Cas9-based screen, as sgRNAs targeting *DCAF13* dropped out of the cell pool over time. This indicated that DCAF13 depletion induced a growth disadvantage, confirmed by competition assays and cell counting (Figure 16,18,19). This aligns with several publications that report a growth

disadvantage of DCAF13-depleted cells in breast cancer (Shan et al., 2022) or LuAD (Wei et al., 2023). Mechanistic studies revealed only modest effects on the cell cycle (Figure 20), but a potent and significant increase of dead cells upon DCAF13 depletion was observed (Figure 21). Accordingly, cell death was identified as the central mechanism leading to the dropout of the cells in LuAD. Interestingly, studies in breast cancer have reported a modest increase in cell death upon DCAF13 depletion (Shan et al., 2022). However, the authors also observed prominent cell cycle arrest in the G1-phase. They concluded that this was the most dominant mechanism of growth arrest in DCAF13-depleted cells, indicating that there might be differences between the specific function of DCAF13 in LuAD and breast cancer cells.

In this study, inhibition of specific cell death pathways revealed that DCAF13 depletion induces caspase dependent apoptosis (Figure 22, 23). Investigation of the mitochondrial membrane potential of these cells further unveiled that apoptosis is induced through the intrinsic pathway, which is characterized by dysfunctional mitochondrial membrane potential (Figure 24). To our knowledge, this is the first account of DCAF13 depletion inducing apoptosis through the intrinsic pathway. The intrinsic pathway of apoptosis can be activated through different mechanisms, such as genotoxic stress or ER stress. Currently, it is still unclear why DCAF13 depletion results in the activation of this pathway. Future experiments should focus on identifying cellular components of the intrinsic apoptosis pathway that are activated upon DCAF13 depletion. To this end, mechanistic loss of function studies could be employed, where individual genes of the apoptosis cascade, such as *PUMA* or *NOXA*, are knocked out to see if apoptosis is still induced upon DCAF13 depletion. For instance, studies have shown that PUMA and NOXA both induce mitochondrial outer membrane permeabilization (MOMP) during apoptosis but are activated through different stress stimuli (Roufayel et al., 2022; J. Wang et al., 2021). Identifying which of these proteins is activated upon DCAF13 depletion could therefore elucidate which stimulus is needed for apoptosis induction. Special interest could also be taken towards proteins of the apoptosis cascade that are known to be ubiquitinated and degraded by the proteasome, such as SMAC (J. Bin Kim et al., 2013) or BCL-2 family members (Benard et al., 2010). Performing loss of function studies of downstream players of apoptosis could further help to exclude that other cell death pathways are induced in parallel to or as a consequence of apoptosis. Wang et al. showed that pyroptosis could be induced through gasdermin E (GSDME) cleavage by activated caspase 3 (Y. Wang et al., 2017). Knockout of gasdermin E in addition to depletion of DCAF13 could reveal if pyroptosis occurs in addition to apoptosis.

Mechanistically, we find that depletion of DCAF13 results in downregulation of the actin nucleation pathway (Figure 28) and similarly to the abrogation of actin stress fiber formation (Figure 29), which has not been attributed to DCAF13 previously. As the loss of actin stress fibers was independent of caspase activation (Figure 30), the question remains whether actin cytoskeleton deregulation could initiate apoptosis upon depletion of DCAF13. Interestingly, several studies have reported a link between cytoskeletal dynamics and apoptosis. Thymosin β, a protein that sequesters G-actin and prevents actin polymerization, was found to sensitize ovarian cancer cells and fibroblasts to apoptosis by disrupting stress fiber formation (Hall, 1995; Rho et al., 2004). A potential mechanism behind this could be the release of actin-bound proteins during the disruption of stress fibers. For example, BH3-only protein BMF was found to associate with F-actin networks under physiological conditions, and loss of F-actin structures

led to dissociation and translocation of BMF to the mitochondria where it instigated MOMP and apoptosis (Grespi et al., 2010; Puthalakath et al., 2001). The apoptotic induction by actin depolymerization agents, such as cytochalasin D, likely relies on the same effect of BMF release from actin structures (Martin & Leder, 2001). Cofilin family proteins are additional connecting elements between the actin cytoskeleton and apoptosis. Cofilins are known for their role in actin disassembly, and dephosphorylated cofilins were found to translocate to the mitochondria and induce the apoptotic cascade through the release of cytochrome c (Chua et al., 2003; Klamt et al., 2009). Notably, cofilin depletion was sufficient to repress apoptosis (Chua et al., 2003) and could thus be studied in the context of apoptosis induction upon DCAF13 depletion. Moreover, cofilin-mediated depolymerization of F-actin promotes translocation and activation of the tumor suppressor p53, a well-known inducer of the intrinsic apoptosis pathway (T. Liu et al., 2017). It is conceivable that DCAF13 influences any of these pathways, and further studies are needed to elucidate which of these mechanisms could take place upon DCAF13 depletion. The apoptotic induction by actin-depolymerizing agents could imply that the loss of F-actin stress fibers upon DCAF13 depletion is sufficient to drive apoptosis. However, further studies are required to conclusively evaluate whether these two phenotypic changes occur consecutively or independently in parallel.

The reduction of actin stress fiber formation and enhanced apoptosis upon depletion of DCAF13 could also explain why *DCAF13* levels are high in cancerous tissue. As loss of DCAF13 induces apoptosis, it is conceivable that higher levels of DCAF13 make cancer cells less susceptible to apoptosis induction, which is a well-established hallmark of cancer (Hanahan & Weinberg, 2000). Further, defects in actin fiber formation in DCAF13-depleted cells could imply that DCAF13 functions as a regulator of actin fiber formation under physiological conditions. Actin remodeling is strongly associated with carcinogenesis, particularly with metastasis and epithelial-to-mesenchymal transition (EMT). For instance, Rho GTPases were shown to reorganize actin filaments and induce filopodia formation, which led to EMT in squamous cell carcinoma (Argenzio et al., 2018; Iwai et al., 2010). Of note, several publications have implicated the role of DCAF13 in promoting migration in breast cancer (J. Liu et al., 2020; Shan et al., 2022; Z. Sun et al., 2022). In particular, the report by Liu *et al.* showed that DCAF13 depletion reduced and DCAF13 overexpression increased breast cancer cell migration (J. Liu et al., 2020). In contrast, a reduction of LuAD cell migration upon DCAF13 depletion, using a wound healing assay, could not be observed in this study (data not shown). However, this could be explained by the potent and early induction of apoptosis upon DCAF13 depletion, making the execution of the wound healing assay technically challenging. Instead, it would be worthwhile to investigate the effects of DCAF13 overexpression on LuAD cell migration and to analyze the impact of actin cytoskeleton organization in that context. Together, these mechanisms could illustrate a function of DCAF13 during carcinogenesis and potentially explain the increased cancer aggressiveness observed in LuAD patients with high levels of *DCAF13* (Figure 13). However, further mechanistic studies are needed to elucidate if increased *DCAF13* expression is sufficient to drive carcinogenesis in LuAD and other cancer entities and in what way regulation of the actin cytoskeleton and apoptosis inhibition are involved.

6.3 DCAF13 localizes to the nucleus, the centrosome and cell contacts

In this study, endogenous DCAF13 was shown to primarily localize to the nucleus in LuAD cells. This study also marks the first report to show that DCAF13 additionally localizes to centrosomal structures and cell-to-cell contacts in LuAD cells (Figure 26). It is conceivable that the localization of DCAF13 is also closely tied to its molecular function or association with specific proteins or ubiquitination substrates. While it is likely that the localization of DCAF13 at the centrosome and the cell contacts is associated with its effects on actin cytoskeleton dynamics, further experiments are needed to delineate the function of DCAF13 in these particular cellular compartments.

SF-tagged and overexpressed DCAF13 seemingly only localized to the nucleus (Figure 25). This could be an artifact of imaging, as the exposure during confocal microscopy of the fluorescent staining needed to be decreased for conditions with DCAF13 overexpression. It is possible that the overexpressed DCAF13 also localized to the centrosome or cell contacts, but the presence could not be seen due to a reduction of laser intensity. Alternatively, it is conceivable that the SF-tag attached to the N-terminus of DCAF13 affects its subcellular localization. It has been shown that adding a tag to a protein can alter its molecular properties, including its subcellular localization (Margolin, 2012). It is conceivable that this happens through the masking of a potential nuclear localization signal (NLS) by the secondary structure of the tag or steric hindrance of the binding of proteins that arrange its localization, such as nuclear import factors. However, DCAF13 possesses an NLS at its C-terminus, as predicted by the NLS prediction tool NLStradamus (Nguyen Ba et al., 2009). Therefore, it is unlikely that the NLS is masked by an N-terminally attached small tag like the SF-tag. However, it cannot be excluded that other localization signals or sites for interaction partners are occluded by the tag, altering its physiological subcellular localization. Nevertheless, the observation of the endogenous staining of DCAF13 in the nucleus, at the centrosome, and cell-to-cell contacts is supported by data obtained from the interactome study in LuAD cells, where DCAF13-interacting proteins were enriched for nuclear, centrosomal, and cell contact localization (Figure 34). The enrichment of these proteins could also be an accompanying effect of the technical execution of the interactome experiment, as proteins are not limited to their physiological compartment and can interact freely during the FLAG-IP of the tagged DCAF13. Thus, even though SF-tagged DCAF13 might not have been located at the centrosome or cell contacts in HCC-44 cells, cell lysis could have led to physiological and false-positive interaction partners associating with DCAF13 during the incubation with the anti-FLAG-resin.

Interestingly, a publication has reported Dcaf13 to localize to nucleoli in mouse oocytes and mammalian HeLa cells (J. Zhang et al., 2019). In that study, Dcaf13 was N-terminally tagged with a GFP and localized primarily to the nucleoli and the rest of the nuclear structure. Distinct nucleolar localization of DCAF13 was never observed during the study presented in this thesis, and it is conceivable that adding a large tag, such as the 28 kDa protein GPF, significantly alters the localization of the tagged protein. A second publication by the same senior author also showed nucleolar localization of Dcaf13 in mouse oocytes and HeLa cells, and here the staining was validated with siRNA-based knockdown of Dcaf13 (Y. Zhang et al., 2018). It is conceivable that DCAF13 localization and its molecular function depend on its

cellular context and that it differs between species. Further studies are needed to determine if nucleolar localization of DCAF13 can also be observed in human oocytes and other contexts and if the localization to the centrosomes and cell contacts in LuAD cells reported in this study can be replicated in other cellular models as well.

6.4 Ubiquitination substrates of DCAF13

6.4.1 Screening approach for the identification of DAF13 ubiquitination substrates

DCAF13 is a predicted substrate recognition adapter for CUL4 ligases, and it was shown to interact with DDB1 and CUL4A in a co-immunoprecipitation (co-IP) in LuAD and HEK293T cells in this study (Figure 31). Therefore, DCAF13 likely contributes to and functions as an active E3 ubiquitin ligase, yet definitive proof is missing. Enzymatic activity can often be tested *in vitro*, as described for deubiquitinating enzymes and activity-based labeling with a suicide probe (Skelly & Spoel, 2021). However, since E3 ubiquitin ligase activity is highly selective towards the designated substrate (Metzger et al., 2012), *in-vitro*-ubiquitination assays to determine if $CRL4^{DCAF13}$ indeed functions as an E3 ubiquitin ligase is only feasible once the designated substrate is discovered.

In an effort to identify DCAF13 ubiquitination substrates in LuAD cells, a two-fold screening approach was employed in this study. Firstly, a DCAF13 interactome was defined through affinity-based purification of DCAF13 and subsequent mass spectrometric analysis of its binding partners (Figure 33). Secondly, ubiquitin-specific functional proteome studies, in the form of diGLY proteomics, and general proteomics were employed to identify proteins less ubiquitinated upon DCAF13 depletion in LuAD cells (Figure 35). Cross-validation of these two approaches and subsequent filtering for common contaminants of affinity purifications yielded 34 potential candidates (Figure 38). However, a large proportion of these candidates was not evaluated further, either since their molecular function did not fit the observed phenotype upon DCAF13 depletion or as their localization in subcellular compartments, such as the Golgi apparatus or the mitochondria, would make a physiological interaction with DCAF13 unlikely. Only two of the 34 candidates were deemed relevant enough to evaluate further, which poses the question of whether the screening and cross-validation approaches presented in this study were suitable for identifying ubiquitination substrates.

In this study, an affinity-based purification of DCAF13 interaction partners was performed using the widely employed method of FLAG-IP. As discussed, a pitfall of the FLAG-IP is the loss of the physiological context of the protein-protein interaction. As DCAF13 binds to the anti-FLAG-resin in a cell lysate, subcellular compartmentalization is lost. Therefore, proteins can interact that would not be able to interact *in vivo*, generating false-positive interaction partners. This could explain the identification of proteins localizing to the Golgi apparatus or the mitochondria, where DCAF13 was neither observed in this study nor reported to reside in the literature. Further, another substrate adapter of the CUL4 family, DCAF2, was reported to only convey binding and ubiquitination of its substrate CDT2 in complexation with chromatin-bound PCNA (Jin et al., 2006). It is, therefore, conceivable that DCAF13 also might need other cofactors, such as chromatin, RNA, or metal-ions, to facilitate the binding and

ubiquitination of its designated substrates. These co-factors and, thus, the potential substrates would be lost during the FLAG-IP process. A recent report has proposed that DCAF13 acts as an RNA-binding protein in breast cancer (J. Liu et al., 2020), supporting the idea that DCAF13 might need co-factors, such as RNA, for substrate ubiquitination. To overcome these limitations, one could perform a proximity-dependent biotin identification (BioID) experiment. The BioID method uses a promiscuous biotin ligase discovered in *E.coli*, which can biotinylate proteins in close proximity and allows the mapping of protein-protein interactions under near-physiological conditions (Roux et al., 2012). The biotin ligase is fused to the protein of interest, thereby marking associating proteins over time in living cells. Biotinylated proteins are then captured through streptavidin purification and analyzed by mass spectrometry. As the BioID-enzyme is comparatively large, with a size of around 35 kDa, and is therefore likely to alter the physiological behavior of its fused protein of interest, recent efforts have brought forth a variety of smaller and more potent versions of the original BioID enzyme, such as the BioID2 (D. I. Kim et al., 2016), the TurboID (Branon et al., 2018), and the MicroID2 (Johnson et al., 2022). TurboID is similar in size to the original BioID (35 kDa) but displays more potent biotinylation activity, enabling higher temporal resolution of protein-protein interactions (Branon et al., 2018). The MicroID2 shows lower biotinylation efficiency. However, at 19 kDa, it is dramatically reduced in size, making it a more suitable option for small proteins of interest (Johnson et al., 2022). To identify physiological interaction partners of DCAF13, both the TurboID and MicroID2 could be employed. However, special care must be taken to validate that proper localization of the fusion construct to centrosomes, cell contacts, and the nucleus occurs.

Another complication of identifying interaction partners of ubiquitin ligases is that the interaction with their substrates is transient (Kleiger et al., 2009). Recent strategies to overcome this challenge have included chemical crosslinking of interacting proteins (Streich & Lima, 2016) or proteasomal inhibition to prevent rapid substrate degradation (T. Y. Kim et al., 2015). Elegant approaches by O'Connor *et al*. and Watanabe *et al*. have shown that fusion of the ligase of interest to a ubiquitin moiety that is then covalently attached to the substrate or a tandem ubiquitin-binding entity (TUBE) that binds the ubiquitinated substrate, respectively, can trap substrates at their designated ubiquitin ligases (O'Connor et al., 2015; Watanabe et al., 2020). These approaches could increase the probability of identifying elusive substrates through affinity-based purifications.

In sum, the BioID method, with a modified BioID enzyme, such as TurboID or MicroID2, should be employed to identify physiological interaction partners of DCAF13 *in vivo*. This could be combined with substrate-trapping strategies to induce substrate retention and increase biotinylation. However, should the fusion protein of BioID and DCAF13 not localize to the physiological subcellular compartments of DCAF13 in LuAD, a substrate-trapping strategy as proposed by O'Connor *et al.* or Watanabe *et al.* with subsequent FLAG-based purification should be the method of choice.

The second strategy presented in this study to identify DCAF13 ubiquitination substrates used ubiquitin-specific proteomics in the form of the diGLY method (Fulzele & Bennett, 2018). The diGLY method offers single peptide resolution of ubiquitination sites, and many peptides were found to be significantly less ubiquitinated upon DCAF13 depletion in HCC-44 and NCI-H1437 cells (Figure 35). During cross-validation with the DCAF13 interactome, proteins that did not have significantly altered peptides or were not detected in the diGLY measurement were excluded from the subsequent candidate selection (Figure 38).

This reveals a pitfall of this approach, as many proteins enriched in the interactome did not have any peptides identified in the diGLY mass spectrometric measurement. This is primarily due to the detection limit of mass spectrometry, where low abundant proteins, even though present in a particular sample, cannot be detected by the mass spectrometer (Karpievitch et al., 2009). Several proteins identified in the DCAF13 interactome belonged to the protein group of transcription factors, which are classically low abundant in the cell (D. Jiang et al., 2009). These transcription factors were not measured in the diGLY proteomics and were not followed up as substrate candidates. The stabilization of transcription factors can tremendously affect the cell, and this protein group could therefore be of high interest. To overcome the detection limit of the mass spectrometer, one could perform fractionation of the diGLY-enriched samples prior to measurement by mass spectrometry. Fractionation describes the separation of the initial sample into smaller fractions so that a larger depth of measurement can be achieved. A popular method for the fractionation of peptides is liquid chromatography, which separates proteins based on their biochemical properties (Paulo et al., 2012). For instance, peptides are separated according to their hydrophobicity as they are bound to C18 resin and eluted using organic solvents in increasing concentrations (Törnkvist et al., 2004). This approach was applied for the reference proteome samples that were analyzed in parallel to the diGLY enrichment, which were divided into six fractions by liquid chromatography before the measurement. This significantly increased the number of identified proteins from a single-shot measurement of the same sample (data not shown). Accordingly, the diGLY-enriched samples could be fractionated and measured similarly to increase measurement depth.

Another limitation of the diGLY proteomics approach is the tryptic digestion of proteins prior to the diGLY-motif enrichment. Trypsin digestion is needed to remove poly-ubiquitin chains to reveal the characteristic KGG (Lysine-glycine-glycine)-motif used for subsequent enrichment of priorly ubiquitinated lysines. Additionally, trypsin digestion ensures that each protein is digested into peptides, which is essential for bottom-up mass spectrometry. As trypsin cleaves after lysines and arginines, lysine- and arginine-rich protein domains will be digested into single amino acids or peptides that are too small for measurement by the mass spectrometer or are not unique enough to be mapped to a single protein after measurement. For instance, classic nuclear localization signals (NLS) are rich in lysines and arginines and will likely not be measured by this approach (Lu et al., 2021). However, these protein domains could be promising in the context of this project, as it is conceivable that the ubiquitination of the NLS alters the subcellular localization of a potential substrate. To circumvent this issue, enrichment of ubiquitinated proteins could be performed prior to tryptic digest and mass spectrometric analysis. Notably, this approach would reduce the resolution of ubiquitination from peptide to protein level. For instance, tagged ubiquitin could be used for marking and enriching ubiquitinated proteins, as described with poly-histidine-tagged ubiquitin (Beers & Callis, 1993). However, this method relies on non-physiological overexpression of the ubiquitin construct and could introduce artificial ubiquitination events. Another method, as described by Azkargorta *et al.*, employs tandem ubiquitin-binding entities (TUBEs) to enrich ubiquitinated proteins from cell lysates (Azkargorta et al., 2016) and perform subsequent mass spectrometric analysis. TUBEs are engineered protein domains that bind poly-ubiquitin chains (Hjerpe et al., 2009). Consequently, TUBEs-mass spectrometry, as described by Azkagorta *et al*., could be used to identify proteins that are less ubiquitinated upon DCAF13 depletion

without the need for overexpression of transgenic ubiquitin or loss of information due to tryptic digestion of ubiquitinated peptides.

6.4.2 CDC42 und CTNND1 as potential substrates

As previously discussed, cross-validation of the screening approaches for DCAF13 ubiquitination substrates yielded two candidates, CDC42 and CTNND1 (Figure 38), that were followed up with validation experiments. The interaction of these candidates with DCAF13 could be shown in LuAD cells, but not in HEK293T cells (Figure 39). An *in-vivo*-ubiquitination experiment in HEK293T cells showed no changes in the ubiquitination status of CDC42 or CTNND1 upon DCAF13 depletion. Due to the missing interaction between the candidates and DCAF13 in HEK293T cells, it is perhaps not surprising that no changes in ubiquitination could be observed. Thus, to investigate if DCAF13 can act as a ubiquitin ligase towards CDC42 or CTNND1 in LuAD cells, *in-vivo*-ubiquitination assays should be repeated in that cellular model. The *in-vivo*-ubiquitination assay requires the simultaneous depletion of DCAF13 and the overexpression of the HA-tagged ubiquitin and the FLAG-tagged substrate candidate. While genetic perturbance and overexpression of multiple constructs are well accepted by HEK293T cells, LuAD cells might react with feedback mechanisms to these manipulations. An elegant method to investigate changes in ubiquitination is the previously described TUBE assay (Hjerpe et al., 2009). Thus, TUBEs could be used to examine the ubiquitination status of CDC42 and CTNND1 upon DCAF13 depletion with minimal manipulation of LuAD cells. Further, should this assay reveal that CDC42 and CTNND1 are indeed less ubiquitinated upon DCAF13 depletion, the TUBE assay could be performed with TUBE variants that are specific towards certain types of ubiquitin chain type (mainly K48 and K63 linkages). This could offer valuable insight into the type of ubiquitin linkage conferred by DCAF13, as well as the potential molecular consequence of that linkage, such as destabilization of the substrate for K48 linkages.

6.4.3 Published ubiquitination substrates of DCAF13

Although DCAF13 is still largely uncharacterized and understudied, recent reports have proposed several ubiquitination substrates of DCAF13. Chen and colleagues reported in 2018 and 2019 that DCAF13 mediates ubiquitination of the tumor suppressor phosphatase and tensin homolog deleted on chromosome 10 (PTEN) in osteosarcoma cells. The authors identified PTEN through a mass spectrometry-based interactome screen of DCAF13 and claimed that it is less ubiquitinated and stabilized upon DCAF13 depletion, thereby inhibiting the growth of osteosarcoma cells (B. Chen et al., 2019; Z. Chen et al., 2018). Interestingly, a CRISPR/Cas9 screen in isogenic HEK293A cells with loss of function of various tumor suppressors, including PTEN, revealed that knockout of DCAF13 still led to depletion from the cell pool regardless of genetic background (Feng et al., 2022). As PTEN enrichment could not be the molecular mechanism that leads to the growth reduction of DCAF13-depleted cells in the context of PTEN knockout cells, it seems logical that other ubiquitination substrates of DCAF13 must confer the observed growth disadvantage in HEK293A cells. Moreover, PTEN was not identified as an interactor of DCAF13 in LuAD in the interactome screens presented in this study (Figure 33). Co-IP experiments performed by C. Dürr in the context of a dissertation for her Master of Science studies revealed that DCAF13 binds to PTEN in

HEK293T but not in LuAD cells. Additionally, destabilization of PTEN upon DCAF13 overexpression was not observed (Dürr, 2021). Context and tissue-dependent ubiquitination of substrates was found to largely depend on posttranslational modification of the ligase-recruiting signals, for instance termed degron for degradation signals(Varshavsky, 1991) , within the substrate or the tissue-specific presence of co-interactors (Ravid & Hochstrasser, 2008; N. Zheng & Shabek, 2017). Therefore, it is conceivable that DCAF13 acts as a ubiquitin ligase towards PTEN in osteosarcoma and that other ubiquitination substrates are more relevant in the context of LuAD and HEK293T.

In another report, Zhang *et al.* identified histone-lysine N-methyltransferase SUV39H1 (Suv39h1) as a ubiquitination substrate of Dcaf13 in oocyte maturation (Y. Zhang et al., 2018). SUV39H1 was not identified as an interactor of DCAF13 in LuAD (Figure 33), and diGLY proteomics showed an increase of ubiquitination upon DCAF13 depletion. This indicates that DCAF13 might not act as a ubiquitin ligase toward SUV39H1 in LuAD. Nevertheless, epigenetic regulation upon DCAF13 depletion is an interesting option that should be explored with further studies.

Shan *et al.* have identified *DCAF13* as a vulnerability in breast cancer, where DCAF13 depletion led to a striking increase of cells in the G1-phase and a modest increase of cells undergoing apoptosis. The authors proposed the protein p53 apoptosis effector related to PMP-22 (PERP) as ubiquitination substrate of DCAF13, as PERP depletion partially restored cell viability upon *DCAF13* knockout. The effect on cell growth could not be entirely rescued by *PERP* knockout, suggesting that other ubiquitination substrates could be important. In the mentioned study however, *PERP* mRNA levels were dramatically increased in the transcriptome analysis of *DCAF13* knockout cells, indicating that *PERP* might be regulated on the transcriptome level rather than post-translationally (Shan et al., 2022). PERP was neither identified as an interactor of DCAF13 nor was it measured in the diGLY proteomics screen presented in this thesis (Figure 35). Although it cannot be concluded that PERP does not play a role in DCAF13-mediated oncogenicity of LuAD cells, it seems unlikely that it is a ubiquitination substrate of DCAF13 in this context. Interestingly, another study of DCAF13 function in breast cancer found that DCAF13 acts as an RNA-binding protein and mediates the degradation of probable E3 ubiquitin-protein ligase DTX3 (*DTX3*) mRNA (J. Liu et al., 2020). While the authors observed an increase of *DTX3* mRNA upon DCAF13 depletion, this was not observed during the analysis of transcriptomic changes upon DCAF13 depletion presented in this thesis (Figure 27), indicating that this mechanism might be relevant in the context of breast cancer but not in LuAD. Nevertheless, further analysis is needed to determine whether DCAF13 can act as an RNA-binding protein in LuAD.

Lastly, a recent publication by Y. Pommier and colleagues identified topoisomerase I (TOP1) as a direct ubiquitination substrate of DCAF13 in colorectal cancer (Y. Sun et al., 2023). The authors showed that DCAF13 localizes to sites of DNA damage and mediates the repair of TOP1 DNA-protein crosslinks. TOP1 was not identified in the interactome analysis of DCAF13 presented in this study (Figure 33). However, diGLY proteomics showed a slight reduction of ubiquitination of TOP1 upon DCAF13 depletion. Further studies are needed to evaluate if DCAF13 acts as a ubiquitin ligase towards TOP1 in LuAD and if DCAF13 localizes to sites of DNA damage.

6.5 Concluding remarks

This study identified the ubiquitin ligase adapter *DCAF13* as a vulnerability in LuAD from a targeted CRISPR/Cas9 screen. Mechanistic studies showed that depletion of DCAF13 induces the intrinsic apoptosis pathway. Further, DCAF13-depleted cells are characterized by loss of actin stress fibers independent of caspase activation during apoptosis. To our knowledge, this study is the first to implicate DCAF13 as a regulator of the actin cytoskeleton. Further studies are needed to elucidate the mechanism by which DCAF13's effect on intrinsic apoptosis and stress fiber formation are connected and how the localization of DCAF13 in the nucleus, at the centrosome, and cell-to-cell contacts might influence these processes. The identification of relevant DCAF13 ubiquitination substrates in LuAD holds the potential to establish a connection between these findings. A systematic screening approach identified two possible candidates, CDC42 and CTNND1, and ongoing experiments seek to establish if these two proteins could be the link between the loss of actin stress fibers and apoptosis induction in LuAD.

The data presented in this study highlight the potential for DCAF13-targeted therapy in patients with LuAD and potentially various other cancer entities. *DCAF13* expression correlated with cancer aggressiveness and with a reduction in actionable oncogenic driver mutations and, thus, eligibility for targeted therapy in patients with LuAD. Developing DCAF13-targeted therapy might offer these patients a more successful and less toxic therapeutic option than systemic chemotherapy. The conclusive characterization of the molecular function and the ubiquitination substrates of DCAF13, building on the data presented in this thesis, will be a vital step in developing this targeted therapeutic.

7 Acknowledgements

Working on this project and finishing this dissertation has been a group effort in many ways. The last 4.5 years have been a truly special time, filled with many highs and many lows, and I want to take the time to thank all the people who helped me (somewhat) retain my sanity during the Ph.D. journey.

First, I want to thank my supervisor Prof. Dr. Florian Bassermann for giving me the opportunity to conduct the research leading to this thesis in his lab, for countless scientific discussions, and for supporting this project. Second, I want to thank my thesis advisory committee members, Prof. Dr. Hana Algül and Prof. Dr. Johannes Buchner, for their invaluable scientific feedback.

A special thank you goes to Anna Sperk and Antje Gabriel for the constant silliness and the absolute joy of the last 4.5 years. I would not have made it without our unwavering moral support triangle and the sunshine you two managed to bring, even on the cloudiest days. Big thanks to Dr. Priska Auf der Maur for the moral support and scientific advice on this project and the written thesis. I'm extremely glad to leave this project in your very capable hands!

I want to thank all past and present members of "Team DCAF13", including Nadine Glaisner, Carina Dürr, and Leonhard Thume. It was my joy to share this project with you. Thank you for your constant motivation and commitment and for your crucial contributions to this project.

Furthermore, I want to thank all collaboration partners for contributing to the success of this project. Special thanks to Dr. Piero Giansanti and Dr. Yun-Chien Chang for their invaluable support with the mass spectrometry analysis and data interpretation. Thank you to Rupert Öllinger for performing the sequencing for the CRISPR screen and the RNA sequencing.

I want to thank all current and former members of the Bassermann lab for being such an open, helpful, and fun group! Thank you for all your constructive input, help with various techniques, and wonderful lunch breaks. Thank you also to all other members of TranslaTUM who made this Ph.D. journey joyful.

Last but not least, my biggest thank you goes to my partner Simon, my whole family, and my friends for your continued support, your understanding, your patience, and for your constant belief in me. I'm truly thankful!

And now, finally, It's time for new adventures!

"I think we've outgrown full-time education …
Time to test our talents in the real world, d'you reckon?"
- Fred Weasley

8 Publications

8.1 Articles in peer-reviewed journals

Vinona Wagner, Priska Auf der Maur, Nadine Glaisner, Carina Dürr, Florian Bassermann „ DCAF13 is a vulnerability in lung adenocarcinoma that regulates the integrity of the actin cytoskeleton“. Submitted to *Cell reports* (2023)

8.2 Conference contributions

Vinona T Wagner, Yun-Chien Chang, Piero Giansanti, Rupert Öllinger, Thomas Engleitner, Bernhard Kuster, Florian Bassermann. “A multi-omic screening approach identifies the E3-ubiquitin ligase DCAF13 as a novel vulnerability in lung adenocarcinoma”. AACR Annual Meeting 2023, Orlando, Florida. Poster
Abstract concurrently published in *Cancer Research* (2023); 83 (7_Supplement): 2575. https://doi.org/10.1158/1538-7445.AM2023-2575

9 References

Abaandou, L., Quan, D., & Shiloach, J. (2021). Affecting HEK293 Cell Growth and Production Performance by Modifying the Expression of Specific Genes. *Cells 2021, Vol. 10, Page 1667*, *10*(7), 1667. https://doi.org/10.3390/CELLS10071667

Acehan, D., Jiang, X., Morgan, D. G., Heuser, J. E., Wang, X., & Akey, C. W. (2002). Three-dimensional structure of the apoptosome: Implications for assembly, procaspase-9 binding, and activation. *Molecular Cell*, *9*(2), 423–432. https://doi.org/10.1016/S1097-2765(02)00442-2

Aguirre, A. J., Meyers, R. M., Weir, B. A., Vazquez, F., Zhang, C. Z., Ben-David, U., Cook, A., Ha, G., Harrington, W. F., Doshi, M. B., Kost-Alimova, M., Gill, S., Xu, H., Ali, L. D., Jiang, G., Pantel, S., Lee, Y., Goodale, A., Cherniack, A. D., … Hahn, W. C. (2016). Genomic Copy Number Dictates a Gene-Independent Cell Response to CRISPR/Cas9 Targeting. *Cancer Discovery*, *6*(8), 914–929. https://doi.org/10.1158/2159-8290.CD-16-0154

Ahuja, R., Pinyol, R., Reichenbach, N., Custer, L., Klingensmith, J., Kessels, M. M., & Qualmann, B. (2007). Cordon-Bleu Is an Actin Nucleation Factor and Controls Neuronal Morphology. *Cell*, *131*(2), 337–350. https://doi.org/10.1016/j.cell.2007.08.030

Angers, S., Li, T., Yi, X., MacCoss, M. J., Moon, R. T., & Zheng, N. (2006). Molecular architecture and assembly of the DDB1–CUL4A ubiquitin ligase machinery. *Nature 2006 443:7111*, *443*(7111), 590–593. https://doi.org/10.1038/nature05175

Argenzio, E., Klarenbeek, J., Kedziora, K. M., Nahidiazar, L., Isogai, T., Perrakis, A., Jalink, K., Moolenaar, W. H., & Innocenti, M. (2018). Profilin binding couples chloride intracellular channel protein CLIC4 to RhoA–mDia2 signaling and filopodium formation. *Journal of Biological Chemistry*, *293*(50), 19161–19176. https://doi.org/https://doi.org/10.1074/jbc.RA118.002779

Azkargorta, M., Escobes, I., Elortza, F., Matthiesen, R., & Rodríguez, M. S. (2016). Tubes-mass spectrometry for identifi cation and analysis of the ubiquitin-proteome. *Methods in Molecular Biology*, *1449*, 177–192. https://doi.org/10.1007/978-1-4939-3756-1_9/COVER

Bade, B. C., & Dela Cruz, C. S. (2020). Lung Cancer 2020: Epidemiology, Etiology, and Prevention. *Clinics in Chest Medicine*, *41*(1), 1–24. https://doi.org/10.1016/J.CCM.2019.10.001

Banfalvi, G. (2017). Methods to detect apoptotic cell death. *Apoptosis*, *22*(2), 306–323. https://doi.org/https://doi.org/10.1007/s10495-016-1333-3

Bard, J. A. M., Goodall, E. A., Greene, E. R., Jonsson, E., Dong, K. C., & Martin, A. (2018). Structure and Function of the 26S Proteasome. *Annual Review of Biochemistry*, *87*, 697–724. https://doi.org/https://doi.org/10.1146/annurev-biochem-062917-011931

Beers, E. P., & Callis, J. (1993). Utility of Polyhistidine-tagged Ubiquitin in the Purification of Ubiquitin-Protein Conjugates and as an Affinity Ligand for the Purification of Ubiquitin-specific Hydrolases*. *The Journal of Biological Chemistry*, *268*(29), 21645–21649. https://doi.org/10.1016/S0021-9258(20)80590-0

Békés, M., Langley, D. R., & Crews, C. M. (2022). PROTAC targeted protein degraders: the past is prologue. *Nature Reviews. Drug Discovery*, *21*(3), 181–200. https://doi.org/10.1038/S41573-021-00371-6

Benard, G., Neutzner, A., Peng, G., Wang, C., Livak, F., Youle, R. J., & Karbowski, M. (2010). IBRDC2, an IBR-type E3 ubiquitin ligase, is a regulatory factor for Bax and apoptosis activation. *The EMBO Journal*, *29*(8), 1458–1471. https://doi.org/10.1038/EMBOJ.2010.39

Bertheloot, D., Latz, E., & Franklin, B. S. (2021). Necroptosis, pyroptosis and apoptosis: an intricate game of cell death. *Cellular and Molecular Immunology*, *18*(5), 1106–1121. https://doi.org/10.1038/S41423-020-00630-3

Bogucka-Janczi, K., Harms, G., Coissieux, M. M., Bentires-Alj, M., Thiede, B., & Rajalingam, K. (2023). ERK3/MAPK6 dictates CDC42/RAC1 activity and ARP2/3-dependent actin polymerization. *ELife*, *12*. https://doi.org/10.7554/ELIFE.85167

Branon, T. C., Bosch, J. A., Sanchez, A. D., Udeshi, N. D., Svinkina, T., Carr, S. A., Feldman, J. L., Perrimon, N., & Ting, A. Y. (2018). Efficient proximity labeling in living cells and organisms with TurboID. *Nature Biotechnology*, *36*(9), 880. https://doi.org/10.1038/NBT.4201

Brault, M., Olsen, T. M., Martinez, J., Stetson, D. B., & Oberst, A. (2018). Intracellular Nucleic Acid Sensing Triggers Necroptosis through Synergistic Type I IFN and TNF Signaling. *Journal of Immunology*, *200*(8), 2748–2756. https://doi.org/10.4049/JIMMUNOL.1701492

Brühmann, S., Ushakov, D. S., Winterhoff, M., Dickinson, R. B., Curth, U., & Faix, J. (2017). Distinct VASP tetramers synergize in the processive elongation of individual actin filaments from clustered arrays. *Proceedings of the National Academy of Sciences of the United States of America*, *114*(29), E5815–E5824. https://doi.org/https://doi.org/10.1073/pnas.1703145114

Buetow, L., & Huang, D. T. (2016). Structural insights into the catalysis and regulation of E3 ubiquitin ligases. *Nature Reviews. Molecular Cell Biology*, *17*(10), 626. https://doi.org/10.1038/NRM.2016.91

Cai, Z., Jitkaew, S., Zhao, J., Chiang, H. C., Choksi, S., Liu, J., Ward, Y., Wu, L. G., & Liu, Z. G. (2014). Plasma membrane translocation of trimerized MLKL protein is required for TNF-induced necroptosis. *Nature Cell Biology*, *16*(1), 55–65. https://doi.org/10.1038/NCB2883

Cain, K., Bratton, S. B., & Cohen, G. M. (2002). The Apaf-1 apoptosome: A large caspase-activating complex. *Biochimie*, *84*(2–3), 203–214. https://doi.org/10.1016/S0300-9084(02)01376-7

Cao, J., Hou, P., Chen, J., Wang, P., Wang, W., Liu, W., Liu, C., & He, X. (2017). The overexpression and prognostic role of DCAF13 in hepatocellular carcinoma. *Tumor Biology*, *39*(6). https://doi.org/10.1177/1010428317705753

Cardozo, T., & Pagano, M. (2004). The SCF ubiquitin ligase: insights into a molecular machine. *Nature Reviews Molecular Cell Biology 2004 5:9*, *5*(9), 739–751. https://doi.org/10.1038/nrm1471

Cerretti, D. P., Kozlosky, C. J., Mosley, B., Nelson, N., Van Ness, K., Greenstreet, T. A., March, C. J., Kronheim, S. R., Druck, T., Cannizzaro, L. A., Huebner, K., & Black, R. A. (1992). Molecular cloning of the interleukin-1 beta converting enzyme. *Science*, *256*(5053), 97–100. https://doi.org/10.1126/SCIENCE.1373520

Chen, B., Feng, Y., Zhang, M., Cheng, G., Chen, B., & Wang, H. (2019). Small molecule TSC01682 inhibits osteosarcoma cell growth by specifically disrupting the CUL4B-DDB1 interaction and decreasing the ubiquitination of CRL4B E3 ligase substrates. *American Journal of Cancer Research*, *9*(9), 1857–1870. /pmc/articles/PMC6780663/

Chen, Y., Lun, A. T. L., Smyth, G. K., Burden, C. J., Ryan, D. P., & Khang, T. F. (2016). From reads to genes to pathways: differential expression analysis of RNA-Seq experiments using Rsubread and the edgeR quasi-likelihood pipeline. *F1000Research 2016 5:1438*, *5*, 1438. https://doi.org/10.12688/f1000research.8987.2

Chen, Z. J., & Sun, L. J. (2009). Nonproteolytic Functions of Ubiquitin in Cell Signaling. *Molecular Cell*, *33*(3), 275–286. https://doi.org/10.1016/J.MOLCEL.2009.01.014

Chen, Z., Zhang, W., Jiang, K., Chen, B., Wang, K., Lao, L., Hou, C., Wang, F., Zhang, C., & Shen, H. (2018). MicroRNA-300 Regulates the Ubiquitination of PTEN through the CRL4BDCAF13 E3 Ligase in Osteosarcoma Cells. *Molecular Therapy - Nucleic Acids*, *10*, 254–268. https://doi.org/10.1016/j.omtn.2017.12.010

Cho, Y. S., Challa, S., Moquin, D., Genga, R., Ray, T. D., Guildford, M., & Chan, F. K. M. (2009). Phosphorylation-driven assembly of the RIP1-RIP3 complex regulates programmed necrosis and virus-induced inflammation. *Cell*, *137*(6), 1112–1123. https://doi.org/10.1016/J.CELL.2009.05.037

Chua, B. T., Volbracht, C., Tan, K. O., Li, R., Yu, V. C., & Li, P. (2003). Mitochondrial translocation of cofilin is an early step in apoptosis induction. *Nature Cell Biology*, *5*(12), 1083–1089. https://doi.org/10.1038/NCB1070

Cohen, G. M. (1997). Caspases: the executioners of apoptosis. *The Biochemical Journal*, *326 (Pt 1)*(Pt 1), 1–16. https://doi.org/10.1042/BJ3260001

Coleman, M. L., Sahai, E. A., Yeo, M., Bosch, M., Dewar, A., & Olson, M. F. (2001). Membrane blebbing during apoptosis results from caspase-mediated activation of ROCK I. *Nature Cell Biology 2001 3:4*, *3*(4), 339–345. https://doi.org/10.1038/35070009

Collisson, E. A., Campbell, J. D., Brooks, A. N., Berger, A. H., Lee, W., Chmielecki, J., Beer, D. G., Cope, L., Creighton, C. J., Danilova, L., Ding, L., Getz, G., Hammerman, P. S., Hayes, D. N., Hernandez, B., Herman, J. G., Heymach, J. V., Jurisica, I., Kucherlapati, R., … Cheney, R. (2014). Comprehensive molecular profiling of lung adenocarcinoma. *Nature*, *511*(7511), 543. https://doi.org/10.1038/NATURE13385

Conrad, M., & Pratt, D. A. (2019). The chemical basis of ferroptosis. *Nature Chemical Biology 2019 15:12*, *15*(12), 1137–1147. https://doi.org/10.1038/s41589-019-0408-1

Coux, O., Tanaka, K., & Goldberg, A. L. (2003). STRUCTURE AND FUNCTIONS OF THE 20S AND 26S PROTEASOMES. *Annual Review of Biochemistry* , *65*, 801–847. https://doi.org/https://doi.org/10.1146/annurev.bi.65.070196.004101

Creagh, E. M., Conroy, H., & Martin, S. J. (2003). Caspase-activation pathways in apoptosis and immunity. *Immunological Reviews*, *193*, 10–21. https://doi.org/10.1034/J.1600-065X.2003.00048.X

Daniel, J. M. (2007). Dancing in and out of the nucleus: p120(ctn) and the transcription factor Kaiso. *Biochimica et Biophysica Acta*, *1773*(1), 59–68. https://doi.org/10.1016/J.BBAMCR.2006.08.052

D'Arcy, M. S. (2019). Cell death: a review of the major forms of apoptosis, necrosis and autophagy. *Cell Biology International*, *43*(6), 582–592. https://doi.org/10.1002/CBIN.11137

Deng, W., Bai, Y., Deng, F., Pan, Y., Mei, S., Zheng, Z., Min, R., Wu, Z., Li, W., Miao, R., Zhang, Z., Kupper, T. S., Lieberman, J., & Liu, X. (2022). Streptococcal pyrogenic exotoxin B cleaves GSDMA and triggers pyroptosis. *Nature*, *602*(7897), 496. https://doi.org/10.1038/S41586-021-04384-4

DepMap Consortium. (2018). *DepMap: The Cancer Dependency Map Project at Broad Institute*.

Deshaies, R. J., & Joazeiro, C. A. P. (2009). RING domain E3 ubiquitin ligases. *Annual Review of Biochemistry*, *78*, 399–434. https://doi.org/10.1146/ANNUREV.BIOCHEM.78.101807.093809

Dickson, D. W. (2004). Apoptotic mechanisms in Alzheimer neurofibrillary degeneration: cause or effect? *Journal of Clinical Investigation*, *114*(1), 23. https://doi.org/10.1172/JCI22317

Ding, L., Bailey, M. H., Porta-Pardo, E., Thorsson, V., Colaprico, A., Bertrand, D., Gibbs, D. L., Weerasinghe, A., Huang, K. lin, Tokheim, C., Cortés-Ciriano, I., Jayasinghe, R., Chen, F., Yu, L., Sun, S., Olsen, C., Kim, J., Taylor, A. M., Cherniack, A. D., … Mariamidze, A. (2018). Perspective on Oncogenic Processes at the End of the Beginning of Cancer

Genomics. *Cell*, *173*(2), 305-320.e10. https://doi.org/https://doi.org/10.1016/j.cell.2018.03.033

Ding, L., Getz, G., Wheeler, D. A., Mardis, E. R., McLellan, M. D., Cibulskis, K., Sougnez, C., Greulich, H., Muzny, D. M., Morgan, M. B., Fulton, L., Fulton, R. S., Zhang, Q., Wendl, M. C., Lawrence, M. S., Larson, D. E., Chen, K., Dooling, D. J., Sabo, A., … Wilson, R. K. (2008). Somatic mutations affect key pathways in lung adenocarcinoma. *Nature*, *455*(7216), 1069. https://doi.org/10.1038/NATURE07423

Dixon, S. J., Lemberg, K. M., Lamprecht, M. R., Skouta, R., Zaitsev, E. M., Gleason, C. E., Patel, D. N., Bauer, A. J., Cantley, A. M., Yang, W. S., Morrison, B., & Stockwell, B. R. (2012). Ferroptosis: An iron-dependent form of nonapoptotic cell death. *Cell*, *149*(5), 1060–1072. https://doi.org/10.1016/j.cell.2012.03.042

Dong, L., Liang, F., Lou, Z., Li, Y., Li, J., Chen, Y., Ding, J., Jiang, B., Wu, C., Yu, H., Liu, Y., Zhang, W., Lu, Y., & Wu, M. (2022). Necrostatin-1 Alleviates Lung Ischemia-Reperfusion Injury via Inhibiting Necroptosis and Apoptosis of Lung Epithelial Cells. *Cells*, *11*(19). https://doi.org/10.3390/CELLS11193139

Dürr, C. (2021). *Identifying substrates of the E3 ubiquitin ligase DCAF13 in lung adenocarcinoma*. Technical University of Munich.

Eberhardt, W. E. E., De Ruysscher, D., Weder, W., Le Péchoux, C., De Leyn, P., Hoffmann, H., Westeel, V., Stahel, R., Felip, E., Peters, S., Kerr, K., Besse, B., Vansteenkiste, J., Edelman, M., Mok, T., O'Byrne, K., Novello, S., Bubendorf, L., Marchetti, A., … Dooms, C. (2015). 2nd ESMO Consensus Conference in Lung Cancer: locally advanced stage III non-small-cell lung cancer. *Annals of Oncology*, *26*(8), 1573–1588. https://doi.org/10.1093/ANNONC/MDV187

Eischen, C. M. (2016). Genome Stability Requires p53. *Cold Spring Harbor Perspectives in Medicine*, *6*(6). https://doi.org/10.1101/CSHPERSPECT.A026096

Elmore, S. (2007). Apoptosis: A Review of Programmed Cell Death. *Toxicologic Pathology*, *35*(4), 495. https://doi.org/10.1080/01926230701320337

Evavold, C. L., Ruan, J., Tan, Y., Xia, S., Wu, H., & Kagan, J. C. (2018). The pore forming protein gasdermin D regulates interleukin-1 secretion from living macrophages. *Immunity*, *48*(1), 35. https://doi.org/10.1016/J.IMMUNI.2017.11.013

Fan, B. Y., Pang, Y. L., Li, W. X., Zhao, C. X., Zhang, Y., Wang, X., Ning, G. Z., Kong, X. H., Liu, C., Yao, X., & Feng, S. Q. (2021). Liproxstatin-1 is an effective inhibitor of oligodendrocyte ferroptosis induced by inhibition of glutathione peroxidase 4. *Neural Regeneration Research*, *16*(3), 561–566. https://doi.org/10.4103/1673-5374.293157

Feng, X., Tang, M., Dede, M., Su, D., Pei, G., Jiang, D., Wang, C., Chen, Z., Li, M., Nie, L., Xiong, Y., Li, S., Park, J. M., Zhang, H., Huang, M., Szymonowicz, K., Zhao, Z., Hart, T., & Chen, J. (2022). Genome-wide CRISPR screens using isogenic cells reveal

vulnerabilities conferred by loss of tumor suppressors. *Science Advances*, *8*(19). https://doi.org/10.1126/SCIADV.ABM6638

Ferlay, J., Colombet, M., Soerjomataram, I., Parkin, D. M., Piñeros, M., Znaor, A., & Bray, F. (2021). Cancer statistics for the year 2020: An overview. *International Journal of Cancer*, *149*(4), 778–789. https://doi.org/10.1002/IJC.33588

Fouad, S., Wells, O. S., Hill, M. A., & D'Angiolella, V. (2019). Cullin Ring Ubiquitin Ligases (CRLs) in Cancer: Responses to Ionizing Radiation (IR) Treatment. *Frontiers in Physiology*, *10*, 469917. https://doi.org/10.3389/FPHYS.2019.01144/BIBTEX

Fujii, T., Iwane, A. H., Yanagida, T., & Namba, K. (2010). Direct visualization of secondary structures of F-actin by electron cryomicroscopy. *Nature 2010 467:7316*, *467*(7316), 724–728. https://doi.org/10.1038/nature09372

Fulzele, A., & Bennett, E. J. (2018). Ubiquitin diGLY proteomics as an approach to identify and quantify the ubiquitin-modified proteome. *Methods in Molecular Biology (Clifton, N.J.)*, *1844*, 363. https://doi.org/10.1007/978-1-4939-8706-1_23

Gandhi, L., Rodríguez-Abreu, D., Gadgeel, S., Esteban, E., Felip, E., De Angelis, F., Domine, M., Clingan, P., Hochmair, M. J., Powell, S. F., Cheng, S. Y.-S., Bischoff, H. G., Peled, N., Grossi, F., Jennens, R. R., Reck, M., Hui, R., Garon, E. B., Boyer, M., … Garassino, M. C. (2018). Pembrolizumab plus Chemotherapy in Metastatic Non–Small-Cell Lung Cancer. *New England Journal of Medicine*, *378*(22), 2078–2092. https://doi.org/10.1056/NEJMoa1801005

Gao, M., Monian, P., Quadri, N., Ramasamy, R., & Jiang, X. (2015). Glutaminolysis and Transferrin Regulate Ferroptosis. *Molecular Cell*, *59*(2), 298–308. https://doi.org/10.1016/j.molcel.2015.06.011

Gon, S., Gatanaga, T., & Sendo, F. (1996). Involvement of two types of TNF receptor in TNF-alpha induced neutrophil apoptosis. *Microbiology and Immunology*, *40*(6), 463–465. https://doi.org/10.1111/J.1348-0421.1996.TB01095.X

Grespi, F., Soratroi, C., Krumschnabel, G., Sohm, B., Ploner, C., Geley, S., Hengst, L., Häcker, G., & Villunger, A. (2010). BH3-only protein Bmf mediates apoptosis upon inhibition of CAP-dependent protein synthesis. *Cell Death and Differentiation*, *17*(11), 1672. https://doi.org/10.1038/CDD.2010.97

Guojie, Q., Chen, L., Jincai, W., & Zhouri, L. (2019). Identification of an eight-gene signature for survival prediction for patients with hepatocellular carcinoma based on integrated bioinformatics analysis. *PeerJ*, *7*(3). https://doi.org/10.7717/PEERJ.6548

Hall, A. K. (1995). Thymosin beta-10 accelerates apoptosis. *Cellular & Molecular Biology Research*, *41*(3), 167–180. https://europepmc.org/article/med/8589757

Hanahan, D., & Weinberg, R. A. (2000). The Hallmarks of Cancer. *Cell*, *100*(1), 57–70. https://doi.org/10.1016/S0092-8674(00)81683-9

Hanahan, D., & Weinberg, R. A. (2011). Hallmarks of cancer: The next generation. *Cell*, *144*(5), 646–674. https://doi.org/https://doi.org/10.1016/j.cell.2011.02.013

He, S., Liang, Y., Shao, F., & Wang, X. (2011). Toll-like receptors activate programmed necrosis in macrophages through a receptor-interacting kinase-3-mediated pathway. *Proceedings of the National Academy of Sciences of the United States of America*, *108*(50), 20054–20059. https://doi.org/10.1073/PNAS.1116302108

He, Y. J., McCall, C. M., Hu, J., Zeng, Y., & Xiong, Y. (2006). DDB1 functions as a linker to recruit receptor WD40 proteins to CUL4–ROC1 ubiquitin ligases. *Genes & Development*, *20*(21), 2949–2954. https://doi.org/10.1101/GAD.1483206

Hendriks, L. E., Kerr, K. M., Menis, J., Mok, T. S., Nestle, U., Passaro, A., Peters, S., Planchard, D., Smit, E. F., Solomon, B. J., Veronesi, G., & Reck, M. (2023a). Non-oncogene-addicted metastatic non-small-cell lung cancer: ESMO Clinical Practice Guideline for diagnosis, treatment and follow-up☆. *Annals of Oncology*, *34*(4), 358–376. https://doi.org/https://doi.org/10.1016/j.annonc.2022.12.013

Hendriks, L. E., Kerr, K. M., Menis, J., Mok, T. S., Nestle, U., Passaro, A., Peters, S., Planchard, D., Smit, E. F., Solomon, B. J., Veronesi, G., & Reck, M. (2023b). Oncogene-addicted metastatic non-small-cell lung cancer: ESMO Clinical Practice Guideline for diagnosis, treatment and follow-up☆. *Annals of Oncology*, *34*(4), 339–357. https://doi.org/https://doi.org/10.1016/j.annonc.2022.12.009

Hershko, A., & Ciechanover, A. (1998). The ubiquitin system. *Annual Review of Biochemistry*, *67*, 425–479. https://doi.org/10.1146/ANNUREV.BIOCHEM.67.1.425

Hjerpe, R., Aillet, F., Lopitz-Otsoa, F., Lang, V., England, P., & Rodriguez, M. S. (2009). Efficient protection and isolation of ubiquitylated proteins using tandem ubiquitin-binding entities. *EMBO Reports*, *10*(11), 1250–1258. https://doi.org/10.1038/EMBOR.2009.192

Holler, N., Zaru, R., Micheau, O., Thome, M., Attinger, A., Valitutti, S., Bodmer, J. L., Schneider, P., Seed, B., & Tschopp, J. (2000). Fas triggers an alternative, caspase-8-independent cell death pathway using the kinase RIP as effector molecule. *Nature Immunology*, *1*(6), 489–495. https://doi.org/10.1038/82732

Ichim, G., & Tait, S. W. G. (2016). A fate worse than death: apoptosis as an oncogenic process. *Nature Reviews Cancer 2016 16:8*, *16*(8), 539–548. https://doi.org/10.1038/nrc.2016.58

Igney, F. H., & Krammer, P. H. (2002). Death and anti-death: tumour resistance to apoptosis. *Nature Reviews Cancer 2002 2:4*, *2*(4), 277–288. https://doi.org/10.1038/nrc776

Imielinski, M., Berger, A. H., Hammerman, P. S., Hernandez, B., Pugh, T. J., Hodis, E., Cho, J., Suh, J., Capelletti, M., Sivachenko, A., Sougnez, C., Auclair, D., Lawrence, M. S., Stojanov, P., Cibulskis, K., Choi, K., De Waal, L., Sharifnia, T., Brooks, A., … Meyerson, M. (2012). Mapping the hallmarks of lung adenocarcinoma with massively parallel sequencing. *Cell*, *150*(6), 1107–1120. https://doi.org/10.1016/j.cell.2012.08.029

Ishiyama, N., Lee, S. H., Liu, S., Li, G. Y., Smith, M. J., Reichardt, L. F., & Ikura, M. (2010). Dynamic and static interactions between p120 catenin and E-cadherin regulate the stability of cell-cell adhesion. *Cell*, *141*(1), 117–128. https://doi.org/10.1016/J.CELL.2010.01.017

Iwai, S., Yonekawa, A., Harada, C., Hamada, M., Katagiri, W., Nakazawa, M., & Yura, Y. (2010). Involvement of the Wnt-β-catenin pathway in invasion and migration of oral squamous carcinoma cells. *International Journal of Oncology*, *37*(5), 1095–1103. https://doi.org/10.3892/IJO_00000761/HTML

Jassem, J., de Marinis, F., Giaccone, G., Vergnenegre, A., Barrios, C. H., Morise, M., Felip, E., Oprean, C., Kim, Y. C., Andric, Z., Mocci, S., Enquist, I., Komatsubara, K., McCleland, M., Kuriki, H., Villalobos, M., Phan, S., Spigel, D. R., & Herbst, R. S. (2021). Updated Overall Survival Analysis From IMpower110: Atezolizumab Versus Platinum-Based Chemotherapy in Treatment-Naive Programmed Death-Ligand 1–Selected NSCLC. *Journal of Thoracic Oncology*, *16*(11), 1872–1882. https://doi.org/10.1016/J.JTHO.2021.06.019

Jiang, D., Jarrett, H. W., & Haskins, W. E. (2009). Methods for Proteomic Analysis of Transcription Factors. *Journal of Chromatography. A*, *1216*(41), 6881. https://doi.org/10.1016/J.CHROMA.2009.08.044

Jiang, X., Stockwell, B. R., & Conrad, M. (2021). Ferroptosis: mechanisms, biology, and role in disease. *Nature Reviews. Molecular Cell Biology*, *22*(4), 266. https://doi.org/10.1038/S41580-020-00324-8

Jin, J., Arias, E. E., Chen, J., Harper, J. W., & Walter, J. C. (2006). A Family of Diverse Cul4-Ddb1-Interacting Proteins Includes Cdt2, which Is Required for S Phase Destruction of the Replication Factor Cdt1. *Molecular Cell*, *23*(5), 709–721. https://doi.org/10.1016/j.molcel.2006.08.010

Johnson, B. S., Chafin, L., Farkas, D., Adair, J., Elhance, A., Farkas, L., Bednash, J. S., & Londino, J. D. (2022). MicroID2: A Novel Biotin Ligase Enables Rapid Proximity-Dependent Proteomics. *Molecular & Cellular Proteomics*, *21*(7). https://doi.org/10.1016/J.MCPRO.2022.100256

Kadara, H., Choi, M., Zhang, J., Parra, E. R., Rodriguez-Canales, J., Gaffney, S. G., Zhao, Z., Behrens, C., Fujimoto, J., Chow, C., Yoo, Y., Kalhor, N., Moran, C., Rimm, D., Swisher, S., Gibbons, D. L., Heymach, J., Kaftan, E., Townsend, J. P., … Herbst, R. S. (2017). Whole-exome sequencing and immune profiling of early-stage lung adenocarcinoma with fully annotated clinical follow-up. *Annals of Oncology*, *28*(1), 75–82. https://doi.org/10.1093/ANNONC/MDW436

Kanellos, G., & Frame, M. C. (2016). Cellular functions of the ADF/cofilin family at a glance. *Journal of Cell Science*, *129*(17), 3211–3218. https://doi.org/https://doi.org/10.1242/jcs.187849

Karpievitch, Y., Stanley, J., Taverner, T., Huang, J., Adkins, J. N., Ansong, C., Heffron, F., Metz, T. O., Qian, W. J., Yoon, H., Smith, R. D., & Dabney, A. R. (2009). A statistical framework for protein quantitation in bottom-up MS-based proteomics. *Bioinformatics*, *25*(16), 2028. https://doi.org/10.1093/BIOINFORMATICS/BTP362

Kerr, J. F. R., Wyllie, A. H., & Currie, A. R. (1972). Apoptosis: A Basic Biological Phenomenon with Wide-ranging Implications in Tissue Kinetics. *British Journal of Cancer*, *26*(4), 239. https://doi.org/10.1038/BJC.1972.33

Kim, J. Bin, Kim, S. Y., Kim, B. M., Lee, H., Kim, I., Yun, J., Jo, Y., Oh, T., Jo, Y., Chae, H. D., & Shin, D. Y. (2013). Identification of a Novel Anti-apoptotic E3 Ubiquitin Ligase That Ubiquitinates Antagonists of Inhibitor of Apoptosis Proteins SMAC, HtrA2, and ARTS. *Journal of Biological Chemistry*, *288*(17), 12014–12021. https://doi.org/10.1074/JBC.M112.436113

Kim, D. I., Jensen, S. C., Noble, K. A., Kc, B., Roux, K. H., Motamedchaboki, K., & Roux, K. J. (2016). An improved smaller biotin ligase for BioID proximity labeling. *Molecular Biology of the Cell*, *27*(8), 1188. https://doi.org/10.1091/MBC.E15-12-0844

Kim, T. Y., Siesser, P. F., Rossman, K. L., Goldfarb, D., Mackinnon, K., Yan, F., Yi, X., MacCoss, M. J., Moon, R. T., Der, C. J., & Major, M. B. (2015). Substrate trapping proteomics reveals targets of the βTrCP2/FBXW11 ubiquitin ligase. *Molecular and Cellular Biology*, *35*(1), 167–181. https://doi.org/10.1128/MCB.00857-14

Klamt, F., Zdanov, S., Levine, R. L., Parisera, A., Zhang, Y., Zhang, B., Yu, L. R., Veenstra, T. D., & Shacter, E. (2009). Oxidant-induced apoptosis is mediated by oxidation of the actin-regulatory protein cofilin. *Nature Cell Biology*, *11*(10), 1241–1246. https://doi.org/10.1038/NCB1968

Kleiger, G., Saha, A., Lewis, S., Kuhlman, B., & Deshaies, R. J. (2009). Rapid E2-E3 assembly and disassembly enable processive ubiquitylation of cullin-RING ubiquitin ligase substrates. *Cell*, *139*(5), 957. https://doi.org/10.1016/J.CELL.2009.10.030

Komander, D., Clague, M. J., & Urbé, S. (2009). Breaking the chains: structure and function of the deubiquitinases. *Nature Reviews Molecular Cell Biology*, *10*(8), 550–563. https://doi.org/10.1038/nrm2731

Komander, D., & Rape, M. (2012). The Ubiquitin Code. *Annual Review of Biochemistry*, *81*(1), 203–229. https://doi.org/10.1146/annurev-biochem-060310-170328

Kovacs, E. M., & Yap, A. S. (2002). The web and the rock: Cell adhesion and the ARP2/3 complex. *Developmental Cell*, *3*(6), 760–761. https://doi.org/10.1016/S1534-5807(02)00374-X

Kwak, E. L., Bang, Y.-J., Camidge, D. R., Shaw, A. T., Solomon, B., Maki, R. G., Ou, S.-H. I., Dezube, B. J., Jänne, P. A., Costa, D. B., Varella-Garcia, M., Kim, W.-H., Lynch, T. J., Fidias, P., Stubbs, H., Engelman, J. A., Sequist, L. V., Tan, W., Gandhi, L., … Iafrate, A. J. (2010). Anaplastic Lymphoma Kinase Inhibition in Non–Small-Cell Lung Cancer. *New*

England Journal of Medicine, *363*(18), 1693–1703. https://doi.org/10.1056/NEJMoa1006448

Landspersky, T., Saçma, M., Rivière, J., Hecker, J. S., Hettler, F., Hameister, E., Brandstetter, K., Istvánffy, R., Romero Marquez, S., Ludwig, R., Götz, M., Buck, M., Wolf, M., Schiemann, M., Ruland, J., Strunk, D., Shimamura, A., Myers, K., Yamaguchi, T. P., … Oostendorp, R. A. J. (2022). Autophagy in mesenchymal progenitors protects mice against bone marrow failure after severe intermittent stress. *Blood*, *139*(5), 690–703. https://doi.org/10.1182/BLOOD.2021011775

Lee, J., & Zhou, P. (2007). DCAFs, the Missing Link of the CUL4-DDB1 Ubiquitin Ligase. *Molecular Cell*, *26*(6), 775–780. https://doi.org/10.1016/j.molcel.2007.06.001

Li, H., Zhu, H., Xu, C. J., & Yuan, J. (1998). Cleavage of BID by caspase 8 mediates the mitochondrial damage in the Fas pathway of apoptosis. *Cell*, *94*(4), 491–501. https://doi.org/10.1016/S0092-8674(00)81590-1

Linder, S., Higgs, H., Hüfner, K., Schwarz, K., Pannicke, U., & Aepfelbacher, M. (2000). The Polarization Defect of Wiskott-Aldrich Syndrome Macrophages Is Linked to Dislocalization of the Arp2/3 Complex. *The Journal of Immunology*, *165*(1), 221–225. https://doi.org/10.4049/JIMMUNOL.165.1.221

Liu, J., Li, H., Mao, A., Lu, J., Liu, W., Qie, J., & Pan, G. (2020). DCAF13 promotes triple-negative breast cancer metastasis by mediating DTX3 mRNA degradation. *Cell Cycle*, *19*(24), 3622–3631. https://doi.org/10.1080/15384101.2020.1859196

Liu, T., Wang, F., LePochat, P., Woo, J. A. A., Bukhari, M. Z., Hong, K. W., Trotter, C., & Kang, D. E. (2017). Cofilin-mediated Neuronal Apoptosis via p53 Translocation and PLD1 Regulation. *Scientific Reports*, *7*(1). https://doi.org/10.1038/S41598-017-09996-3

Liu, W. W., Hu, J., Wang, R., Han, Q., Liu, Y., & Wang, S. (2021). Cytoplasmic P120ctn Promotes Gefitinib Resistance in Lung Cancer Cells by Activating PAK1 and ERK Pathway. *Applied Immunohistochemistry & Molecular Morphology*, *29*(10), 750–758. https://doi.org/10.1097/PAI.0000000000000965

Liu, X., Zhang, Z., Ruan, J., Pan, Y., Magupalli, V. G., Wu, H., & Lieberman, J. (2016). Inflammasome-activated gasdermin D causes pyroptosis by forming membrane pores. *Nature*, *535*(7610), 153–158. https://doi.org/10.1038/NATURE18629

Liu, Y., Zhao, L. W., Shen, J. L., Fan, H. Y., & Jin, Y. (2019). Maternal DCAF13 Regulates Chromatin Tightness to Contribute to Embryonic Development. *Scientific Reports*, *9*(1). https://doi.org/10.1038/s41598-019-42179-w

Livak, K. J., & Schmittgen, T. D. (2001). Analysis of relative gene expression data using real-time quantitative PCR and the 2(-Delta Delta C(T)) Method. *Methods*, *25*(4), 402–408. https://doi.org/10.1006/METH.2001.1262

Lowry, O. H., Rosebrough, N. J., Farr, A. L., & Randall, R. J. (1951). Protein measurement with the folin phenol reagent. *Journal of Biological Chemistry*, *193*(1), 265–275. https://doi.org/10.1016/S0021-9258(19)52451-6

Lu, J., Wu, T., Zhang, B., Liu, S., Song, W., Qiao, J., & Ruan, H. (2021). Types of nuclear localization signals and mechanisms of protein import into the nucleus. *Cell Communication and Signaling*, *19*(1), 1–10. https://doi.org/https://doi.org/10.1186/s12964-021-00741-y

Luo, X., Budihardjo, I., Zou, H., Slaughter, C., & Wang, X. (1998). Bid, a Bcl2 interacting protein, mediates cytochrome c release from mitochondria in response to activation of cell surface death receptors. *Cell*, *94*(4), 481–490. https://doi.org/10.1016/S0092-8674(00)81589-5

Machesky, L. M., & Insall, R. H. (1998). Scar1 and the related Wiskott-Aldrich syndrome protein, WASP, regulate the actin cytoskeleton through the Arp2/3 complex. *Current Biology*, *8*(25), 1347–1356. https://doi.org/10.1016/S0960-9822(98)00015-3

Macosko, E. Z., Basu, A., Satija, R., Nemesh, J., Shekhar, K., Goldman, M., Tirosh, I., Bialas, A. R., Kamitaki, N., Martersteck, E. M., Trombetta, J. J., Weitz, D. A., Sanes, J. R., Shalek, A. K., Regev, A., & McCarroll, S. A. (2015). Highly parallel genome-wide expression profiling of individual cells using nanoliter droplets. *Cell*, *161*(5), 1202. https://doi.org/10.1016/J.CELL.2015.05.002

Maekawa, M., Ishizaki, T., Boku, S., Watanabe, N., Fujita, A., Iwamatsu, A., Obinata, T., Ohashi, K., Mizuno, K., & Narumiya, S. (1999). Signaling from Rho to the actin cytoskeleton through protein kinases ROCK and LIM-kinase. *Science*, *285*(5429), 895–898. https://doi.org/10.1126/SCIENCE.285.5429.895

Margolin, W. (2012). The Price of Tags in Protein Localization Studies. *Journal of Bacteriology*, *194*(23), 6369. https://doi.org/10.1128/JB.01640-12

Martin, S. S., & Leder, P. (2001). Human MCF10A mammary epithelial cells undergo apoptosis following actin depolymerization that is independent of attachment and rescued by Bcl-2. *Molecular and Cellular Biology*, *21*(19), 6529–6536. https://doi.org/10.1128/MCB.21.19.6529-6536.2001

Martinon, F., Burns, K., & Tschopp, J. (2002). The Inflammasome: A molecular platform triggering activation of inflammatory caspases and processing of proIL-β. *Molecular Cell*, *10*(2), 417–426. https://doi.org/10.1016/S1097-2765(02)00599-3

Mashima, T., Naito, M., Noguchi, K., Miller, D. K., Nicholson, D. W., & Tsuruo, T. (1997). Actin cleavage by CPP-32/apopain during the development of apoptosis. *Oncogene 1997 14:9*, *14*(9), 1007–1012. https://doi.org/10.1038/sj.onc.1200919

Mashima, T., Naito, M., & Tsuruo, T. (1999). Caspase-mediated cleavage of cytoskeletal actin plays a positive role in the process of morphological apoptosis. *Oncogene 1999 18:15*, *18*(15), 2423–2430. https://doi.org/10.1038/sj.onc.1202558

Meister, A. (1995). Glutathione metabolism. *Methods in Enzymology*, *251*(C), 3–7. https://doi.org/10.1016/0076-6879(95)51106-7

Mellacheruvu, D., Wright, Z., Couzens, A. L., Lambert, J. P., St-Denis, N. A., Li, T., Miteva, Y. V., Hauri, S., Sardiu, M. E., Low, T. Y., Halim, V. A., Bagshaw, R. D., Hubner, N. C., Al-Hakim, A., Bouchard, A., Faubert, D., Fermin, D., Dunham, W. H., Goudreault, M., … Nesvizhskii, A. I. (2013). The CRAPome: a contaminant repository for affinity purification–mass spectrometry data. *Nature Methods 2013 10:8*, *10*(8), 730–736. https://doi.org/10.1038/nmeth.2557

Mengwasser, K. E., Adeyemi, R. O., Leng, Y., Choi, M. Y., Clairmont, C., D'Andrea, A. D., & Elledge, S. J. (2019). Genetic Screens Reveal FEN1 and APEX2 as BRCA2 Synthetic Lethal Targets. *Molecular Cell*, *73*(5), 885-899.e6. https://doi.org/10.1016/j.molcel.2018.12.008

Metzger, M. B., Hristova, V. A., & Weissman, A. M. (2012). HECT and RING finger families of E3 ubiquitin ligases at a glance. *Journal of Cell Science*, *125*(3), 531–537. https://doi.org/10.1242/JCS.091777

Meyers, R. M., Bryan, J. G., McFarland, J. M., Weir, B. A., Sizemore, A. E., Xu, H., Dharia, N. V., Montgomery, P. G., Cowley, G. S., Pantel, S., Goodale, A., Lee, Y., Ali, L. D., Jiang, G., Lubonja, R., Harrington, W. F., Strickland, M., Wu, T., Hawes, D. C., … Tsherniak, A. (2017). Computational correction of copy number effect improves specificity of CRISPR–Cas9 essentiality screens in cancer cells. *Nature Genetics 2017 49:12*, *49*(12), 1779–1784. https://doi.org/10.1038/ng.3984

Micheau, O., & Tschopp, J. (2003). Induction of TNF receptor I-mediated apoptosis via two sequential signaling complexes. *Cell*, *114*(2), 181–190. https://doi.org/10.1016/S0092-8674(03)00521-X

Moseley, J. B., & Goode, B. L. (2006). The Yeast Actin Cytoskeleton: from Cellular Function to Biochemical Mechanism. *Microbiology and Molecular Biology Reviews*, *70*(3), 605. https://doi.org/10.1128/MMBR.00013-06

Muzio, M., Stockwell, B. R., Stennicke, H. R., Salvesen, G. S., & Dixit, V. M. (1998). An induced proximity model for caspase-8 activation. *The Journal of Biological Chemistry*, *273*(5), 2926–2930. https://doi.org/10.1074/JBC.273.5.2926

Nandi, D., Tahiliani, P., Kumar, A., & Chandu, D. (2006). The ubiquitin-proteasome system. *Journal of Biosciences*, *31*(1), 137–155. https://doi.org/10.1007/BF02705243

Nguyen Ba, A. N., Pogoutse, A., Provart, N., & Moses, A. M. (2009). NLStradamus: a simple Hidden Markov Model for nuclear localization signal prediction. *BMC Bioinformatics*, *10*. https://doi.org/10.1186/1471-2105-10-202

Nicholson, A. G., Tsao, M. S., Beasley, M. B., Borczuk, A. C., Brambilla, E., Cooper, W. A., Dacic, S., Jain, D., Kerr, K. M., Lantuejoul, S., Noguchi, M., Papotti, M., Rekhtman, N., Scagliotti, G., van Schil, P., Sholl, L., Yatabe, Y., Yoshida, A., & Travis, W. D. (2022). The

2021 WHO Classification of Lung Tumors: Impact of Advances Since 2015. *Journal of Thoracic Oncology*, *17*(3), 362–387. https://doi.org/https://doi.org/10.1016/j.jtho.2021.11.003

Nicholson, D. W. (1999). Caspase structure, proteolytic substrates, and function during apoptotic cell death. *Cell Death & Differentiation 1999 6:11*, *6*(11), 1028–1042. https://doi.org/10.1038/sj.cdd.4400598

Nobes, C. D., & Hall, A. (1995). Rho, rac, and cdc42 GTPases regulate the assembly of multimolecular focal complexes associated with actin stress fibers, lamellipodia, and filopodia. *Cell*, *81*(1), 53–62. https://doi.org/10.1016/0092-8674(95)90370-4

Nolen, B. J., & Pollard, T. D. (2008). Structure and Biochemical Properties of Fission Yeast Arp2/3 Complex Lacking the Arp2 Subunit. *The Journal of Biological Chemistry*, *283*(39), 26490. https://doi.org/10.1074/JBC.M802607200

Oan, J., Chiller, H. S., Avid, D., Arrington, H., Handra, C., Elani, P. B., Orey, C., Anger, L., Lan, A., Andler, S., Ames, J., Rook, K., Unming, J., Hu, Z., & Ohnson, P. H. D. J. (2002). Comparison of Four Chemotherapy Regimens for Advanced Non–Small-Cell Lung Cancer. *The New England Journal of Medicine*, *346*(2), 92–98. https://doi.org/10.1056/NEJMOA011954

O'Connor, H. F., Lyon, N., Leung, J. W., Agarwal, P., Swaim, C. D., Miller, K. M., & Huibregtse, J. M. (2015). Ubiquitin-Activated Interaction Traps (UBAITs) identify E3 ligase binding partners. *EMBO Reports*, *16*(12), 1699–1712. https://doi.org/10.15252/EMBR.201540620

Otomo, T., Otomo, C., Tomchick, D. R., Machius, M., & Rosen, M. K. (2005). Structural basis of Rho GTPase-mediated activation of the formin mDia1. *Molecular Cell*, *18*(3), 273–281. https://doi.org/10.1016/j.molcel.2005.04.002

Parekh, S., Ziegenhain, C., Vieth, B., Enard, W., & Hellmann, I. (2016). The impact of amplification on differential expression analyses by RNA-seq. *Scientific Reports*, *6*. https://doi.org/10.1038/SREP25533

Passaro, A., Jänne, P. A., Mok, T., & Peters, S. (2021). Overcoming therapy resistance in EGFR-mutant lung cancer. *Nature Cancer 2021 2:4*, *2*(4), 377–391. https://doi.org/10.1038/s43018-021-00195-8

Paulmann, C., Spallek, R., Karpiuk, O., Heider, M., Schäffer, I., Zecha, J., Klaeger, S., Walzik, M., Öllinger, R., Engleitner, T., Wirth, M., Keller, U., Krönke, J., Rudelius, M., Kossatz, S., Rad, R., Kuster, B., & Bassermann, F. (2022). The OTUD6B-LIN28B-MYC axis determines the proliferative state in multiple myeloma. *The EMBO Journal*, *41*(20), e110871. https://doi.org/10.15252/EMBJ.2022110871

Paulo, J. A., Kadiyala, V., Banks, P. A., Steen, H., & Conwell, D. L. (2012). Mass Spectrometry-Based Proteomics for Translational Research: A Technical Overview. *The Yale Journal of Biology and Medicine*, *85*(1), 59. /pmc/articles/PMC3313540/

Pellegrin, S., & Mellor, H. (2007). Actin stress fibres. *Journal of Cell Science*, *120*(20), 3491–3499. https://doi.org/10.1242/JCS.018473

Peters, S., Camidge, D. R., Shaw, A. T., Gadgeel, S., Ahn, J. S., Kim, D.-W., Ou, S.-H. I., Pérol, M., Dziadziuszko, R., Rosell, R., Zeaiter, A., Mitry, E., Golding, S., Balas, B., Noe, J., Morcos, P. N., & Mok, T. (2017). Alectinib versus Crizotinib in Untreated ALK -Positive Non–Small-Cell Lung Cancer . *New England Journal of Medicine*, *377*(9), 829–838. https://doi.org/10.1056/NEJMOA1704795/

Petroski, M. D., & Deshaies, R. J. (2005). Function and regulation of cullin-RING ubiquitin ligases. In *Nature Reviews Molecular Cell Biology* (Vol. 6, Issue 1, pp. 9–20). https://doi.org/10.1038/nrm1547

Pickart, C. M. (2001). Mechanisms underlying ubiquitination. *Annual Review of Biochemistry*, *70*, 503–533. https://doi.org/10.1146/ANNUREV.BIOCHEM.70.1.503

Pietkiewicz, S., Schmidt, J. H., & Lavrik, I. N. (2015). Quantification of apoptosis and necroptosis at the single cell level by a combination of Imaging Flow Cytometry with classical Annexin V/propidium iodide staining. *Journal of Immunological Methods*, *423*, 99–103. https://doi.org/10.1016/J.JIM.2015.04.025

Planchard, D., Kim, T. M., Mazieres, J., Quoix, E., Riely, G., Barlesi, F., Souquet, P. J., Smit, E. F., Groen, H. J. M., Kelly, R. J., Cho, B. C., Socinski, M. A., Pandite, L., Nase, C., Ma, B., D'Amelio, A., Mookerjee, B., Curtis, C. M., & Johnson, B. E. (2016). Dabrafenib in patients with BRAFV600E-positive advanced non-small-cell lung cancer: A single-arm, multicentre, open-label, phase 2 trial. *The Lancet Oncology*, *17*(5), 642–650. https://doi.org/10.1016/S1470-2045(16)00077-2

Planchard, D., Popat, S., Kerr, K., Novello, S., Smit, E. F., Faivre-Finn, C., Mok, T. S., Reck, M., Van Schil, P. E., Hellmann, M. D., & Peters, S. (2018). Metastatic non-small cell lung cancer: ESMO Clinical Practice Guidelines for diagnosis, treatment and follow-up†. *Annals of Oncology*, *29*, iv192–iv237. https://doi.org/10.1093/ANNONC/MDY275

Pollard, T. D., & Cooper, J. A. (2009). Actin, a Central Player in Cell Shape and Movement. *Science*, *326*(5957), 1208–1212. https://doi.org/10.1126/SCIENCE.1175862

Postmus, P. E., Kerr, K. M., Oudkerk, M., Senan, S., Waller, D. A., Vansteenkiste, J., Escriu, C., & Peters, & S. (2017). Early and locally advanced non-small-cell lung cancer (NSCLC): ESMO Clinical Practice Guidelines for diagnosis, treatment and follow-up. *ESMO Updated Clinical Practice Guidelines*, *28*, iv1–iv21. https://doi.org/10.1093/annonc/mdx222

Pruyne, D., Evangelista, M., Yang, C., Bi, E., Zigmond, S., Bretscher, A., & Boone, C. (2002). Role of formins in actin assembly: Nucleation and barbed-end association. *Science*, *297*(5581), 612–615. https://doi.org/https://doi.org/10.1126/science.1072309

Puthalakath, H., Villunger, A., O'Reilly, L. A., Beaumont, J. G., Coultas, L., Cheney, R. E., Huang, D. C. S., & Strasser, A. (2001). Bmf: a proapoptotic BH3-only protein regulated

by interaction with the myosin V actin motor complex, activated by anoikis. *Science*, *293*(5536), 1829–1832. https://doi.org/10.1126/SCIENCE.1062257

Ravid, T., & Hochstrasser, M. (2008). Diversity of degradation signals in the ubiquitin–proteasome system. *Nature Reviews Molecular Cell Biology 2008 9:9*, *9*(9), 679–689. https://doi.org/10.1038/nrm2468

Reck, M., Rodríguez-Abreu, D., Robinson, A. G., Hui, R., Csőszi, T., Fülöp, A., Gottfried, M., Peled, N., Tafreshi, A., Cuffe, S., O'Brien, M., Rao, S., Hotta, K., Leiby, M. A., Lubiniecki, G. M., Shentu, Y., Rangwala, R., & Brahmer, J. R. (2016). Pembrolizumab versus Chemotherapy for PD-L1–Positive Non–Small-Cell Lung Cancer. *New England Journal of Medicine*, *375*(19), 1823–1833. https://doi.org/10.1056/NEJMOA1606774

Remon, J., Soria, J. C., & Peters, S. (2021). Early and locally advanced non-small-cell lung cancer: an update of the ESMO Clinical Practice Guidelines focusing on diagnosis, staging, systemic and local therapy. *Annals of Oncology*, *32*(12), 1637–1642. https://doi.org/10.1016/j.annonc.2021.08.1994

Rho, S. B., Chun, T., Lee, S. H., Park, K., & Lee, J. H. (2004). The interaction between E-tropomodulin and thymosin β-10 rescues tumor cells from thymosin β-10 mediated apoptosis by restoring actin architecture. *FEBS Letters*, *557*(1–3), 57–63. https://doi.org/10.1016/S0014-5793(03)01438-8

Rohatgi, R., Ma, L., Miki, H., Lopez, M., Kirchhausen, T., Takenawa, T., & Kirschner, M. W. (1999). The interaction between N-WASP and the Arp2/3 complex links Cdc42-dependent signals to actin assembly. *Cell*, *97*(2), 221–231. https://doi.org/10.1016/S0092-8674(00)80732-1

Rosell, R., Carcereny, E., Gervais, R., Vergnenegre, A., Massuti, B., Felip, E., Palmero, R., Garcia-Gomez, R., Pallares, C., Sanchez, J. M., Porta, R., Cobo, M., Garrido, P., Longo, F., Moran, T., Insa, A., De Marinis, F., Corre, R., Bover, I., … Paz-Ares, L. (2012). Erlotinib versus standard chemotherapy as first-line treatment for European patients with advanced EGFR mutation-positive non-small-cell lung cancer (EURTAC): A multicentre, open-label, randomised phase 3 trial. *The Lancet Oncology*, *13*(3), 239–246. https://doi.org/10.1016/S1470-2045(11)70393-X

Rotin, D., & Kumar, S. (2009). Physiological functions of the HECT family of ubiquitin ligases. *Nature Reviews. Molecular Cell Biology*, *10*(6), 398–409. https://doi.org/10.1038/NRM2690

Rottner, K., Faix, J., Bogdan, S., Linder, S., & Kerkhoff, E. (2017). Actin assembly mechanisms at a glance. *Journal of Cell Science*, *130*(20), 3427–3435. https://doi.org/10.1242/JCS.206433

Roufayel, R., Younes, K., Al-Sabi, A., & Murshid, N. (2022). BH3-Only Proteins Noxa and Puma Are Key Regulators of Induced Apoptosis. *Life*, *12*(2). https://doi.org/10.3390/LIFE12020256

Roux, K. J., Kim, D. I., Raida, M., & Burke, B. (2012). A promiscuous biotin ligase fusion protein identifies proximal and interacting proteins in mammalian cells. *Journal of Cell Biology*, *196*(6), 801–810. https://doi.org/10.1083/JCB.201112098

Sainz De Aja, J., Dost, A. F. M., Kim, C. F., Sainz De Aja, A., Afm, D., Cf, K., & Boston, (. (2021). Alveolar progenitor cells and the origin of lung cancer. *Journal of Internal Medicine*, *289*(5), 629–635. https://doi.org/10.1111/JOIM.13201

Sarikas, A., Hartmann, T., & Pan, Z. Q. (2011). The cullin protein family. *Genome Biology*, *12*(4), 1–12. https://doi.org/https://doi.org/10.1186/gb-2011-12-4-220

Sato, H., Tamba, M., Ishii, T., & Bannai, S. (1999). Cloning and expression of a plasma membrane cystine/glutamate exchange transporter composed of two distinct proteins. *Journal of Biological Chemistry*, *274*(17), 11455–11458. https://doi.org/10.1074/jbc.274.17.11455

Savill, J., & Fadok, V. (2000). Corpse clearance defines the meaning of cell death. *Nature 2000 407:6805*, *407*(6805), 784–788. https://doi.org/10.1038/35037722

Schneider, P., Bodmer, J. L., Holler, N., Mattmann, C., Scuderi, P., Terskikh, A., Peitsch, M. C., & Tschopp, J. (1997). Characterization of Fas (Apo-1, CD95)-Fas ligand interaction. *The Journal of Biological Chemistry*, *272*(30), 18827–18833. https://doi.org/10.1074/JBC.272.30.18827

Schneider, P., Thome, M., Burns, K., Bodmer, J. L., Hofmann, K., Kataoka, T., Holler, N., & Tschopp, J. (1997). TRAIL receptors 1 (DR4) and 2 (DR5) signal FADD-dependent apoptosis and activate NF-kappaB. *Immunity*, *7*(6), 831–836. https://doi.org/10.1016/S1074-7613(00)80401-X

Schulman, B. A., & Wade Harper, J. (2009). Ubiquitin-like protein activation by E1 enzymes: the apex for downstream signalling pathways. *Nature Reviews. Molecular Cell Biology*, *10*(5), 319. https://doi.org/10.1038/NRM2673

Seol, D. W., Li, J., Seol, M. H., Park, S. Y., Talanian, R. V., & Billiar, T. R. (2001). Signaling events triggered by tumor necrosis factor-related apoptosis-inducing ligand (TRAIL): caspase-8 is required for TRAIL-induced apoptosis. *Cancer Research*, *61*(3), 1138–1143. https://pubmed.ncbi.nlm.nih.gov/11221844/

Shalem, O., Sanjana, N. E., Hartenian, E., Shi, X., Scott, D. A., Mikkelsen, T. S., Heckl, D., Ebert, B. L., Root, D. E., Doench, J. G., & Zhang, F. (2014). Genome-scale CRISPR-Cas9 knockout screening in human cells. *Science*, *343*(6166), 84–87. https://doi.org/https://doi.org/10.1126/science.1247005

Shan, B. Q., Wang, X. M., Zheng, L., Han, Y., Gao, J., Lv, M. D., Zhang, Y., Liu, Y. X., Zhang, H., Chen, H. S., Ao, L., Zhang, Y. L., Lu, X., Wu, Z. J., Xu, Y., Che, X., Heger, M., Cheng, S. Q., Pan, W. W., & Zhang, X. (2022). DCAF13 promotes breast cancer cell proliferation by ubiquitin inhibiting PERP expression. *Cancer Science*, *113*(5), 1587–1600. https://doi.org/10.1111/CAS.15300

Sherman, B. T., Hao, M., Qiu, J., Jiao, X., Baseler, M. W., Lane, H. C., Imamichi, T., & Chang, W. (2022). DAVID: a web server for functional enrichment analysis and functional annotation of gene lists (2021 update). *Nucleic Acids Research*, *50*(W1), W216–W221. https://doi.org/10.1093/NAR/GKAC194

Shi, D., & Grossman, S. R. (2010). Ubiquitin becomes ubiquitous in cancer. *Cancer Biology & Therapy*, *10*(8), 737–747. https://doi.org/10.4161/CBT.10.8.13417

Shi, J., Zhao, Y., Wang, K., Shi, X., Wang, Y., Huang, H., Zhuang, Y., Cai, T., Wang, F., & Shao, F. (2015). Cleavage of GSDMD by inflammatory caspases determines pyroptotic cell death. *Nature 2015 526:7575*, *526*(7575), 660–665. https://doi.org/10.1038/nature15514

Sidhu, H., & Capalash, N. (2017). UHRF1: The key regulator of epigenetics and molecular target for cancer therapeutics. *Tumour Biology*, *39*(2), 1–11. https://doi.org/10.1177/1010428317692205

Singh, R., Letai, A., & Sarosiek, K. (2019). Regulation of apoptosis in health and disease: the balancing act of BCL-2 family proteins. *Nature Reviews Molecular Cell Biology 2018 20:3*, *20*(3), 175–193. https://doi.org/10.1038/s41580-018-0089-8

Skelly, M. J., & Spoel, S. H. (2021). Characterising plant deubiquitinases within vitro activity-based labelling and ubiquitin chain disassembly assays. *Bio-Protocol*, *11*(9). https://doi.org/10.21769/BIOPROTOC.4015

Skoulidis, F., & Heymach, J. V. (2019). Co-occurring genomic alterations in non-small-cell lung cancer biology and therapy. *Nature Reviews Cancer 2019 19:9*, *19*(9), 495–509. https://doi.org/10.1038/s41568-019-0179-8

Slivka, P. F., Hsieh, C. L., Lipovsky, A., Pratt, S. D., Locklear, J., Namovic, M. T., McDonald, H. A., Wetter, J., Edelmayer, R., Hu, M., Murphy, E., Domanus, M., Lu, C., Duggan, R., King, J., Scott, V. E., Donnelly-Roberts, D., Slavin, A., Gopalakrishnan, S., … Goedken, E. R. (2019). Small Molecule and Pooled CRISPR Screens Investigating IL17 Signaling Identify BRD2 as a Novel Contributor to Keratinocyte Inflammatory Responses. *ACS Chemical Biology*, *14*(5), 857–872. https://doi.org/10.1021/ACSCHEMBIO.8B00260

Smit, J. J., & Sixma, T. K. (2014). RBR E3-ligases at work. *EMBO Reports*, *15*(2), 142–154. https://doi.org/10.1002/EMBR.201338166

Soria, J.-C., Ohe, Y., Vansteenkiste, J., Reungwetwattana, T., Chewaskulyong, B., Lee, K. H., Dechaphunkul, A., Imamura, F., Nogami, N., Kurata, T., Okamoto, I., Zhou, C., Cho, B. C., Cheng, Y., Cho, E. K., Voon, P. J., Planchard, D., Su, W.-C., Gray, J. E., … Ramalingam, S. S. (2018). Osimertinib in Untreated EGFR -Mutated Advanced Non–Small-Cell Lung Cancer . *New England Journal of Medicine*, *378*(2), 113–125. https://doi.org/10.1056/NEJMoa1713137

Spigel, D. R., Faivre-Finn, C., Gray, J. E., Vicente, D., Planchard, D., Paz-Ares, L., Vansteenkiste, J. F., Garassino, M. C., Hui, R., Quantin, X., Rimner, A., Wu, Y. L.,

Özgüroğlu, M., Lee, K. H., Kato, T., De Wit, M., Kurata, T., Reck, M., Cho, B. C., … Antonia, S. J. (2022). Five-Year Survival Outcomes From the PACIFIC Trial: Durvalumab After Chemoradiotherapy in Stage III Non-Small-Cell Lung Cancer. *Journal of Clinical Oncology*, *40*(12), 1301–1311. https://doi.org/10.1200/JCO.21.01308

Streich, F. C., & Lima, C. D. (2016). Capturing a substrate in an activated RING E3/E2-SUMO complex. *Nature*, *536*(7616), 304. https://doi.org/10.1038/NATURE19071

Su, L., Quade, B., Wang, H., Sun, L., Wang, X., & Rizo, J. (2014). A plug release mechanism for membrane permeation by MLKL. *Structure* , *22*(10), 1489–1500. https://doi.org/10.1016/J.STR.2014.07.014

Sun, Y., Baechler, S. A., Zhang, X., Kumar, S., Factor, V. M., Arakawa, Y., Chau, C. H., Okamoto, K., Parikh, A., Walker, B., Su, Y. P., Chen, J., Ting, T., Huang, S. yin N., Beck, E., Itkin, Z., McKnight, C., Xie, C., Roper, N., … Pommier, Y. (2023). Targeting neddylation sensitizes colorectal cancer to topoisomerase I inhibitors by inactivating the DCAF13-CRL4 ubiquitin ligase complex. *Nature Communications*, *14*(1). https://doi.org/10.1038/S41467-023-39374-9

Sun, Z., Zhou, D., Yang, J., & Zhang, D. (2022). Doxorubicin promotes breast cancer cell migration and invasion via DCAF13. *FEBS Open Bio*, *12*(1), 221–230. https://doi.org/10.1002/2211-5463.13330

Suraneni, P., Rubinstein, B., Unruh, J. R., Durnin, M., Hanein, D., & Li, R. (2012). The Arp2/3 complex is required for lamellipodia extension and directional fibroblast cell migration. *Journal of Cell Biology*, *197*(2), 239–251. https://doi.org/https://doi.org/10.1083/jcb.201112113

Swatek, K. N., & Komander, D. (2016). Ubiquitin modifications. *Cell Research*, *26*(4), 399. https://doi.org/10.1038/CR.2016.39

Tait, S. W. G., & Green, D. R. (2010). Mitochondria and cell death: outer membrane permeabilization and beyond. *Nature Reviews Molecular Cell Biology 2010 11:9*, *11*(9), 621–632. https://doi.org/10.1038/nrm2952

Tapon, N., & Hall, A. (1997). Rho, Rac and Cdc42 GTPases regulate the organization of the actin cytoskeleton. *Current Opinion in Cell Biology*, *9*(1), 86–92. https://doi.org/10.1016/S0955-0674(97)80156-1

Taylor, R. C., Cullen, S. P., & Martin, S. J. (2008). Apoptosis: controlled demolition at the cellular level. *Nature Reviews Molecular Cell Biology 2008 9:3*, *9*(3), 231–241. https://doi.org/10.1038/nrm2312

Tenev, T., Bianchi, K., Darding, M., Broemer, M., Langlais, C., Wallberg, F., Zachariou, A., Lopez, J., MacFarlane, M., Cain, K., & Meier, P. (2011). The Ripoptosome, a Signaling Platform that Assembles in Response to Genotoxic Stress and Loss of IAPs. *Molecular Cell*, *43*(3), 432–448. https://doi.org/10.1016/J.MOLCEL.2011.06.006

Thai, A. A., Solomon, B. J., Sequist, L. V., Gainor, J. F., & Heist, R. S. (2021). Lung cancer. *The Lancet*, *398*(10299), 535–554. https://doi.org/10.1016/S0140-6736(21)00312-3

Tomko, R. J., & Hochstrasser, M. (2013). Molecular Architecture and Assembly of the Eukaryotic Proteasome. *Annual Review of Biochemistry* , *82*, 415–445. https://doi.org/10.1146/ANNUREV-BIOCHEM-060410-150257

Törnkvist, A., Sjöberg, P. J. R., Markides, K. E., & Bergquist, J. (2004). Analysis of catecholamines and related substances using porous graphitic carbon as separation media in liquid chromatography-tandem mass spectrometry. *Journal of Chromatography B*, *801*(2), 323–329. https://doi.org/10.1016/j.jchromb.2003.11.036

Ursini, F., Maiorino, M., Valente, M., Ferri, L., & Gregolin, C. (1982). Purification from pig liver of a protein which protects liposomes and biomembranes from peroxidative degradation and exhibits glutathione peroxidase activity on phosphatidylcholine hydroperoxides. *Biochimica et Biophysica Acta (BBA) - Lipids and Lipid Metabolism*, *710*(2), 197–211. https://doi.org/10.1016/0005-2760(82)90150-3

Vansteenkiste, J., Crinò, L., Dooms, C., Douillard, J. Y., Faivre-Finn, C., Lim, E., Rocco, G., Senan, S., van Schil, P., Veronesi, G., Stahel, R., Peters, S., Felip, E., Kerr, K., Besse, B., Eberhardt, W., Edelman, M., Mok, T., O'Byrne, K., … Westeel, V. (2014). 2nd ESMO consensus conference on lung cancer: Early-stage non-small-cell lung cancer consensus on diagnosis, treatment and follow-up. *Annals of Oncology*, *25*(8), 1462–1474. https://doi.org/10.1093/annonc/mdu089

Varadi, M., Anyango, S., Deshpande, M., Nair, S., Natassia, C., Yordanova, G., Yuan, D., Stroe, O., Wood, G., Laydon, A., Zídek, A., Green, T., Tunyasuvunakool, K., Petersen, S., Jumper, J., Clancy, E., Green, R., Vora, A., Lutfi, M., … Velankar, S. (2022). AlphaFold Protein Structure Database: massively expanding the structural coverage of protein-sequence space with high-accuracy models. *Nucleic Acids Research*, *50*(D1), D439–D444. https://doi.org/10.1093/NAR/GKAB1061

Varshavsky, A. (1991). Naming a targeting signal. *Cell*, *64*(1), 13–15. https://doi.org/10.1016/0092-8674(91)90202-A

Vichas, A., Riley, A. K., Nkinsi, N. T., Kamlapurkar, S., Parrish, P. C. R., Lo, A., Duke, F., Chen, J., Fung, I., Watson, J., Rees, M., Gabel, A. M., Thomas, J. D., Bradley, R. K., Lee, J. K., Hatch, E. M., Baine, M. K., Rekhtman, N., Ladanyi, M., … Berger, A. H. (2021). Integrative oncogene-dependency mapping identifies RIT1 vulnerabilities and synergies in lung cancer. *Nature Communications*, *12*(1). https://doi.org/10.1038/S41467-021-24841-Y

Wang, J., Thomas, H. R., Li, Z., Yeo, N. C., Scott, H. E., Dang, N., Hossain, M. I., Andrabi, S. A., & Parant, J. M. (2021). Puma, noxa, p53, and p63 differentially mediate stress pathway induced apoptosis. *Cell Death & Disease 2021 12:7*, *12*(7), 1–11. https://doi.org/10.1038/s41419-021-03902-6

Wang, K., Li, L., Fu, L., Yuan, Y., Dai, H., Zhu, T., Zhou, Y., & Yuan, F. (2019). Integrated Bioinformatics Analysis the Function of RNA Binding Proteins (RBPs) and Their Prognostic Value in Breast Cancer. *Frontiers in Pharmacology*, *10*. https://doi.org/10.3389/FPHAR.2019.00140

Wang, Y., Gao, W., Shi, X., Ding, J., Liu, W., He, H., Wang, K., & Shao, F. (2017). Chemotherapy drugs induce pyroptosis through caspase-3 cleavage of a gasdermin. *Nature 2017 547:7661*, *547*(7661), 99–103. https://doi.org/10.1038/nature22393

Wang, Y. Q., Wang, L., Zhang, M. Y., Wang, T., Bao, H. J., Liu, W. L., Dai, D. K., Zhang, L., Chang, P., Dong, W. W., Chen, X. P., & Tao, L. Y. (2012). Necrostatin-1 suppresses autophagy and apoptosis in mice traumatic brain injury model. *Neurochemical Research*, *37*(9), 1849–1858. https://doi.org/https://doi.org/10.1007/s11064-012-0791-4

Watanabe, M., Saeki, Y., Takahashi, H., Ohtake, F., Yoshida, Y., Kasuga, Y., Kondo, T., Yaguchi, H., Suzuki, M., Ishida, H., Tanaka, K., & Hatakeyama, S. (2020). A substrate-trapping strategy to find E3 ubiquitin ligase substrates identifies Parkin and TRIM28 targets. *Communications Biology 2020 3:1*, *3*(1), 1–13. https://doi.org/10.1038/s42003-020-01328-y

Wéber, A., Morgan, E., Vignat, J., Laversanne, M., Pizzato, M., Rumgay, H., Singh, D., Nagy, P., Kenessey, I., Soerjomataram, I., & Bray, F. (2023). Lung cancer mortality in the wake of the changing smoking epidemic: a descriptive study of the global burden in 2020 and 2040. *BMJ Open*, *13*(5), e065303. https://doi.org/10.1136/BMJOPEN-2022-065303

Wei, S., Lu, K., Xing, J., & Yu, W. (2023). A multidimensional pan-cancer analysis of DCAF13 and its protumorigenic effect in lung adenocarcinoma. *FASEB Journal*, *37*(4). https://doi.org/10.1096/FJ.202201022RRR

Williams, J. R., Little, J. B., & Shipley, W. U. (1974). Association of mammalian cell death with a specific endonucleolytic degradation of DNA. *Nature 1974 252:5485*, *252*(5485), 754–755. https://doi.org/10.1038/252754a0

Winter, J., Schwering, M., Pelz, O., Rauscher, B., Zhan, T., Heigwer, F., & Boutros, M. (2017). CRISPRAnalyzeR: Interactive analysis, annotation and documentation of pooled CRISPR screens. *BioRxiv*, 109967. https://doi.org/10.1101/109967

Winter, S. C., Buffa, F. M., Silva, P., Miller, C., Valentine, H. R., Turley, H., Shah, K. A., Cox, G. J., Corbridge, R. J., Homer, J. J., Musgrove, B., Slevin, N., Sloan, P., Price, P., West, C. M. L., & Harris, A. L. (2007). Relation of a hypoxia metagene derived from head and neck cancer to prognosis of multiple cancers. *Cancer Research*, *67*(7), 3441–3449. https://doi.org/10.1158/0008-5472.CAN-06-3322

Wu, D., & Smyth, G. K. (2012). Camera: a competitive gene set test accounting for inter-gene correlation. *Nucleic Acids Research*, *40*(17), e133–e133. https://doi.org/10.1093/NAR/GKS461

Wu, J., & Akhmanova, A. (2017). Microtubule-Organizing Centers. *Annual Review of Cell and Developmental Biology* , *33*, 51–75. https://doi.org/10.1146/ANNUREV-CELLBIO-100616-060615

Wu, W. K. K., Cho, C. H., Lee, C. W., Wu, K., Fan, D., Yu, J., & Yiu Sung, J. J. (2010). Proteasome inhibition: a new therapeutic strategy to cancer treatment. *Cancer Letters*, *293*(1), 15–22. https://doi.org/10.1016/J.CANLET.2009.12.002

Xu, P., Duong, D. M., Seyfried, N. T., Cheng, D., Xie, Y., Robert, J., Rush, J., Hochstrasser, M., Finley, D., & Peng, J. (2009). Quantitative proteomics reveals the function of unconventional ubiquitin chains in proteasomal degradation. *Cell*, *137*(1), 133–145. https://doi.org/10.1016/J.CELL.2009.01.041

Xu, P., Scott, D. C., Xu, B., Yao, Y., Feng, R., Cheng, L., Mayberry, K., Wang, Y. D., Bi, W., Palmer, L. E., King, M. T., Wang, H., Li, Y., Fan, Y., Alpi, A. F., Li, C., Peng, J., Papizan, J., Pruett-Miller, S. M., … Weiss, M. J. (2021). FBXO11-mediated proteolysis of BAHD1 relieves PRC2-dependent transcriptional repression in erythropoiesis. *Blood*, *137*(2), 155–167. https://doi.org/10.1182/BLOOD.2020007809

Xue, B., & Robinson, R. C. (2013). Guardians of the actin monomer. *European Journal of Cell Biology*, *92*(10–11), 316–332. https://doi.org/10.1016/J.EJCB.2013.10.012

Yang, W. S., Sriramaratnam, R., Welsch, M. E., Shimada, K., Skouta, R., Viswanathan, V. S., Cheah, J. H., Clemons, P. A., Shamji, A. F., Clish, C. B., Brown, L. M., Girotti, A. W., Cornish, V. W., Schreiber, S. L., & Stockwell, B. R. (2014). Regulation of ferroptotic cancer cell death by GPX4. *Cell*, *156*(1–2), 317–331. https://doi.org/10.1016/j.cell.2013.12.010

Ye, Y., & Rape, M. (2009). Building ubiquitin chains: E2 enzymes at work. *Nature Reviews. Molecular Cell Biology*, *10*(11), 755–764. https://doi.org/10.1038/NRM2780

Zhang, C., Li, C., Wang, Y., Xu, L., He, X., Zeng, Q., Zeng, C., Mai, F., Hu, B., & Ouyang, D. (2019). Chemotherapeutic paclitaxel and cisplatin differentially induce pyroptosis in A549 lung cancer cells via caspase-3/GSDME activation. *Apoptosis*, *24*(3–4), 312–325. https://doi.org/https://doi.org/10.1007/s10495-019-01515-1

Zhang, G., Wang, J., Zhao, Z., Xin, T., Fan, X., Shen, Q., Raheem, A., Lee, C. R., Jiang, H., & Ding, J. (2022). Regulated necrosis, a proinflammatory cell death, potentially counteracts pathogenic infections. *Cell Death & Disease 2022 13:7*, *13*(7), 1–14. https://doi.org/10.1038/s41419-022-05066-3

Zhang, J., Zhang, Y. L., Zhao, L. W., Guo, J. X., Yu, J. L., Ji, S. Y., Cao, L. R., Zhang, S. Y., Shen, L., Ou, X. H., & Fan, H. Y. (2019). Mammalian nucleolar protein DCAF13 is essential for ovarian follicle maintenance and oocyte growth by mediating rRNA processing. *Cell Death and Differentiation*, *26*(7), 1251–1266. https://doi.org/10.1038/s41418-018-0203-7

Zhang, Y., Zhao, L., Zhang, J., Le, R., Ji, S., Chen, C., Gao, Y., Li, D., Gao, S., & Fan, H. (2018). DCAF 13 promotes pluripotency by negatively regulating SUV 39H1 stability during early embryonic development. *The EMBO Journal*, *37*(18). https://doi.org/10.15252/embj.201898981

Zhao, J., Jitkaew, S., Cai, Z., Choksi, S., Li, Q., Luo, J., & Liu, Z. G. (2012). Mixed lineage kinase domain-like is a key receptor interacting protein 3 downstream component of TNF-induced necrosis. *Proceedings of the National Academy of Sciences of the United States of America*, *109*(14), 5322–5327. https://doi.org/https://doi.org/10.1073/pnas.1200012109

Zheng, L., Bidere, N., Staudt, D., Cubre, A., Orenstein, J., Chan, F. K., & Lenardo, M. (2006). Competitive control of independent programs of tumor necrosis factor receptor-induced cell death by TRADD and RIP1. *Molecular and Cellular Biology*, *26*(9), 3505–3513. https://doi.org/10.1128/MCB.26.9.3505-3513.2006

Zheng, N., & Shabek, N. (2017). Ubiquitin Ligases: Structure, Function, and Regulation. *Annual Review of Biochemistry*, *86*, 129–157. https://doi.org/10.1146/ANNUREV-BIOCHEM-060815-014922